Engineering Solid Binding Proteins for the Biofabrication of Environmentally Friendly Multi-functional Quantum Dots

Brian James Fullerton Swift

A dissertation submitted in partial fulfillment of the

requirements for the degree of

Doctor of Philosophy

University of Washington

2016

Reading Committee:

François Baneyx, Chairman

Dan T. Schwartz

Cole DeForest

Program Authorized to Offer Degree:

Department of Chemical Engineering

University of Washington

Abstract

Engineering Solid Binding Proteins for the Biofabrication of Environmentally Friendly Multi-functional Quantum Dots

Brian James Fullerton Swift

Chair of the Supervisory Committee
Dr. François Baneyx
Chemical Engineering

Methods that emulate Nature's remarkable ability to synthesize chemically and structurally intricate architectures are of considerable interest for the fabrication of industrially-relevant materials and systems. In this work, we design and engineer solid-binding proteins that drive the formation and assembly of multi-functional nanomaterials. We first describe a method to biomineralize Mn-doped ZnS immuno-quantum dots with a minimized protein and study how such protein-coated nanocrystals are taken up by, and impact the physiology of the model bacterium *Escherichia coli*. We next design and build ZnS-binding derivatives of Green Fluorescent Protein to mineralize nanocrystals that combine inorganic and organic fluorescence properties and combine these with DNA aptamers and silica phases to create small-molecule sensors. Finally, we demonstrate that solid-binding proteins can be used to solubilize carbon nanotubes and to selectively label their ends. Collectively, our results emphasize the power of protein engineering for the environmentally friendly synthesis of functional nanomaterials.

Table of Contents

Table of Figures

Acknowledgements

I would like to acknowledge the immense contributions that others have made in the development of this dissertation. None of this would have happened without the incomparable support of my wife, Katie, and her unfailing ability to inspire me to press onward. My lab-mates both former (Brent, Brandon, James, and Weibin) and current (Jessica, Alex, Brittney, and Sonja) have also been instrumental in my success here through their hijinks, intellectual input, and commiseration.

My colleagues in the Department also deserve special mention, because their work at building a community that cares for each other has done wonders for my mental health during this experience, but there are simply too many of them to name. I would also like to thank my advisor, François Baneyx, for his enduring patience and instruction in my evolution as a researcher. Additionally, thank you to my committee: Dan Schwartz, Cole DeForest, and Terry Kavanagh for your support and guidance on my projects over the years.

Finally, thank you to my family. To my parents, Mike and Linda, you raised me to think and question, to laugh and sing, and I will never be given better gifts than those nor could I thank you enough. To my siblings, Brad and Kim, you have kept me humble, taught me to fight, forced me to face fears, and kept me upright; you mean the world to me.

Introduction

Nature builds compositionally complex and hierarchically ordered materials that exhibit remarkable mechanical and functional properties.[1] This marvel of engineering is chiefly the work of proteins and peptides that are responsible for synthesizing most of the inorganic structures living beings need to survive.[2] Nature has spent billions of years evolving biomineralizing proteins and peptides for very specific functions,[3] and extensive research at the interface of biology and materials science has focused on understanding how they work.[4-6] Engineers and nanotechnologists have also used and modified these proteins, or simply drawn inspiration from their mode of action, to produce technologically relevant materials and systems.[7-9] This dissertation focuses on combining the solid binding peptide's (SBPs) capacity to bind inorganic materials[10] with our ability to modify proteins through genetic engineering to create useful, functional nanomaterials with nontoxic compositions via environmentally friendly schemes. More specifically, *Chapter 2* describes the use of a minimized protein fitted with a zinc sulfide (ZnS) binding sequence for the efficient synthesis of luminescent Mn-doped ZnS quantum dots (QDs) whose protein shell is capable of binding antibodies. *Chapter 3* explores the potential environmental toxicity of such biofabricated QDs using the model bacterium *Escherichia coli.* *Chapter 4* describes how luminescent nanocrystals can be mineralized with ZnS and silica-binding derivatives of the Green Fluorescent Protein (GFP) and how a combination of the two fluorophores and DNA aptamers can be used for small-molecule detection. *Chapter 5* demonstrates that silica binding GFP derivatives can be used for selective end-labeling of carbon nanotubes. Finally, a summary of results and a discussion of the impact of this research and its future directions are presented in concluding *Chapter 6*.

1.1 Biomineralization

Biomineralization refers to the solution synthesis of inorganic materials by biological species.[11, 12] It is key to the formation of vertebrate bones and teeth, mollusk shells, diatom frustules, and the magnetic crystals found in magnetotactic bacteria. The resulting materials are unique not because of their compositions – chiefly hydroxyapatite calcium phosphates, calcium carbonate ($CaCO_3$), silica (SiO_2), magnetite (Fe_3O_4) and greigite (Fe_3S_4) – but because of how they are synthesized and organized. Indeed, biological macromolecules, usually proteins and peptides, control the nucleation and growth phenomena that give rise to the nanoscale structure and hierarchical assembly that impart desirable properties to bioinorganics. For example, mollusk shells[13, 14] are composed of multiple polymorphs of $CaCO_3$, with nacre (**Figure 1.1**) being the most extensively studied because its mechanical strength greatly exceeds that of disordered $CaCO_3$.[15, 16] This is due to the fact that nacre is made from a precise brick and mortar layering[17-19] of aragonite platelets with joints consisting of a mixture of proteins and polysaccharides.[20]

While the precise spatio-temporal control of protein-ion-mineral interactions that lead to the complex architecture of nacre remains poorly understood and outside of our reach, it has been possible to recapitulate basic mineralization mechanisms by making use of proteins from biomineralizing organisms. For instance, a family of silica-mineralizing proteins called silaffins has been isolated from diatoms,[21] and used to synthesize silica nanoparticles *in vitro* (**Figure 1.2**).[21, 22] Silaffins are highly enriched in serine, lysine, and glycine residues and undergo considerable post-translational modifications (primarily polyamine addition to lysines) that are critical for silica precipitation.[21] In addition, phosphorylation of serine residues provides negative charges that are necessary for silaffins to form supramolecular structures required for the templating and condensation of silicic acid.[23] While silaffins drive silica formation in acidic

environments, the silicatein family of proteins from sponge spicules employs a histidine-serine-asparagine catalytic site to hydrolyze silicon alkoxides in neutral environments.[24-27] Silicateins also assemble intro macroscopic filaments that serve as scaffolds for templating the condensation of newly formed polysiloxanes to silica.[28] As biologists continue to explore the structure-function relationship of naturally-occurring biomineralizing proteins,[1, 28-39] engineers have set out to develop novel pathways to biofabricate industrially-relevant materials.

1.1.1 Solid binding peptides

Solid binding peptides (SBPs) are short sequences of amino acids capable of recognizing the surface of inorganic or synthetic materials with high affinity and/or specificity. Similar sequences occur in nature and support the mineralization and organization of inorganic materials such as silica[40] and hydroxyapatite[41, 42]. However, rather than being derived from natural biomineralizing proteins, SBPs are selected from combinatorial libraries for inorganic binding[43]. Although the list is not exhaustive, SBPs have been identified on gold[44, 45], silver[46], titania[47], silica[48, 49], zinc oxide[50], zinc sulfide[51], carbon[52], calcium phosphate[53], palladium[44], and cadmium[54] surfaces. The most common isolation methods are phage display[55, 56] using the Ph.D. system from New England Biolabs (Ipswich, MA) in which random heptapeptides or dodecapeptides are displayed on the M13 bacteriophage via fusion to the N-terminus of the p3 minor coat protein; and cell-surface display[57] using the FliTrx system from Invitrogen (Carlsbad, CA) in which disulfide-constrained dodecapeptides inserted within the TrxA oxidoreductase are displayed on *E. coli* flagella as insertional fusions to the FliC protein. These libraries typically count 10^8 to 10^9 unique members, a small fraction of the 10^{15} possible dodecapeptides that can be specified by the 20 natural amino acids. However, this low diversity is usually sufficient to identify SBPs. The

selection of peptides from Ph.D. or FliTrx libraries entails exposing phages or cells to the inorganic surface of interest, washing off weak binders, recovering the strong ones, and repeating the biopanning process 3 to 5 times to enrich for a manageable number (10 to 20) of solid-binding sequences. These methods have proven very effective at yielding SBPs that have a range of affinities for their cognate inorganics.

1.1.1.1 Biomineralization of zinc sulfide

The biomineralization of zinc sulfide (ZnS) is of particular interest to this work. ZnS nanoparticles are naturally made by sulfate-reducing bacteria,[58] and the so-called "zinc finger" proteins[59-62] coordinate zinc ions through the use of cysteine and histidine side chains. It is therefore not surprising that much of the original research on ZnS biomineralization has focused on the ability of the sulfhydryl-containing amino acid cysteine to arrest the growth of ZnS particles by capping.[62-64] This method, and related approaches that make use of histidine or glutathione, require high molar concentrations (>100 mM) for the capping process to be effective.[65, 66] It has separately been shown that the M1 peptide of the Influenza Virus Matrix Protein M1, which contains a Cys_2His_2 zinc finger domain, supports the mineralization of wurtzite ZnS when conjugated to peptide nanotubes.[64, 67] This process was sensitive to pH, because the M1 peptide experiences a conformational shift above pH 9 that prevents histidine residues from cooperatively binding zinc ions. The resulting change in the structure of the ZnS nucleation site alters the crystallinity of the particles from wurtzite to amorphous.[67]

In addition to free amino acids and the M1 peptide, SBPs have also been used to mediate ZnS biomineralization. For instance, Flynn and coworkers used phage display to isolate heptameric and dodecameric ZnS-binding peptides.[68] A Pro-Met-His-Gln motif was identified

within the heptamers but not the dodecamers,[68] although the latter often contained a basic amino acid paired with a proline and followed by a methionine or a hydroxyl containing residue. Both heptamers and dodecamers supported the mineralization of ZnS particles presumably by coordinating Zn^{2+} ions through the electron donors of histidine's imidazole ring. However, this interaction is not the only way to biomineralize ZnS.[69, 70] A separate study that used cell-surface display to identify ZnS binders found that charged residues separated by hydrophobic residues were important for ZnS binding, and made use of two peptides without any histidine or cysteines to mineralize wurtzite ZnS nanocrystals.[51] Thus, while Cys_2His_2 may be a powerful zinc ion-coordinating complex in nature, SBPs that lack both residues remain capable of mineralizing ZnS nanoparticles.

1.1.2 Solution conditions for biomineralization

The identification of SBPs is considerably more rapid than furthering our understanding of why and how they bind to a particular material. It is also much faster to isolate inorganic binders than to find the solution conditions under which they will mineralize a particular phase or drive the formation of a specific architecture. Interactions between SBPs and materials are dictated by amino acid sequence, amino acid composition, and peptide conformation, both in solution and upon adsorption to interfaces. Appending SBPs to the N- or C-termini of proteins and/or inserting them at permissive internal locations also influences outcomes because local SBP conformation, proximal scaffold residues and even distal features can influence binding and/or mineralization events. Thus, not only is an understanding of biotic-abiotic interactions hard to come by, but what is learned with one set of SBPs does not necessarily provide information on the behavior of another[71]. For example, it has been shown that while certain silica-mineralizing proteins only

function in the presence of phosphate – an additive believed to enable the formation of large aggregates necessary for silica polycondensation – others have no need for it but require an acidic environment to hydrolyze silica precursors.[72, 73] Additives and reaction conditions are also important in inorganic morphogenesis. For instance, addition of alcohols to a silica precursor solution was found to cause a five-fold reduction in the size of the silica particles formed, while conducting precipitation under flow conditions changed the silica morphology formed from spherical particles to intertwined fibers.[73] This variety of outcomes indicates that careful control of conditions is needed when pursuing inorganic synthesis with solid binding peptides and proteins.

1.2 Quantum dots

Quantum dots (QDs) are fluorescent semiconductor nanocrystals that exhibit electronic properties distinct from the bulk because their size is smaller than the Böhr exciton radius of the constituent material.[74-76] Within this size range (2-10 nm, depending on composition) electrons are confined in all directions, and as a result of this quantum confinement the bandgap becomes dependent on size.[77] Cadmium selenide (CdSe) is one of the most commonly used materials to produce QD cores. Its bulk bandgap is 1.7 eV (730 nm), but CdSe QDs of 2 nm diameter have a bandgap of 2.4 eV (516 nm).[78, 79] As the particle diameter increases, the bandgap decreases, which red-shifts the emission wavelength, and this trend continues until the electronic properties resemble those of the bulk material at sufficiently large diameter.[80] In addition to CdSe, a number of II-VI semiconductor pairings (CdS[81-83], CdTe[84-87], ZnSe[88-90]), III-V (InP[91-93], InAs[94-96], GaAs[97, 98]), and IV-VI (PbS[99, 100], PbSe[100-102]) pairings have been used to produce QDs. An illustration of

the impressive variety of QD spectral properties as a function of composition and size is provided in **Figure 1.3**.[103]

Early QD synthesis schemes led to nanocrystals with quantum yields (photons emitted per photons absorbed) inferior to 10%[104] because surface defects caused undesirable electron-hole recombination (the so-called trap states).[105] It was however later found that core-shell architectures in which a larger bandgap material (e.g., ZnS) coats the surface of a smaller bandgap nanocrystal (e.g., CdSe), drastically reduced non-radiative recombination events and improved fluorescence yields.[106, 107] Indeed, CdSe-ZnS core-shell QDs can exhibit quantum yields of 40-70%[106-109], and further innovation in synthesis, especially the use of gradient shell layers, has pushed these values towards unity.[110-112]

Because of their broad excitation ranges, size-tunable emissions, large Stoke shifts, and resistance to photobleaching, QDs have gained in popularity over organic fluorophores. Applications include bioimaging,[113] analytical assays,[114] electronic displays,[115] solid-state lighting,[116] and photovoltaics,[117] with a global market expected to reach $3.1 billion by 2018[118]. As of 2016, Samsung, Sony, and LG[119] are all selling televisions containing QDs as part of their backlighting system. In such electronic applications, QDs are coated with the hydrophobic capping agents they are typically synthesized in (*e.g.,* tri-n-octylphosphine oxide, TOPO).[79, 108, 120] However, for bioimaging or bioassay applications, they must be made water-soluble. Methods to do so include encapsulating nanocrystals within phospholipid block-copolymer micelles[121], modifying their surface with amphiphilic polymers such as polyacrylic acid[122] or polyethylene glycol (PEG)[123, 124], or coating them with a layer of silica.[125-128] Thiol-containing agents such as mercaptoacetic acid (MAA) have been used to covalently couple proteins and antibodies to QDs because they bind to the ZnS shell via thiol coordination and contain a carboxylic acid group that

can be used for the chemical conjugation of biomolecules.[129-131] Alternative approaches include the use of thioglycolic acid to stabilize QDs followed by EDC-NHS (1-Ethyl-3-(3-dimethylaminopropyl)carbodiimide - N-Hydroxysuccinimide) click chemistry for protein conjugation,[132] or coating the nanocrystals with silica which can be functionalized with thiols, PEG, amine, or carboxylate groups.[127, 133, 134] For oligonucleotide conjugation, the TOPO layer has been replaced by dithiothreitol (DTT) and subsequent treatment with 1,1′-carbonyl diimidazole (CDI) to create QDs with an imidazole−carbamate surface, which allows for the conjugation of 5'-aminated oligonucleotides through a carbamate bond.[135] These various conjugation chemistries have allowed the use of QDs in bioimaging.[136-138] As QDs become more prevalent in consumer products that will be reused, recycled, and landfilled, concerns have been rising about their impact on humans and the environment.[139]

1.2.1 Toxicity concerns

Engineered nanomaterials have raised environmental health and safety concerns because of their high reactivity and surface area, and in some cases (e.g. QDs) their composite materials.[140] Studies conducted with cultured eukaryotic cell lines have revealed that QDs can exert cytotoxic effects through a variety of mechanisms. These include leaching of toxic heavy metals (Cd, Se, Te) from the nanocrystal core, (photo)generation of reactive oxygen species, primarily superoxide anion radicals[141] that cause oxidative stress, and direct or indirect damage to DNA and biological membranes.[142-146] QD size, shape, composition, and surface coating(s) can significantly impact cytotoxicity outcomes and do so in a mechanism-specific (and cell-specific)[147] manner. For instance, while ZnS or polymer coatings have been shown to reduce the cellular toxicity of CdSe nanocrystals,[144] these surface modifications do little to prevent photo-induced DNA damage.[142]

While QDs with a hydrodynamic diameter inferior to 5.5 nm are readily cleared by the kidneys,[148] there is still concern about the potential for proinflammatory effects in animals, where the situation is further complicated by the exposure route, and where the primary concern is the long-term retention in the liver, spleen, kidney, and lymph nodes.[143, 149, 150]

There is considerably less information on the interaction of QDs and prokaryotes although these abundant organisms will be first to come into contact with nanomaterials that find their way into the environment. Additionally, there are concerns regarding the interactions of these and other nanomaterials with the intestinal microbiome, which is critically important for our health.[151] Furthermore, most available studies have been conducted with cadmium-based (CdS, CdSe and CdTe) QDs using different synthesis schemes, coatings, doses, strains, and culture conditions.[152-154] In *Chapter 2*, we utilize a minimized designer protein for the fabrication of manganese (Mn)-doped ZnS QDs, and in *Chapter 3* we investigate how these protein-coated QDs interact with *E. coli* with an emphasis on how they translocate to the cell cytoplasm, the physiological stresses that they induce, and their persistence in metabolically active cultures.

1.3 Green fluorescent protein

Green fluorescent protein (GFP) was discovered in Puget Sound in 1962 as the source of fluorescence in the jellyfish *Aequorea Victoria*, but only captured the limelight after its structural gene was cloned and the protein expressed in *E. coli* in 1992.[155, 156] Within a few years the crystal structure had been solved,[157] and laboratories around the world began to use its fluorescent properties to track cell movements[158, 159], interrogate cell mechanisms[160], monitor gene expression.[161-164] and report on intracellular redox states.[165]

GFP is organized as a β-barrel consisting of 11 β-strands wrapped around a central α-helix that contains the chromophore. The minimal chromophore is a Ser-dehydroTyr-Gly sequence at positions 65-67, while the full version is a hexapeptide extending from residues 64 to 69.[166, 167] The chromophore forms co-currently with the folding process and no co-factor or additive is required for fluorescence emission.[167] For the wild type protein, maximum absorption occurs at 395 nm and there is a weak secondary excitation peak at 475 nm with maximum emission at 510 nm.[168] The protein is approximately 24 Å in diameter and 42 Å tall and both its N- and C- termini project from the "bottom" face of the β-barrel (**Figure 1.4**)

Wild-type GFP suffers from long maturation times (1-2 hours)[168] and poor solubility (25%)[169, 170] when expressed at physiological temperatures in *E. coli*. These undesirable phenotypes launched a search for mutations that would improve GFP folding. Although many mutations were found to improve solubility and fluorescence characteristics,[171, 172] the combination of 3 substitutions (F99S, M153T and V163A) along with optimization of codon usage yielded the widely used "cycle-3" mutant.[169] In 1997, two additional mutations (F64L and S65T) were found to drastically improve GFP fluorescence. The resulting enhanced GFP (eGFP, also known as GFP-mut2) became the gold-standard for the next 8 years.[170] In 2005, Waldo *et al* isolated six mutations (S30R, Y39N, N105T, Y145F, I171V, and A206V) that, when combined with the 5 substitutions present in eGFP, produced a highly soluble protein resistant to unfolding that was christened superfolder GFP (sfGFP).[173] This new variant has a 2.5-times higher fluorescence intensity than eGFP, and is about 50% more resistant to unfolding in urea. The excitation maximum is at 485 nm and the emission maximum is at 510 nm.

Besides improvements in folding or fluorescence, GFP has been engineered for new uses. Blue-shifted variants have been identified and employed with the parental protein to label multiple

sites in a single fluorescent image;[174] yellow fluorescent mutants (YFP) have been combined with cyan fluorescent mutants (CFP) as a FRET (Förster resonance energy transfer) pair;[175-177] and split GFP fragments that recover fluorescence upon spontaneous or directed reassembly have been used as solubility sensors, the identification of interacting protein pairs, and as binding partners for protein crystallization.[178, 179]

Permissive sites are locations in proteins that tolerate the insertion of extraneous amino acids without impacting the ability of the protein to fold or function.[180] These regions often, but not always, map to solvent exposed loops and are usually identified by linker or transposon mutagenesis.[181] Model proteins such as β-lactamase and maltose binding protein (MBP) contain permissive sites that have been exploited for the development of chimeras ranging from immunogen presenters[182] to allosteric dual-enzymes.[183-186] To identify permissive sites in GFP, Abedi and coworkers inserted 20 residue-long peptides within each of its loops and evaluated the resulting constructs for fluorescence.[187] This study revealed that only loop 8 (amino acids 155-160) and loop 9 (170-176) tolerate insertions without losing function. These loops are located on the "bottom" face and "top" faces of the β-barrel and are highlighted in **Figure 1.4**. In *Chapter 4*, we make use of the accessible termini and of the 172-173 permissive loop to build a multifunctional variant of superfolder GFP.

1.4 Carbon nanotubes

Carbon naturally occurs in one of two structures: sp^2-hybridized rings, known in bulk as graphite, or an sp^3-hybridized face-centered cubic lattice, known as diamond (**Figure 1.5**). Carbon nanotubes (CNTs), a carbon nanostructure discovered in 1991,[188] are best described as a single graphene sheet rolled along its length into a tube. These tubes can be single-walled or be comprised

of concentric layers that form a multi-walled CNT. A visualization of the chiral variants of CNTs, which depend on the angle at which the tube is rolled, is also shown in **Figure 1.6**.[189, 190] These differences in chirality determine whether CNTs function as semiconductors or as metals in terms of electron propogation.[191, 192] Since their discovery, CNTs have been extensively studied for use in transistors[193, 194], supercapacitors[195], and additives for carbon fiber composites.[191, 196, 197] They have potential for a broad range of other applications due their attractive electronic, thermal, optical and mechanical properties. For example, CNTs have 100-fold the conductivity[198] and 10-times the heat transfer rate[199] of the industrial main-stay, copper.

CNTs are difficult to disperse in aqueous solutions because of their hydrophobic nature. This can be overcome by treatment with strong acids to create carboxylic acid groups on the CNT surface, but the treatment also disrupts the carbon lattice responsible for electronic properties.[200] To circumvent this problem, non-covalent solubilization approaches have been explored. One of these, dispersion in the detergent sodium dodecyl sulfate (SDS), has proven particularly useful, because it does not damage CNT structure or alter their desirable electronic properties.[201, 202] However, controlled patterning and alignment of CNTs, which is necessary for the production of reliable[194] and competitive[203, 204] electronic devices remains difficult. One approach involves chemical-vapor-deposition (CVD) of CNTs on previously patterned silicon or quartz substrates.[205] Unfortunately, this strategy does not allow for the separation of metallic and semiconducting CNTs, which is necessary for the production of transistor devices.[206] Although there has been recent progress in the formation of purely semiconducting CNT arrays by exploiting nanoscale thermocapillary flow to remove metallic tubes[207], improvements will be needed before practical devices can be made.[204]

Because the electrical properties of CNTs are so sensitive to their environment[208], they have been utilized in biosensor construction.[209] These sensors are primarily built by conjugating an analyte-binding species to the carboxylated ends of CNTs. With this approach, devices that allow glucose or DNA biosensing have been demonstrated.[210-212] The high aspect ratio of CNTs also allows them to penetrate cell membranes, and such membrane-spanning CNTs have been used for the transport and delivery of both proteins[213] and DNA[214] into cells. In *Chapter 5*, we demonstrate the end-labeling of single-walled CNTs without any chemical modifications through the use of a peptide affinity tag.

1.5 Figures

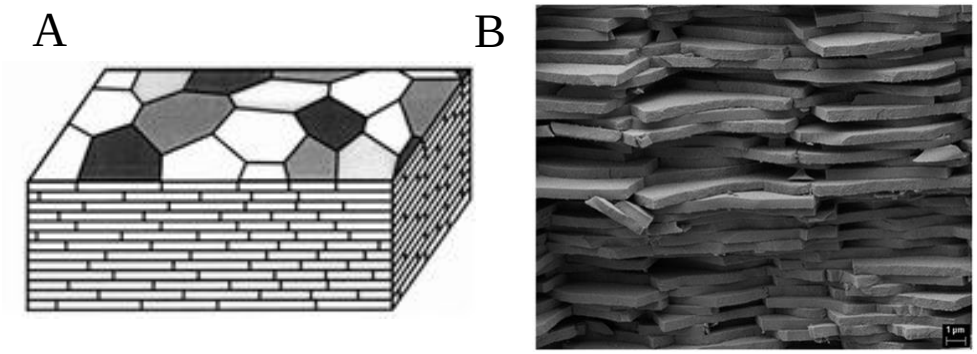

Figure 0.1 A) A representation of the aragonite platelets forming sheet nacre (adapted from ref. 18 Sun *et al.)* B) SEM micrograph of a fracture plane of nacre (adapted from ref. 19 Behr *et al.)*

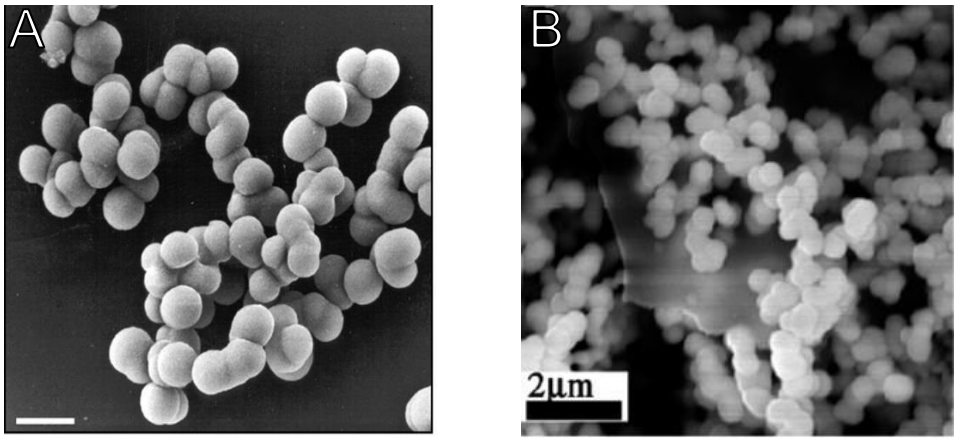

Figure 0.2 Silica precipitation induced by silaffins. A) SEM micrograph of silica precipitated by silaffin-1A adapted from ref. 20 Marner *et al*. The diameter of silica particles is 500 to 700 nm. The protein concentration was 5 mg/ml. Bar: 1 µm. B) SEM micrograph of silica spheres from the R5 peptide, a derivative of silaffin-1A, adapted from ref. 21 Kröger *et al*.

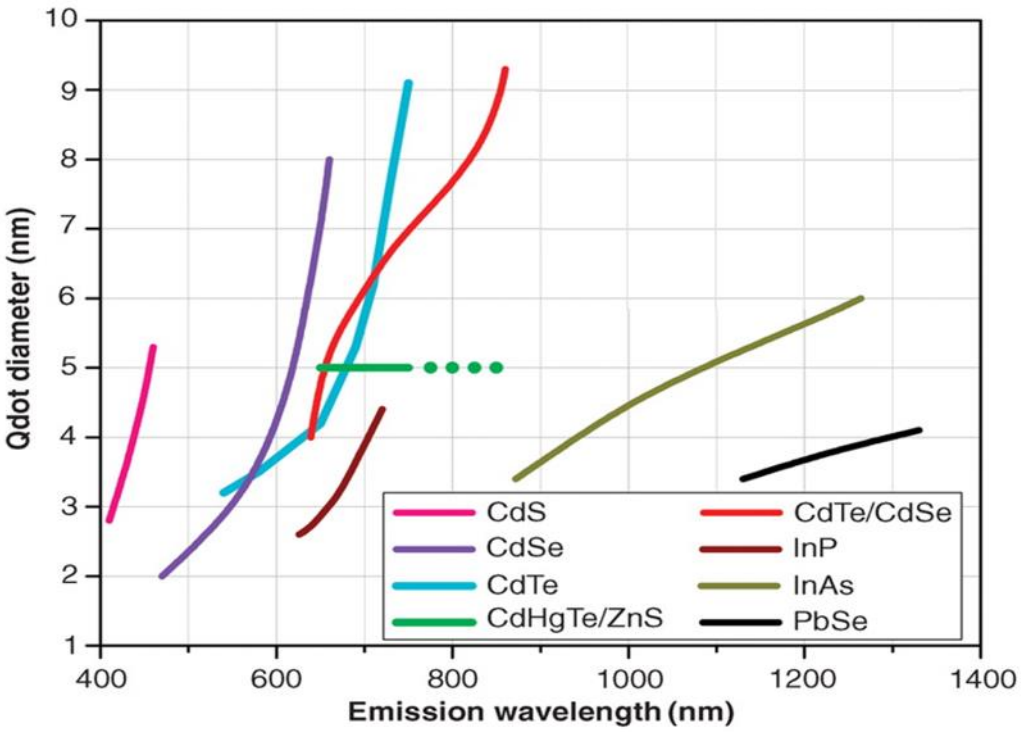

Figure 0.3 Both QD composition and size affect emission properties. Adapted from ref. 67 Michalet *et al*

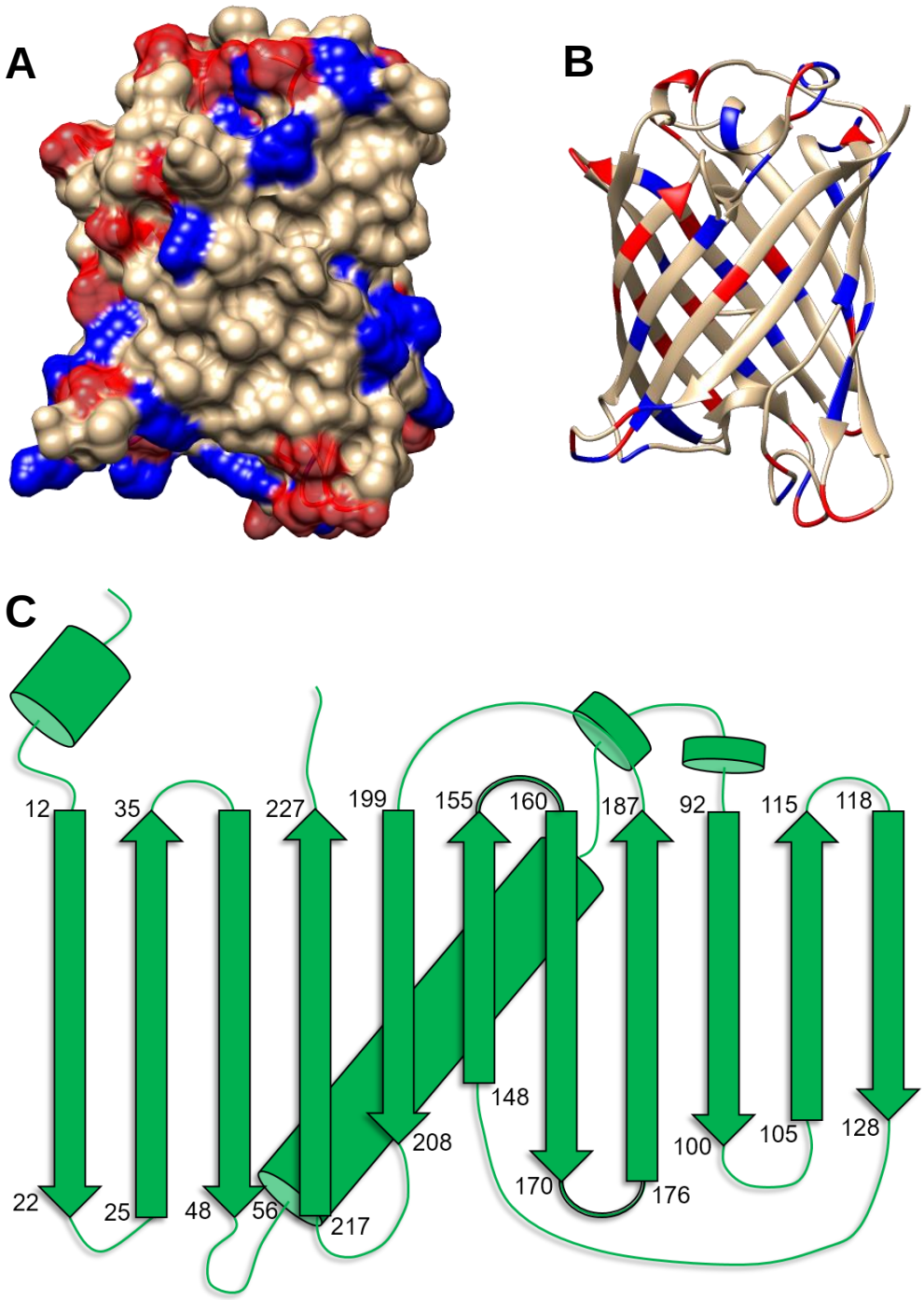

Figure 0.4 3-D Molecular surface (A) and ribbon structure (B) of sfGFP. Basic amino acids (Arg, Lys, and His) are colored blue while acidic residues (Glu, Asp) are colored red. C) 2-D ribbon structure of sfGFP with permissive loops 8 and 9 in bold.

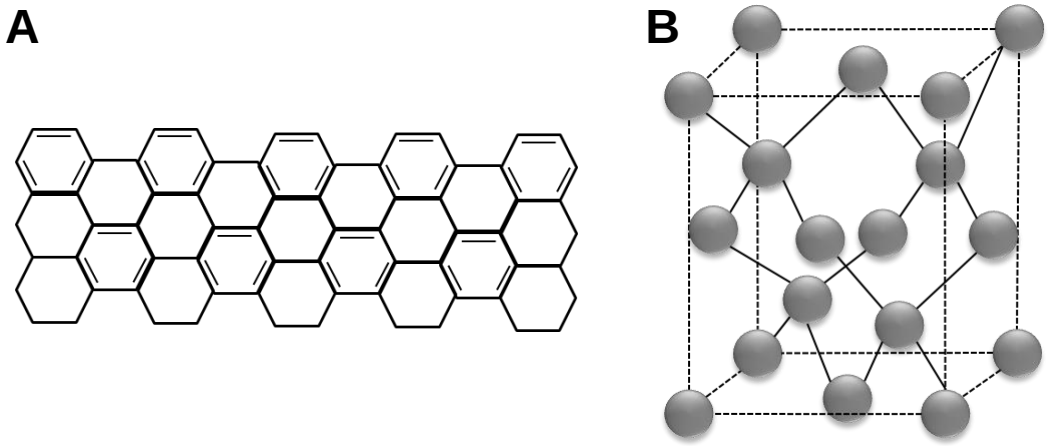

Figure 0.5 Carbon has two natural crystal structures, sp^2-hybridized graphite (A) and sp^3-hybridized diamond.

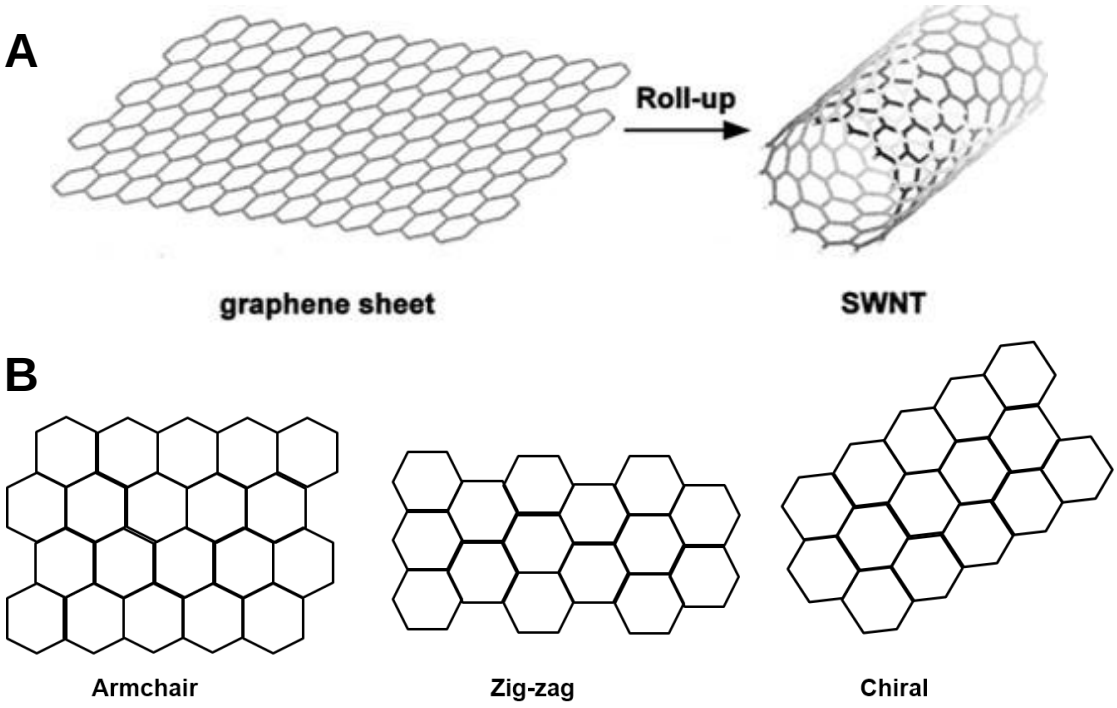

Figure 0.6 A) Single walled carbon nanotubes are best described as a single graphene sheet rolled up along one axis. Adapted from ref. 186 Odom et al. B) Their chirality is determined by their pattern along their long axis: armchair, metallic; zig-zag, semi-conducting; chiral, semi-conducting.

A minimized designer protein for facile biofabrication of ZnS:Mn immuno-quantum dots

1.6 Introduction

The fabrication of protein-coated quantum dots (QDs) benign to humans and the environment is a complex and time-consuming process that is further complicated by the inherent toxicity of commonly used core materials (*e.g.*, CdSe) and by the need for polymer coatings and secondary functional groups[215-218] which can exert a deleterious effect on biological systems.[219] To circumvent these limitations, we previously built a "designer" protein that supports the aqueous and one-pot synthesis of undoped and manganese-doped ZnS QDs whose crystalline cores are approximately 4 nm in diameter.[220, 221] The 27-kDa BB-TrxA::CT43 fusion protein (**Figure 0.1**) consists of an antibody-binding domain derived from S. aureus protein A (BB) followed by a disulfide-constrained ZnS-binding peptide (CT43) inserted within the active site loop of E. coli Thioredoxin A (TrxA). BB-TrxA::CT43 prevents uncontrolled precipitation of ZnS (or ZnS:Mn) via CT43-dependent capping and allows for rapid production of immuno-QDs by BB-mediated conjugation of antibodies to protein-stabilized nanocrystals.[220, 221]

From a bio-imaging perspective, nanoparticles with small hydrodynamic diameters (D_h) are preferable to larger ones because they are more efficiently transported to a variety of tissues and subcellular locations.[222] Small QDs ($\leq$ 10 nm) are also desirable from a toxicological standpoint because they are more readily cleared from the circulation by the renal system.[148] For our biofabricated QDs, reducing D_h means decreasing the size of the designer protein without affecting it ability to stabilize nanocrystals. If antibody-binding functionality is to be maintained,

this means truncating or eliminating the TrxA domain while repositioning the CT43 motif as a fusion to BB.

The CT43 dodecapeptide was identified as one of several ZnS binders from a screen of the FliTrx flagellar display library.[221, 223] In the original display system, and in the BB-TrxA::CT43 designer protein, CT43 is presented to the solvent in a disulfide-bonded loop that reduces its flexibility and available degrees of freedom (**Figure 0.1**). This has important consequences on inorganic binding since conversion from circular to linear topology often reduces or even entirely eliminates the ability of solid binding peptides (SBPs) to interact with their cognate materials.[224-226] For nucleation and growth processes, a decrease in affinity means less efficient capping and the production of larger particles.[227, 228] On the other hand, certain disulfide-bonded SBPs are largely unaffected by linearization,[225, 226] and conversion of certain binders to a linear configuration has even been reported to increase inorganic affinity.[229]

1.7 Materials and methods

1.7.1 DNA manipulations

Plasmid pBB-CT43, which encodes a fusion protein between tandem repeat antibody-binding domains from S. aureus protein A (BB segment) and the Zn-binding peptide CT43 under transcriptional control of the T7 promoter, was constructed as follows. Two phosphorylated primers, 5'-CTAGGGGTGGCGGAGGTAGCGCGGGTGATAGTAGTGGGGTGGACAGTC GCAGTGTTTAATGAC-3' and 5'TTAAGTCATTAAACACTGCGACTGTCCACCCCACTA CTATCACCCGCGCTACCTCCGCCACCC-3', were annealed by boiling in a water bath for 10 min followed by air cooling. Backbone DNA was amplified from plasmid pBB-Trx::CT431 using primers 5'-GCGTCGACCTTAAGTAATCGTACAGGGTAGT-3' and 5'-GGTTTCCGGGGATCCTC GCTATTTT-3' to introduce *AvrII* and *AflII* sites at 5' and 3' ends,

respectively. Hybridized primers and backbone were ligated at a 5:1 ratio. Construct integrity was verified by sequencing.

1.7.2 Protein purification and nanocrystal synthesis

BB-TrxA::CT43 was purified as previously described.[221] BB-CT43 was purified by a similar procedure. Briefly, BL21(DE3) cells harboring pBB-CT43 were grown at 37° C in LB medium supplemented with 34 μg/mL chloramphenicol to $A_{600} \approx 0.4$ and protein expression was induced by addition of 0.4 mM IPTG (Isopropyl β-D-1-thiogalactopyranoside). After a 4h incubation at 37° C, cells were sedimented by centrifugation at 3,500g for 10 min, resuspended in 20 mM Tris-HCl, pH 7.5, 2.5 mM EDTA, 1 mM PMSF to $A_{600} \approx 50$, and disrupted with a French press. Lysates were clarified by centrifugation at 14,000g for 10 min and supernatants were loaded onto a Q Sepharose FF column (6.0 x 1.0 cm inner diameter) equilibrated in 20 mM Tris-HCl, pH 7.5. Contaminants were removed by washing with 20 mL of the same buffer at 1 mL/min. Bound proteins were eluted over 1h using a 0 to 250 mM NaCl linear gradient. Fractions containing pure BB-CT43 (eluting at ≈ 100 mM NaCl) were pooled and desalted by dialysis against 20 mM Tris-HCl, pH 7.5 using 3 kDa-cutoff SnakeSkin dialysis tubing (Thermo Scientific). Protein-capped Mn-doped ZnS nanocrystals were synthesized as previously described[220] using 5 μM of purified BB-CT43 or BB-TrxA::CT43 and stored at 4° C, a temperature at which they are stable for months.

1.7.3 Agarose gel electrophoresis

ZnS:Mn quantum dots prepared with BB-CT43- or BB-TrxA::CT43 were concentrated ≈ 4 times by centrifugation at 4,000 g using an Amicon Ultra-4 centrifugal filter (MWCO 3 kDa, Millipore). The retentate was assayed for protein concentration (assumed to be quantitatively bound to nanocrystals) using a Bradford assay (Pierce). The typical concentration of fusion protein was 0.2 mg/mL (7.5 μM). Human IgG purified immunoglobin (Sigma) was dissolved to a 2 mg/mL

(13.3 μM) concentration in buffer A (100 mM Tris-HCl, pH 7.5, 150 mM NaCl). ZnS:Mn nanocrystals (30 μL) were mixed with IgG to a molar ratio of IgG to BB-CT43 (or BB-TrxA::CT43) of 1 to 5 and the final volume was adjusted to 60 μL with buffer A. After 1h incubation at 4° C with slow shaking, immunocomplexes were mixed with 10 μL of 5X sample buffer (50% glycerol, 0.1% Bromophenol Blue, 0.12 M Tris base), and aliquots were loaded onto 0.75% agarose gels made in running buffer (25 mM Tris, 19.2 mM glycine, pH 8.5). The gel was submerged in running buffer and electrophoresis was performed at a constant voltage of 50 V for 45 min at room temperature. Fluorescent bands were detected by illumination on a UV transilluminator operating at 303 nm. To quantify the fraction of QDs decorated with antibodies, we converted fluorescence images to gray scale and used Image J analysis software to integrate the total fluorescence signal in lane 3 and in lane 4. We next integrated the fluorescence peak corresponding to antibody-free quantum dots and subtracted this result from total fluorescence measurements to obtain the amount of antibody-bound material. Results were normalized to a total fluorescence of 1 to obtain values of 60% antibody decoration for BB-TrxA::CT43-stabilized nanocrystals and 70% for BB-CT43-stabilized nanocrystals. The experiment was repeated twice with similar results.

1.7.4 Analytical techniques

UV-visible absorption spectra were recorded on a Beckman DU640 spectrophotometer. Fluorescence and phosphorescence emission spectra were recorded using 1 mL of sample on a Hitachi F4500 fluorescence spectrophotometer with excitation at 280 nm and excitation and emission slit widths set at 2.5 nm (fluorescence) or excitation at 316 nm and excitation and emission slit width at 2.5 nm and 10 nm, respectively (phosphorescence). The wavelength region corresponding to the second order diffraction peak of the excitation light was omitted.

Hydrodynamic diameters and zeta potentials were measured on 1 mL samples using a Malvern Zetasizer Nano-ZS dynamic light scattering instrument equipped with a 633 nm laser filter. Data were fit with a Gaussian distribution to determine standard deviations.

1.8 Results and discussion

1.8.1 The effects of CT43 linearization

To determine if an unconstrained version of CT43 would remain capable of supporting QD synthesis, we used site directed mutagenesis to convert the first and second cysteine of BB-TrxA::CT43 to serine. The resulting proteins, BB-TrxA::CT43-C32S and BB-TrxA::CT43-C35S (using the numbering system of native TrxA) were purified to homogeneity along with the wild type and proteins were used at a 5 μM concentration to synthesize ZnS:Mn QDs by dropwise addition of sodium sulfite to a precursor solution of zinc and manganese.[220] After 5 days of aging at 37° C, all solutions were bright orange under UV illumination and D_h measured by dynamic light scattering were comparable for all suspensions (~15 nm). Nevertheless, maximum emission intensities at 590 nm, a wavelength characteristic of the 4T1→6A1 Mn2+ transition, were 10% and 16% lower when the C32S or C35S variants (respectively) were used. We conclude that although the disulfide-bonded conformation of CT43 is not required for efficient QD biofabrication, it exerts a small positive impact on its optical properties.

Consistent with the fact that elimination of TrxA yields a protein that is 25% more compact than its parent (**Figure 2.1A-B**), the mean D_h of particles biofabricated with BB-CT43 was 9.5 ± 2 nm compared to 15 ± 3 nm for BB-TrxA::CT43-stabilized nanocrystals (**Figure 2.1F**). Also as expected from the lower zeta potential (ζ) of BB-CT43 (**Figure 2.1A-B**), QDs made with the minimized protein had a ζ of –16.5 ± 6 mV relative to –30 ± 10 mV for particles produced with the full-length protein (Fig. 1F). This change in charge did not affect colloidal stability. BB-CT43-

capped QDs retained their optical properties over months of storage at 4° C and did not aggregate or experience significant fluorescence loss when exposed to pH ranging from 7 to 9 and salt concentrations as high as 500 mM NaCl (**Figure 2.2**). Additionally, there was no significant change in colloidal or optical properties following one week of incubation under physiological conditions (37° C, 150 mM NaCl). It is therefore likely that steric exclusion effects play an important role in particle stabilization.[143] On the other hand, BB-CT43-stabilized nanocrystals were sensitive to acidification (**Figure 2.2**), just like particles produced with BB-TrxA::CT43.[220]

1.8.2 Retention of immuno-functionality

To demonstrate that the BB domain of the minimized protein was functional for antibody binding, QDs fabricated with BB-TrxA::CT43 or BB-CT43 were fractionated on 0.75% agarose gels.[220, 221] In the absence of additive, both colloidal suspensions migrated as tight bands (**Figure 2.3**) with BB-CT43-stabilized QDs traveling closer to the cathode (at the bottom of the gel) due to their smaller D_h. Incubation with human immunoglobulin G (IgG) at a 1:5 molar ratio of antibody to designer protein led to a decrease in the intensities of these bands and to the concomitant appearance of fluorescent material migrating closer to the loading wells (lanes 2 and 3). These species, which correspond to antibody-derivatized QDs,[220] accounted for 60% of the total fluorescence for QDs made with BB-TrxA::CT43 and 70% of the total fluorescence for nanocrystals produced with BB-CT43. Thus, antibody decoration is slightly more efficient with BB-CT43-stabilized QDs, perhaps because the BB domain is more accessible to the solvent. In support of this hypothesis, BB-CT43-based immuno-QDs migrated over a broader range of positions compared to those produced with BB-TrxA::CT43, which suggests that they are decorated with different numbers of antibodies (we previously calculated that 5 to 6 designer

protein molecules stabilize each nanocrystal which means that up to 6 antibody molecules might bind to a QD).[220]

1.9 Conclusions

In summary, we have shown that a minimal version of BB-TrxA::CT43 consisting of the *S. aureus* BB antibody binding domain fused to a linear version of CT43 remains functional for the facile biofabrication of luminescent ZnS:Mn nanocrystals. QDs produced with the minimized protein are as stable as those made with BB-TrxA:CT43, but 30% brighter and more accessible for antibody binding. A one-third reduction in D_h should make these optical probes more versatile and less toxic for biological imaging applications.

1.10 Figures

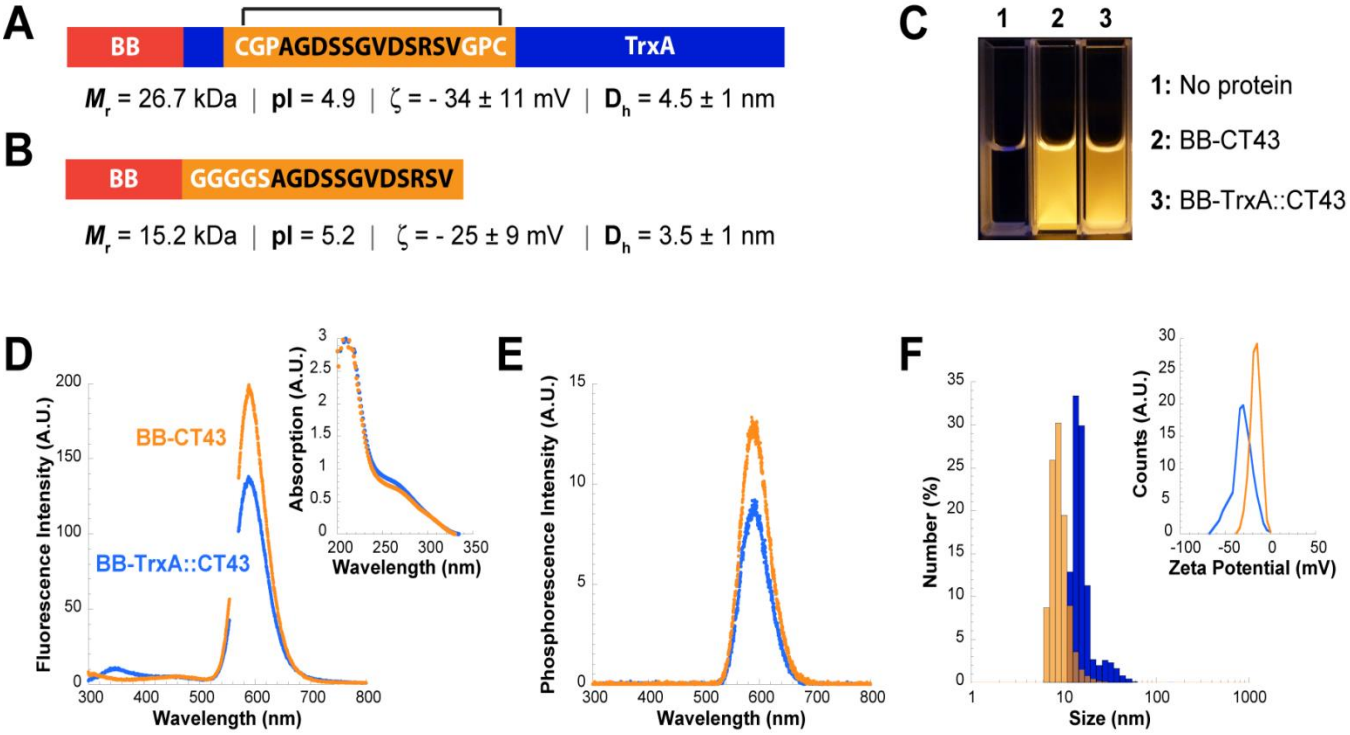

Figure 0.1 Comparison of the properties of ZnS:Mn nanocrystals biofabricated with the BB-TrxA::CT43 and BB-CT43 designer proteins. Schematic structures of BB-TrxA::CT43 (A) and BB-CT43 (B). The antibody-binding BB domain is in red, TrxA in blue and the ZnS-binding region in orange. The amino acid sequence of the CT43 peptide is in black and invariant tripeptides (A) or flexible linker (B) in white using the one letter code. The disulfide bond between cysteine residues is shown in the case of BB-TrxA::CT43. Calculated molecular mass and pI, and measured zeta potential and hydrodynamic diameters for the purified proteins are shown below the sketches. (C) Appearance of ZnS:Mn nanocrystals fabricated with 5 µM of BB-CT43 or BB-TrxA::CT43 under UV illumination. (D) Fluorescence emission spectra of nanocrystals produced with BB-CT43 (orange) or BB-TrxA::CT43 (blue) after excitation at 280 nm. The inset shows the corresponding absorption spectra. (E) Phosphorescence emission spectra after excitation at 280 nm. (F) Distribution of hydrodynamic diameters for nanocrystals produced with BB-CT43 (orange) or BB-TrxA::CT43 (blue). The inset shows the corresponding zeta potentials.

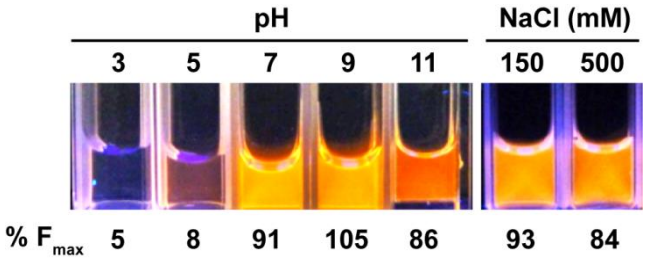

Figure 0.2 Stability of ZnS:Mn nanocrystals fabricated with BB-CT43. Colloidal suspensions were photographed under UV illumination 1h after pH adjustment with 0.1 M HCl or NaOH, or after addition of the indicated NaCl concentration. Numbers below samples correspond to the ratio of maximum fluorescence intensity at 590 nm (λ_{ex} = 280 nm) to that of a control QD solution synthesized at the standard pH of 8.2.

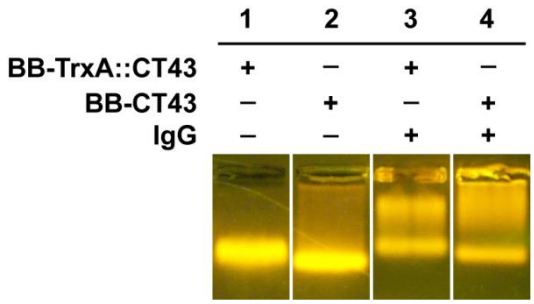

Figure 0.3 Production of immuno-QDs. ZnS:Mn nanocrystals fabricated with 5 µM of BB-TrxA::CT43 or BB-CT43 were fractionated on a 0.75% agarose gel in the absence of additive (lanes 1 and 2) or after 1h incubation with 1 µM human IgG (lanes 3 and 4).

Microbial uptake, toxicity, and fate of biofabricated ZnS:Mn nanocrystals

1.11 Introduction

Quantum dots (QDs) are semiconductor nanocrystals that are gaining in popularity over organic fluorophores in applications ranging from bioimaging[230] and analytical assays[231] to electronic displays,[232] solid-state lighting[233] and photovoltaics.[234] QDs commonly consist of a CdSe, CdTe, ZnSe, or PbSe core coated with a ZnS shell to enhance stability and optical properties. In some cases, the shell is further functionalized with thiols or amphiphilic polymers to make the nanocrystals soluble in aqueous solvents and to allow for biomolecule conjugation.[215-217] As QDs become more prevalent in consumer products that will be used, reused, recycled, and landfilled, concerns have been rising about their impact on humans and the environment.[235]

Studies conducted with cultured eukaryotic cells have revealed that QDs can exert cytotoxic effects through a variety of mechanisms. These include leaching of toxic heavy metals from the inorganic core, (photo)generation of reactive oxygen species that induce oxidative stress, and direct or indirect damage to genomic DNA and biological membranes.[215, 236-239] Parameters such as size, shape, composition, and surface coating(s) can all impact cytotoxicity outcomes and do so in a mechanism-specific (and cell-specific) [240] manner. For instance, while ZnS shells or polymer coatings can reduce the cellular toxicity of CdSe nanocrystals,[237] they do little to prevent photo-induced DNA damage.[241] Similar observations have been made in animals, where the situation is further complicated by the route of exposure and where long-term retention in the liver, spleen, kidney, and lymph nodes is of primary concern.[236, 242, 243]

There is considerably less information on how QDs interact with prokaryotes although these abundant microorganisms will be first to come into contact with engineered nanomaterials that find their way into the environment. Furthermore, most studies conducted to date have focused on cadmium-based QDs (CdS, CdSe and CdTe cores) produced with different synthesis schemes and coatings, and used at different doses with a variety of strains and culture conditions.[244-246]

To answer a growing demand for the production of functional nanomaterials through environmentally friendly processes, we previously described a set of "designer" proteins that support the low-temperature and aqueous fabrication of undoped and transition metal-doped ZnS QDs to which antibodies can be conjugated by simple mixing.[220, 221, 247] Because zinc is not as toxic as cadmium,[248] these particles should exhibit low cellular toxicity upon core dissolution, and because they are capped by proteins as part of the manufacturing process, their shell is already biologically-relevant.

Here, we used *E. coli* as a model organism to investigate the penetration requirements, subcellular localization, induction of stress responses, and long-term fate of luminescent ZnS:Mn nanocrystals fabricated with a minimized designer protein.[247] Our results suggest that such protein-coated fluorophores are likely to be benign toward prokaryotes because their uptake requires membrane destabilization, they only induce oxidative stress at high doses, and they are rapidly diluted by cell division.

1.12 Materials and Methods

1.12.1 QD uptake by competent cells

AB734, an E. coli K-12 strain containing a mutation in the *lacZ* gene but otherwise wild type was obtained from the E. coli Genetic Stock Center. To prepare competent cells, 500 mL

cultures were grown in LB medium at 37° C to A600 ≈ 0.4, and cells were sedimented by centrifugation at 8,000g for 8 min and resuspended in 100 mL of 100 mM $CaCl_2$ or phosphate buffered saline (PBS;150 mM NaCl, 10 mM Na_2HPO_4, 2 mM KH_2PO_4). After 30 min incubation on ice and centrifugation at 8,000 g for 8 min, cells were resuspended into 12.5 mL of 100 mM $CaCl_2$ (or PBS for a non-competent control) and held on ice overnight. Glycerol was added to a 10% (v/v) final concentration and aliquots (200 μL) were stored at -80° C for future use. For uptake experiments, competent or control cells were thawed at room temperature, washed twice with PBS with an intervening cycle of centrifugation at 4,000 rpm for 5 min in a microfuge, and resuspended in 900 μL of the same buffer. QDs (approximately 100 μL for a dose of 0.5 μg/mL) were added and the mixture was incubated at room temperature for 2h without shaking. Cells were washed twice with PBS to remove unincorporated QDs.

1.12.2 QD subcellular localization

Cells that had taken up QDs were stripped of their outer membrane and peptidoglycan layer by spheroplasting.[249] Briefly, samples prepared as above were resuspended in 200 μL of buffer A (100 mM Tris-HCl, pH 8.0, 0.5 M sucrose, 0.5 mM EDTA), and 10 μL of a 2 mg/mL solution of lysozyme was added, followed by 400 μL buffer A, and 400 μL of ddH2O. After 20 min at room temperature, spheroplasts were recovered by centrifugation at 12,800 g for 30 s and resuspended in 100 mM Tris-HCl, pH 8.0, 0.3 M sucrose, and 10 mM $MgCl_2$. Samples were visualized on an optical microscope at 50x magnification.

1.12.3 FRET experiments

AB734 (pmCherry-mut2) cultures were grown to A600 = 0.2 at 37° C in LB medium supplemented with 50 μg/mL kanamycin. Production of mCherry was induced by addition of 0.2% L-arabinose and cultures were collected after 3 h of growth at 37° C. Cells were made competent

by $CaCl_2$ and ice treatment as above and stored in 200 µL aliquots. After two wash cycles and resuspension in 900 µL PBS, one sample was incubated for 2 h with 100 µL of BB-CT43-stabilized QDs or the same volume of PBS to serve as a control. After 2 wash cycles with PBS, samples were diluted 20-fold in PBS and fluorescence emission spectra were recorded with excitation at 280 nm or 590 nm. Control samples of AB734 cells lacking the pmCherry-mut2 plasmid and incubated or not with QDs were prepared as above and fluorescence spectra were recorded following excitation at 280 nm. The spectra of Fig. 4 show QD-free AB734 emission subtracted from QD-treated AB734 emission with excitation at 280 nm (orange), and QD-free mCherry-producing AB734 subtracted from QD-treated mCherry-producing AB734 with excitation at 280 nm (red).

1.12.4 QD fate

Aliquots (200 µL) of AB734 cells that had taken up QDs as above were used to inoculate 2 mL of LB media in multiple 15 mL culture tubes supplemented or not with 50 µg/mL of the translational inhibitor kanamycin. Cultures were transferred to a 37° C water bath. At the indicated time points, culture absorbance was recorded at 600 nm and samples (2 mL) were subjected to centrifugation at 5,000 rpm for 5 min in a microfuge. Cells were resuspended in 50 µL of PBS, deposited on quartz microscope slide and photographed on a UV table with excitation at 303 nm. Median fluorescence in the red channel was quantified in square areas encompassing about 60% of the droplets and excluding their edges using the histogram function of Adobe Photoshop. Fluorescence loss was quantified by subtracting the fluorescence of control samples from that of QD-loaded cells at the indicated time points.

1.12.5 Stress responses

Strains ADA110 (AB734 λϕ(*ibp::lacZ*)) and ADA510 (AB734 λϕ(*sulA::lacZ*)) have been described previously.[250, 251] ADA710 (AB734 λϕ(*katG::lacZ*)) was constructed by lysogenizing

AB734 with a bacteriophage λ derivative bearing the oxidative stress-responsive *katG::lacZ* translational fusion and isolated from BGF931 through standard protocols.[252] The three strains were made chemically competent by $CaCl_2$ treatment and incubated or not with QDs as above. After resuspension in buffer, 200 µL of culture was used to inoculate 5 mL of LB medium. Samples were either exposed to buffer (negative control), known stress response inducers (4% ethanol, 15 µg/mL nalidixic acid, or 10 µM H_2O_2) or 0.5 µg/mL or 2.5 µg/mL of BB-CT43-stabilized QDs. After a 3h incubation at 37° C, cells were lysed and β-galactosidase activities determined as described.

1.12.6 Analytical techniques

UV-visible absorption spectra were recorded on a Beckman DU640 spectrophotometer. Fluorescence and phosphorescence emission spectra were recorded using 1 mL of sample on a Hitachi F4500 fluorescence spectrophotometer with excitation at 280 nm and excitation and emission slit widths set at 2.5 nm (fluorescence) or excitation at 316 nm and excitation and emission slit width at 2.5 nm and 10 nm, respectively (phosphorescence). The wavelength region corresponding to the second order diffraction peak of the excitation light was omitted.

1.13 Results and Discussion

1.13.1 Uptake by Escherichia coli requires membrane destabilization

We previously described the aqueous, one-pot synthesis of ZnS:Mn QDs using a linear ZnS binding peptide (CT43) fused to a tandem repeat of the antibody binding domain (B) from protein A of *S. aureus*. These biomineralized QDs are ~10 nm in hydrodynamic diameter, fluoresce at 590 nm when excited in the UV range and are stable for months in solution. This stark deviation from the industry standards presented us with the opportunity to examine the stability and toxicity of these nanocrystals in biological systems. To this end, we characterized their uptake by *E. coli*,

an extensively studied gram-negative organism whose envelope consists of the following consecutive layers: (i) a 13 nm thick and negatively charged outer membrane composed of a lipopolysaccharide outer leaflet and phospholipid inner leaflet; (ii) a 1-2 nm thick peptidoglycan layer formed by polymerized sugars and amino acids; (iii) a 12 nm thick gel-like space known as the periplasm; and (iv) a 5 nm thick inner membrane consisting of a phospholipid bilayer.[253]

When *E. coli* cells harvested in mid-exponential phase were incubated with 0.5 µg/mL BB-CT43-mineralized QDs, there was no detectable nanocrystal uptake, as evidenced by the fact that washed cell pellets remained blue upon UV illumination (**Figure 3.1**). However, and as previously reported,[254] fluorescent material colocalized with sedimented cells if *E. coli* was first made chemically competent by incubation with 100 mM $CaCl_2$ at low temperature. This treatment transiently affects the integrity of the outer membrane and is routinely used for introducing naked DNA into cells, but the mechanism(s) responsible for this remain largely unknown. QD uptake by these chemically competent cells was dose-dependent as was seen in other studies. (**Figure 3.1B & C**)[144] Whether transient loss of cell envelope integrity is needed for nanoparticle uptake by microbes has been a controversial issue. Clearly, prokaryotes lack the endocytosis pathways responsible for nanoparticle uptake by eukaryotes. Furthermore, bacterial porins, which allow free diffusion of small molecules across prokaryotic membranes through 1-2 nm pores,[255] should not support penetration of even the smallest QDs. Nevertheless, Hirschey and coworkers reported that CdSe/CdS QDs stabilized by citrate, isocitrate, succinate, or malate readily penetrated unmodified E. coli when their core size was smaller than 6 nm. By contrast, Wenhua et al. found that mercaptoacetic acid-stabilized QDs with 3-4 nm CdSe/CdS cores could only enter E. coli if the outer membrane had been destabilized by chemical treatment,[254] and Nadeau and coworkers reported that the uptake of adenine-coated CdSe QDs smaller than 5 nm was strictly dependent on

photo-induced membrane damage and purine metabolism.[152] The results of **Figure 3.1**, which were obtained with biologically relevant protein shells and inorganic cores that are less susceptible to photo-oxidation than CdSe, strongly support a scenario where disruption of outer membrane integrity is a prerequisite for entry of these nanoparticles in *E. coli*.

1.13.2 Internalized QDs localize to the cytoplasm

To confirm that the nanocrystals localized to the cell interior and were not simply adsorbed to the surface of the outer membrane, competent *E. coli* were incubated with BB-CT43-mineralized QDs as above and subjected to spheroplasting (**Figure 3.2**). This procedure strips cells of their outer membrane and peptidoglycan layer, releases periplasmic contents and leads to loss of bacterial rod shape and formation of spherical cytoplasmic vesicles bounded by the inner membrane.[249] **Figure 3.2B** shows that the spheroplasts thus obtained remained fluorescent, indicating that the protein-coated nanocrystals were either associated with the inner membrane or had translocated to the cytoplasm.

Because confocal microscopy does not allow one to unambiguously distinguish between these two possibilities, we took advantage of the fact that the emission spectrum of UV-excited ZnS:Mn nanocrystals overlaps the absorption spectrum of the fluorescent protein mCherry.[256] Thus, Förster Resonance Energy Transfer (FRET) should occur between the two fluorophores if they co-localize in the same cellular compartment and are separated by less than 10 nm. To test this idea, we first recorded fluorescence emission spectra of competent cells that had incorporated QDs or had been exposed to buffer alone following excitation at 280 nm. Subtraction of the two spectra eliminated the contribution of background fluorescence and revealed a weak but clear peak centered at 590 nm and corresponding to ZnS:Mn emission (**Figure 3.3**, orange). Next, we introduced a plasmid expressing high levels of mCherry in the cytoplasm of E. coli and confirmed

that the emission spectrum of these cells exhibited the characteristic shape and 610 nm emission maximum of mCherry upon excitation at 590nm (**Figure 3.3**, inset).[256] Finally, we made samples of mCherry-producing cells competent, exposed them to QDs or buffer as detailed in the experimental section, and used these samples to collect fluorescence emission data following excitation at 280 nm. The subtracted spectrum (**Figure 3.3**, red) shows that the QD-associated peak at 590 nm peak completely disappeared to the profit of a 610 nm peak corresponding to mCherry emission. We conclude that nonradiative energy transfer occurs between the two fluorophores in intact cells. This implies that the nanocrystal donor and protein acceptor are located within a few nanometers of one another and thus in the cell cytoplasm.

How QDs (or plasmid DNA for the matter) translocate across the peptidoglycan layer, periplasm and inner membrane to reach the cytoplasm remains unclear. One possible explanation is that both DNA and nanoparticles rely on the transient and $CaCl_2$-induced opening of sites where the outer and inner membranes come into intimate contact. Such adhesion zones, known as Bayer's patches, were identified microscopically over 40 years ago,[257] but their existence has remained controversial in spite of supporting biochemical evidence.[258]

1.13.3 High doses of ZnS:Mn nanocrystals are required to induce an oxidative stress responses

We next investigated how the presence of QDs in the cytoplasm would impact cell physiology. Prokaryotes have evolved complex and redundant mechanisms to survive exposure to environmental stresses. Many of these processes rely on increasing the synthesis of protective proteins (e.g., molecular chaperones, proteases, DNA repair enzymes and reductases) through upregulation events that are often controlled at the transcriptional level. Previously, we described *E. coli* cells harboring single-copy gene fusions between the stress-inducible *ibp* or *sulA* promoters

and the *lacZ* gene (which encodes β-galactosidase).[250, 251] These strains report on the amount of stress experienced by the cell as a result of cytoplasmic protein misfolding (*ibp::lacZ* fusion) or DNA damage (*sulA::lacZ* fusion) by producing the easily assayed enzyme, β-galactosidase. Because QD cytotoxicity has repeatedly been correlated with oxidative damage,[152, 259-262] we constructed an additional isogenic strain bearing a single-copy gene fusion between the oxidative stress responsive promoter of the major *E. coli* catalase (the *OxyR*-regulated *katG* gene product)[263] and *lacZ*.

The functionality of the reporter panel was first confirmed using hydrogen peroxide, nalidixic acid and ethanol at concentrations known to cause extensive oxidative stress, DNA damage, or protein misfolding, respectively.[250, 251] These chemicals caused about a 3-fold induction of the corresponding promoters (**Figure 3.4**, positive controls). Next, the three strains were made chemically competent, exposed to QDs, and cultures were assayed for β-galactosidase activity after 3h. While there was no detectable induction of any of the stress promoters when QDs were supplied at the concentration used in all above experiments (0.5 μg/mL), addition of 2.5 μg/mL nanocrystals was as effective as the use of 10 μM H_2O_2 in inducing the *katG* promoter. Of note, however, there was no statistically significant activation of either the *ibp* or *sulA* promoter under the same conditions (**Figure 3.4**). While the dependency of toxicity on QD dose is not particularly surprising,[144] our results indicate that it takes highly concentrated solutions of nanocrystals to fully induce the bacterial oxidative stress response and that BB-CT43-stabilized QDs do not cause appreciable protein misfolding or DNA damage under the same conditions.

1.13.4 QD fluorescence is rapidly lost in growing cells

The persistence of toxicants in the environment can lead to their long-range transport and bioaccumulation at toxic doses in animal and human tissues. To gain information on the in vivo

stability of BB-CT43-stabilized QDs, we first incubated cells that had internalized nanocrystals in phosphate buffered saline (PBS) for 24 h at temperatures ranging from 4 to 42° C. **Figure 3.5** shows that there was no significant change in the fluorescence of cell pellets indicating that protein-capped nanocrystals are stable for extended periods of time in quiescent cells exposed to a physiologically relevant range of temperatures.

To determine if growth or metabolic activity would influence this outcome, QD-loaded cells were taken in LB medium and incubated at 37° C, the optimum growth temperature for *E. coli*. In contrast to quiescent cells, we observed a linear decrease in fluorescence over time and nearly complete disappearance of the signal after 3 h of cultivation (**Figure 3.6**A, closed symbols). Because cells experienced a 1 h lag phase and exponential growth only started about 2 h after transfer to LB (**Figure 3.6**A, open symbols), the nearly 50% loss of fluorescence that occurs over the first 1.5 h of cultivation cannot be attributed to QD dilution by cell division. Indeed, when the experiment was repeated in the presence of the translational inhibitor kanamycin, we observed a similar fluorescence loss over the first 1.5 h but, remarkably, no further decrease thereafter (**Figure 3.6**B). Thus, although de novo protein synthesis and/or cell growth are not implicated in the initial signal loss, they are necessary for complete elimination of QD fluorescence.

There are several possible explanations for the initial loss in fluorescence emission intensity: dissolution or extrusion of about 50% of the internalized nanocrystals or substitution of the BB-CT43 shell by host proteins that change the QD optical properties. We do not believe that chemical dissolution of the nanocrystals is a likely mechanism since it would be unlikely to abruptly stop in kanamycin-treated (**Figure 3.6**) or quiescent cultures (**Figure 3.5**). The fact that *E. coli* primarily relies on the trans-periplasmic protein TolC as an exit duct to export a wide variety of small drugs and proteins from the cytoplasm to the growth medium offered us a route to test the

extrusion hypothesis. However, there was no significant difference in the kinetics and extent of fluorescence loss in isogenic *tolC+* and *tolC* cells indicating that a TolC-dependent extrusion mechanism is not at play (**Figure 3.7**). While we cannot rule out extrusion through other systems, we favor a mechanism in which host proteins replace BB-CT43 at the ZnS:Mn surface, causing a decrease in maximum emission intensity. This explanation is consistent with our observation from previous work that BB-TxA::CT43-mineralized QDs have lower emission intensity than those fabricated with BB-CT43, and the fact that the fluorescence of kanamycin-treated cultures reaches a plateau after 1.5 h (**Figure 3.6**B), which is presumably the time needed to modify the surface of all internalized nanocrystals. Irrespective of the precise mechanism of initial fluorescence loss, the data of Fig. 6A shows that the QD signal is rapidly lost in actively growing cultures due to dilution by cell division.

1.14 Conclusions

In this study, we have shown that our protein-stabilized ZnS:Mn QDs can translocate in a dose-dependent manner to the cytoplasm of *E. coli*, but there is an absolute requirement for chemical destabilization of the cell envelope. Once inside the cell cytoplasm, these QDs did not induce the protein misfolding or SOS responses at either administered dose, but the cells did experience oxidative stress at the 2.5 μg/mL dose. The fluorescence of cell pellets containing QDs was reduced by ~50% after the reintroduction of the cells to LB media within 1.5h, but inhibition of de novo protein synthesis prevents the fluorescence from being completely lost. Such inefficient bacterial uptake coupled with the facts that internalized nanocrystals do not induce significant stress responses and do not persist in dividing cells suggest that biofabricated ZnS:Mn QDs will be unlikely to cause damage to prokaryotes in the environment.

1.15 Figures

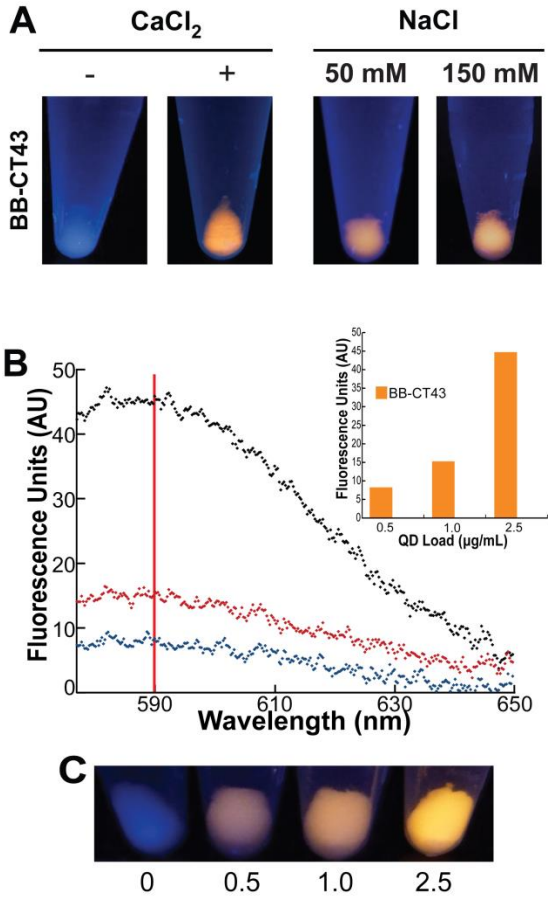

Figure 0.1 The impacts of $CaCl_2$, NaCl and dose on QD penetration in *E. coli*. (A) AB734 cells made competent by $CaCl_2$-ice treatment (+) or not (-) were incubated with BB-CT43-mineralized ZnS:Mn nanocrystals for 2h. Cells were washed twice and pellets were photographed under UV illumination. A minor increase in transformation was observed with a buffer containing 150 mM NaCl over 50 mM NaCl. (B) Quantification of dose-dependent penetration of the QDs by fluorescence sprectroscopy. The inset shows the values at the 590 nm emission peak for each of the three load quantities. (C) AB734 competent cells under UV illumination after being exposed to the indicated µg/mL loads of of BB-CT43 QDs followed by two pellet-wash cycles.

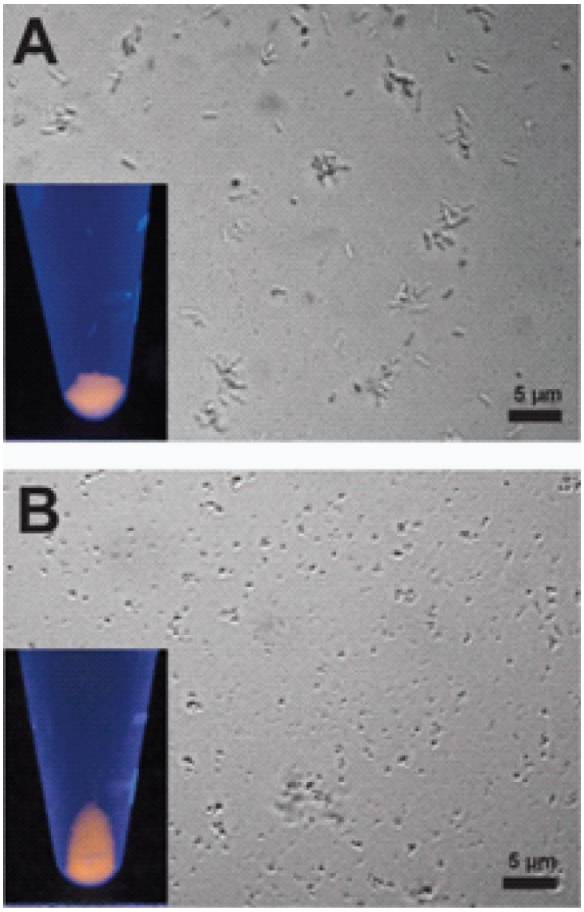

Figure 0.2 Spheroplasts retain the QD fluorescence. AB734 cells that had uptaken BB-CT43-stabilized QDs were washed and imaged on an optical microscope without further treatment (A) or following spheroplasting (B). Insets show the appearance of cells or spheroplasts following sedimentation by centrifugation and exposure to UV light.

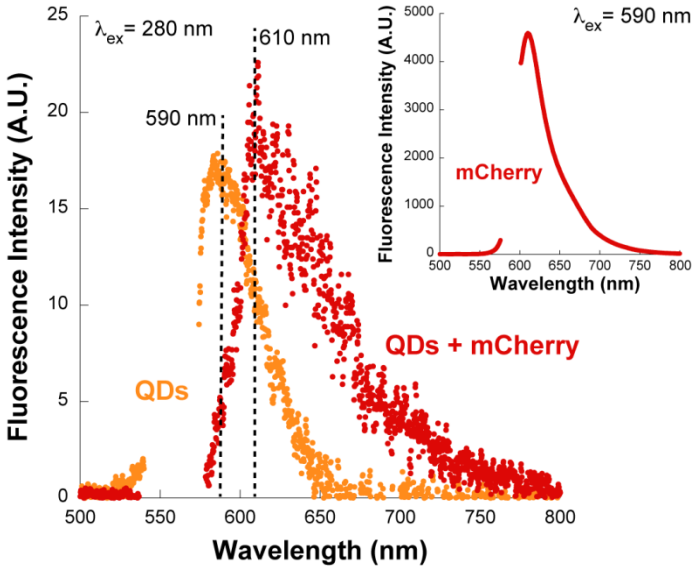

Figure 0.3 FRET confirmation of cytoplasmic QDs. The inset shows the emission spectrum of mCherry producing cells upon direct excitation at 590 nm. The orange spectrum is from QDs inside of cells upon excitation at 280 nm. The red spectrum is of cells containing both QDs and cytoplasmic mCherry with excitation at 280 nm. The existence of emission at 610 nm but not 590 nm confirms the cytoplasmic location of the QDs.

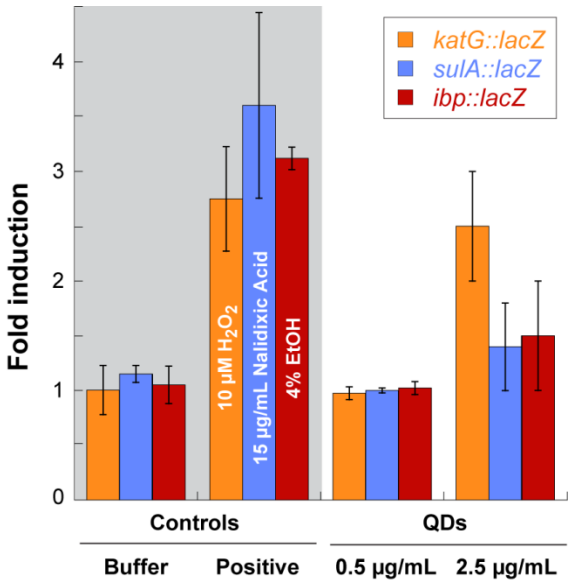

Figure 0.4 Internalized QD cause oxidative stress at high doses but do not significantly activate the SOS or unfolded protein responses. AB734 cells bearing single copy chromosomal fusions between the *lacZ* reporter gene and promoters induced by oxidative stress (*katG*), DNA damage (*sulA*), and cytoplasmic protein misfolding (*ibp*) were made competent and exposed to buffer (negative control) or the indicated chemical stressors. β-galactosidase activities were determined after 3 h at 37° C and the magnitude of promoter induction was calculated by assigning a value of unity to the mean of negative controls. The β-galactosidase activity in cultures that had internalized BB-CT43-stabilized QDs supplied at 0.5 or 2.5 µg/mL was determined in a similar fashion. Error bars correspond to independent triplicate experiments.

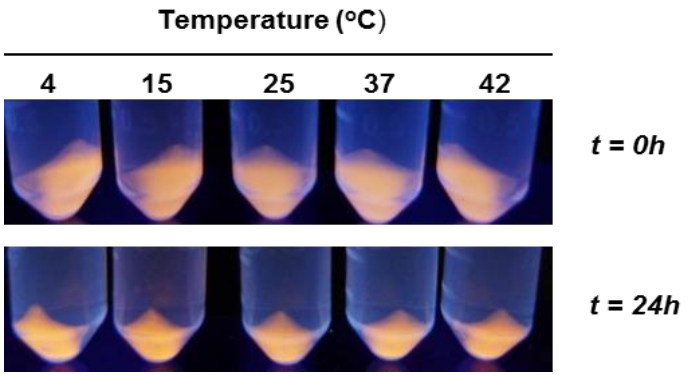

Figure 0.5 Quiescent cells retain QD fluorescence. AB734 cells that have taken up BB-CT43 stabilized QDs remain fluorescent after 24 h of incubation at temperatures varying from 4 to 42° C.

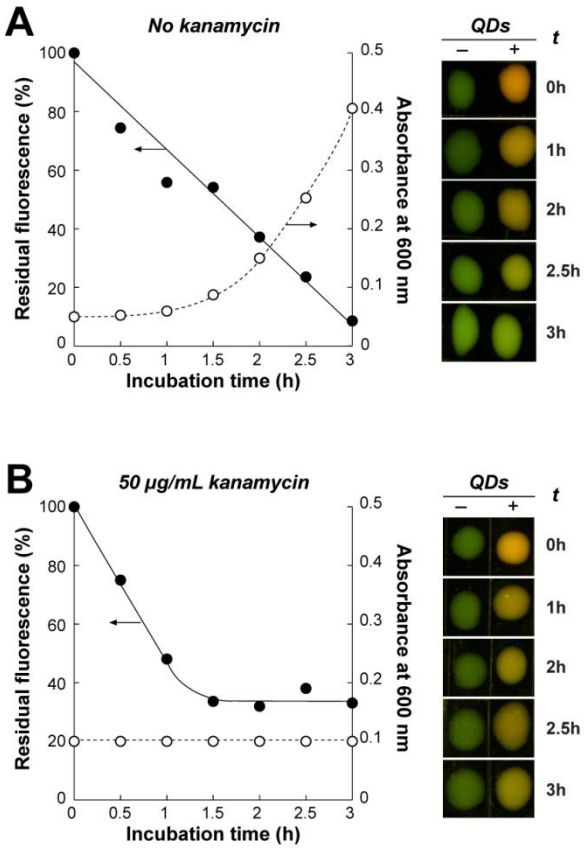

Figure 0.6 Complete elimination of internalized QD fluorescence requires active cell growth. The fluorescence (closed circles) and growth (open circles) of AB734 cells that had internalized BB-CT43-mineralized QDs was measured in the absence (A) or presence (B) of the translational inhibitor kanamycin at the indicated time points. Photographs show the fluorescence of cell samples (50 µL) from cultures that had uptaken QDs (+) or not (-) and after the indicated incubation times at 37° C in LB medium.

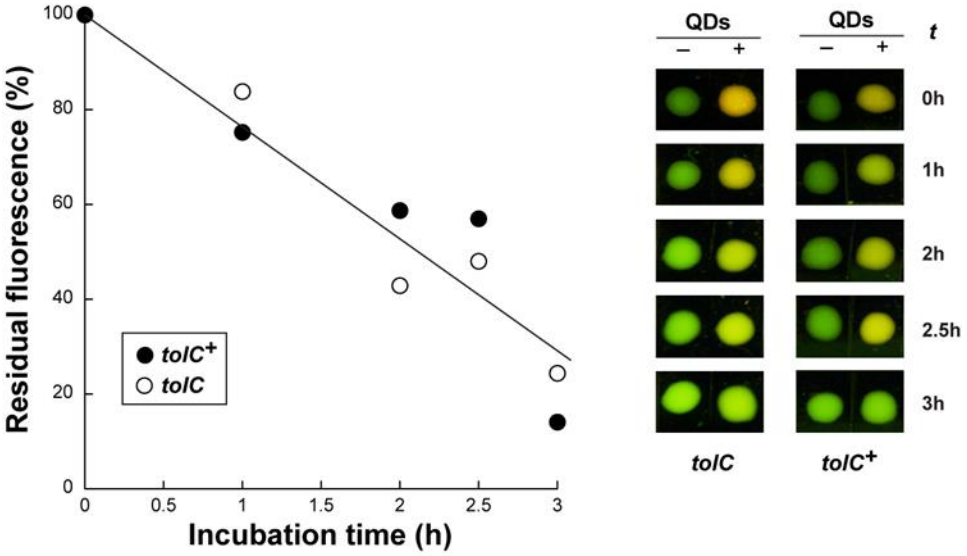

Figure 0.7 Impact of a *tolC* null mutant on fluorescence loss. Inactivation of *tolC* has no obvious impact on the loss of fluorescence in AB734 cells experiencing balanced growth in LB medium at 37° C.

Development of a protein with multiple, modular functionalities

1.16 Introduction

Combining multiple sources of fluorescence whose emission is either quenched or activated in the presence of a specific analyte is the basic premise for color shift sensors.[264] With their narrow, size-tunable emission spectra, broad excitation spectra, and large Stokes shift quantum dots (QDs) are particularly attractive for the construction of sensors that are tuned to the unique absorption or emission properties of organic fluorophores.[265-269] Such sensors often exploit Förster resonance energy transfer (FRET) between a CdSe/ZnS QD donor (λ_{em} ~ 600 nm) and a well characterized organic dye such as Cy5 as an acceptor, (λ_{ex} ~ 605 nm).[270] Fluorescent proteins have also been covalently coupled to the hydrophilic dihydrolipoic acid (DHLA) coatings of QDs[271, 272] but only recently have small capping ligands been developed that allow His-tagged fluorescent proteins to directly bind to the Zn-rich surface of QDs via metal coordination.[272, 273] The additional chemical modifications required for these methods[274] can not only cause instability of the particles, but also reduce their FRET efficiency by increasing the distance between the acceptor and donor components.[275] Therefore, the synthesis of a stable organic-inorganic fluorophore pair in a single, aqueous step would present a facile, environmentally friendly alternative to current methods of synthesis.

In this work we use a fluorescent protein, superfolder GFP (sfGFP, **Figure 4.1**), modified with a ZnS binding peptide to synthesize ZnS:Mn QDs creating an organic-inorganic fluorophore pair without the need for covalent conjugation chemistries.[276] We further modify sfGFP by adding a silica binding peptide, Car9, in a permissive loop on the protein face opposite of the N- and C-termini, which should allow the protein to bind to silica surfaces. Finally, we introduced single cysteines at two different sites on the protein to create a new chemical handle for easy chemical

conjugation of DNA aptamers that would enable this construct to be used as a sensor for small molecules.

1.17 Materials and Methods

1.17.1 DNA manipulations

Previously[277], a pUC57-Kan derivative containing a *Nde*I-*Xho*I fragment encoding a variant of sfGFP with *Avr*II and *Spe*I restriction sites at codons 172-173 (a known permissive site)[187] and a 3' extension specifying a GGGS linker followed by the Car15[278] dodecamer (RTYLPLPWMAAL) was ordered from GenScript (Piscataway, NJ). This gene was inserted via *Nde*I-*Xho*I sites into pBLN200[279] to place the sfGFP derivative under transcriptional control of the arabinose-inducible P_{BAD} promoter. Complementary primers encoding the Car9 sequence (DSARGFKKPGKR) flanked by *Avr*II and *Spe*I sites (5'-GTGGAGCCTAGGGACAGTGCTCGCGGGTTTAAAAAGCCTGGGAAGCGGACTAGTGATGGC–3') were ordered from Invitrogen (Carlsbad, CA). Primers were mixed at 10 µM concentration, boiled for 10 min and allowed to slowly cool to room temperature. Annealed primers were digested with *Avr*II and *Spe*I and inserted into the same sites on the sfGFP-Car15 to yield sfGFP::Car9-Car15, in which the native VEDG loop 9 is replaced by VEPRDSARGFKKPGKRTSDG and the protein contains the KLGGGSRTYLPLPWMAAL C-terminal sequence. Because *Avr*II and *Spe*I are isoschizomers, the *Avr*II site was mutated to *Bgl*II by Quikchange (Agilent) mutagenesis with primers 5'-CGTAGAGGATCGATATCTCGATCCCGC and 5'-GCGGGATCGAGATATCGATCCTCTACG.

In order to exchange the Car15 tag with the ZnS-binding CT43 sequence (AGDSSGVDSRSV), primers 5'-

AAAAAGCTTGGCGGCGGCTCTGCGGGTGATAGTAGTGGGGTGGACAGTCGCAGTGT TTAATAACTCGAGCACC-3' and 5'-GGTGCTCGAGTTATTAAACACTGCGACTGTCCACCCCACTACTATCACCCGCAGAGC CGCCGCCAAGCTTTTT -3' which encode CT43 preceded by a GGGS linker and flanked by *Hind*III and *Xho*I restriction sites were hybridized, digested, and ligated in to the same sites of psfGFP-Car15 and psfGFP::Car9-Car15 to yield plasmids psfGFP-CT43 and psfGFP::Car9-CT43, respectively.

The genes encoding sfGFP-CT43 and sfGFP::Car9-CT43 were placed under transcriptional control of the T7 promoter by transferring the *Nde*I-*Xho*I fragments of psfGFP-CT43 and psfGFP::Car9-CT43 into a derivative of pET24a+ whose *Bgl*II site was mutated to *BamH*I by Quikchange (Agilent) mutagenesis using primers 5'-CAACGTGGAGGGATCCGACAGTGCTC-3' and 5'-TGGCGAATTTTAAAATTCGCTTTAATG-3'.

The Arg2-Cys and Cys48-Ser/Gly51-Cys mutations were introduced into sfGFP::Car9-CT43 by Quikchange mutagenesis using 5'-GAACAGCTCTTCGCCTTTGCACATATGTATATCTCCTTCTTAAAGTTAAAC-3' or 5'-GCCAAGGTACCGGCAGTTTGCAAGTAGTGCTGATGAACTTCAGCGTCAGT-3' and their reverse complements, respectively. The resulting proteins were termed sfGFP-R2C::Car9-CT43 and sfGFP-G51C::Car9-CT43. The integrity of all constructs was verified by DNA sequencing.

1.17.2 Protein purification

BL21(DE3) cells harboring psfGFP-CT43, psfGFP::Car9-CT43, psfGFP-R2C::Car9-CT43, or psfGFP-G51C::Car9-CT43 were grown to mid-exponential phase (A600 ~ 0.4) at 37 °C in 500 mL of LB medium supplemented with 50 µg/mL kanamycin. Cultures were induced with

1 mM IPTG and recombinant protein expression was allowed to proceed for 5 h at the same temperature. Cells were centrifuged at 4,000 *g* for 10 min, resuspended in 40 mL of 20 mM Tris-HCl, pH 8.5, 5 mM EDTA, and lysed by 6 consecutive cycles of sonication (6 min on ice at 30% duty cycle) on a Branson sonifier. Insoluble material was removed by centrifugation for 15 min at 10,000*g* and clarified extracts were subjected to a 15 min heat shock at 70 °C to precipitate thermolabile proteins. Aggregated material was removed by centrifugation for 15 min at 10,000*g* and the clarified lysate was subjected to rapid silica chromatography on 5 g of Davisil grade silica (Sigma Aldrich, 15 nm pore size, 35-70 nm particle size) equilibrated in 20 mM Tris-HCl, pH 8.5. Contaminants were removed by aspiring 100 mL of buffer through the bed. Proteins sfGFP-CT43, sfGFP::Car9-CT43, sfGFP-R2C::Car9-CT43 and sfGFP-G51C::Car9-CT43 were eluted in 30 mL of buffer supplemented with 1 M Lysine[48]. The final protein concentration was ~1.5 mg/mL and the purity ~ 90% for all proteins.

1.17.3 Quantum dot synthesis

Quantum dots were synthesized as described.[276, 280] Briefly, 250 µL of 50 µM sfGFP-CT43, sfGFP::Car9-CT43, sfGFP-G51C::Car9-CT43, or sfGFP-R2C::Car9-CT43 was mixed with 185 µL of 5 mM $ZnCH_3COO$, 15 µL of 5 mM $MnCH_3COO$, 200 µL of 5 mM NH_4CH_3COO, µL of 6 mM NH_4OH, and 1.3 mL of 18 mΩ water. After 1h, 200 µL of 5 mM Na_2S was added dropwise with stirring. The resulting solutions were aged for 5 days at 37 °C and filtered through 0.2 µm filters before storage at 4 °C. Aliquots were subjected to centrifugation at 15,000 *g* for 10 min before use.

1.17.4 Silica binding

Davisil silica (50 mg) was transferred to 1.5 mL centrifuge tubes, washed twice with 1 mL of 20 mM Tris-HCl, pH 7.5, and resuspended in 300 µL of the same buffer. The slurry was

degassed, before addition of 200 µL of either sfGFP-CT43@ZnS:Mn or sfGFP::Car9-CT43@ZnS:Mn QDs, and samples were mixed by pipetting with a 200 µL tip and agitated for 10 min at room temperature on a rotary shaker. Samples were washed twice with 1 mL of 20 mM Tris-HCl, pH 7.5 and the settled slurry was photographed on a Benchtop 3UV transilluminator with excitation at 305 or 365 nm.

1.17.5 Effect of chloramphenicol on ZnS:Mn nanocrystal emission

A series of chloramphenicol solutions was prepared in 20 mM Tris-HCl, pH 7.5 so that addition of 10 µL of stock to 490 µL of QD would yield the indicated final concentrations. The resulting solutions were photographed under UV illumination. Relative fluorescence values were determined by comparison of the emission at 510 and 590 nm in a fluorescence spectrophotometer against a control sample that received only buffer additive.

1.17.6 Aptamer conjugation

Aptamer ACTTCAGTGAGTTGTCCCACGGTCGGCGAGTCGGTGGTAG which recognizes chloramphenicol with a K_d of 1 µM[281] was synthesized with a 5'-amine modification by Invitrogen. For BCN:N_3 (bicyclononyne:azide) conjugation, the aptamer (100 µM) in 10% dimethylformamide (DMF) was mixed with a 10-fold molar excess of NHS-BCN (synthesized as described previously[282]) in DMF. In parallel, the reactive Tris buffer of sfGFP::Car9-CT43 QDs was exchanged to phosphate buffered saline (PBS; 150 mM NaCl, 10 mM Na_2HPO_4, 2 mM KH_2PO_4) using 4-kDa cutoff centrifugal filters (Amicon Ultra-4; Millipore). NHS-N_3 (synthesized as described previously[282]) dissolved in PBS (5 mM) was added to 1 mL of QDs, to provide an ~10-fold molar excess of reactant to protein. Both mixtures were incubated overnight at room temperature and excess reactant was removed with centrifugal filters. A 10-fold molar excess of aptamer-BCN conjugate was mixed with the QD-N_3 conjugate and the reaction was allowed to

proceed overnight at room temperature. Centrifugal filtration was used to remove any unreacted aptamer.

1.17.7Analytical techniques

UV-visible absorption spectra were recorded on a Beckman DU640 spectrophotometer. Fluorescence and phosphorescence emission spectra were recorded using 1 mL of sample on a Hitachi F4500 fluorescence spectrophotometer with excitation and emission slit widths set at 2.5 nm (fluorescence). The wavelength region corresponding to the second order diffraction peak of the excitation light was omitted. Hydrodynamic diameters and zeta potentials were measured on 1 mL samples using a Malvern Zetasizer Nano-ZS dynamic light scattering instrument equipped with a 633 nm laser filter. Data were fit with a Gaussian distribution to determine standard deviations.

1.18 Results and Discussion

1.18.1 Synthesis of ZnS:Mn nanocrystals with sfGFP-CT43

In an effort to combine organic and inorganic fluorophores without relying on colloidal chemistry to synthesize the QD component or conjugation chemistry to couple a fluorescent protein to a luminescent nanocrystal, we set out to modify sfGFP to endow it with the ability to synthesize its own inorganic fluorophore. To this end, we fused the CT43 extension to the C-terminus of sfGFP with the expectation that the resulting protein would cap the growth of ZnS:Mn nanocrystals and lead to the production of luminescent QDs as we previously reported with other proteins.[10, 280] Purified sfGFP-CT43 along with the BB-CT43 control (*Chapter 2*) were used at a concentration of 5 μM to mineralize ZnS:Mn luminescent nanocrystals using previously described conditions.[280] DLS measurements revealed that the hydrodynamic diameter of sfGFP-

CT43@ZnS:Mn particles (14.5 ± 1.5 nm) was about 50% larger than that of the BB-CT43@ZnS:Mn control (**Figure 4.2**). This result is consistent with the fact that sfGFP is larger than BB-CT43 (30-kDa vs. 15-kDa) and with our previous observation that BB-TrxA-CT43 (a 27-kDa protein) yields ZnS:Mn nanocrystals with a mean hydrodynamic diameter of 15 nm.[280] The UV-Visible spectra of the two colloidal preparations were comparable except for the contribution of sfGFP absorption at higher wavelengths (**Figure 4.2**). However, when excited at 280 nm, the sfGFP-CT43@ZnS:Mn colloidal solution exhibited two distinct peaks corresponding to the expected emission of sfGFP (510 nm) and Mn-doped ZnS (590 nm). We conclude that the CT43 sequence endows sfGFP with the ability to stabilize ZnS:Mn nanocrystals of expected size and optical properties and that formation of the hybrid structure does not interfere with the protein fluorescent properties.

1.18.2 Construction of an sfGFP variant that supports ZnS:Mn nanocrystals fabrication and their immobilization onto silica beads

We previously reported that Car9, a dodecapeptide of amino acid sequence DSARGFKKPGKR that recognizes the edges of carbon nanostructures[278] also confers proteins to which it is fused the ability to bind silica.[48] Car9 is functional as a linear extension (e.g., when appended to the C-termini of proteins such as MBP, GFP, and mCherry) and when displayed as a disulfide-constrained loop within the active site of the *E. coli* TrxA.[48] In order to create an sfGFP variant that would support the synthesis of luminescent nanocrystals and further mediate their association with silica substrates, we used standard molecular biology approaches to insert Car9 within loop 9 of sfGFP-CT43 (**Figure 4.1**). This loop maps between residues 172 and 173 of sfGFP and is one of 2 sites shown by Abedi et al. to tolerate the insertion of extraneous sequences up to 20 amino acids in length.[187] We chose this location because it lies on the opposite side of the β-

barrel relative to the C-terminal CT43 extension. Thus, Car9 should remain accessible for silica binding following capping of ZnS:Mn nanocrystals by CT43 segments.

The resulting protein, sfGFP::Car9-CT43, was expressed at high levels in *E. coli* where it accumulated in a primarily soluble form, confirming that loop 9 is permissive. In addition, the Car9 insert was functional since we were able to purify the tripartite fusion to near homogeneity in a single chromatography step on silica beads[48] (**Figure 4.3**). Finally, and as expected, purified sfGFP::Car9-CT43 supported the production of ZnS:Mn nanocrystals whose spectral characteristics and hydrodynamic diameters (15 ± 1 nm) were comparable to those obtained with sfGFP-CT43 (14.5 ± 1.5 nm, **Figure 4.4**).

To identify conditions that would maximize the signal from each fluorophore, we conducted excitation scans while monitoring emission intensities at 510 nm (λ^{em}_{max} for sfGFP) and 590 nm (λ^{em}_{max} for ZnS:Mn nanocrystals). **Figure 4.5** shows that excitation at 305 nm gave the highest ZnS:Mn to sfGFP signal while excitation at 365 nm yielded a signal of comparable intensity that had no contribution from the inorganic fluorophore. The apparent ZnS:Mn emission occurring at 485 nm excitation is an artifact from a tail of the broad sfGFP emission peak when excited at 485 nm. For comparison, excitation of the nanocrystals at the primary absorption peak of sfGFP (485 nm) yields a fluorescent signal that is 10-fold larger than that obtained when exciting at 365 nm, and even excitation at 365 nm creates an observable tail emission at 590 nm (**Figure 4.6**, middle panel). The full emission spectra of sfGFP-CT43@ZnS:Mn nanocrysals at these two excitation wavelengths, along with the appearance of the pure protein and colloidal solutions under ambient light and upon illumination at 305 nm and 365 nm is shown in **Figure 4.6**. Contributions from GFP and ZnS:Mn emissions give the solution a goldenrod color when excitation is conducted at 365 nm.

To demonstrate that sfGFP::Car9-CT43@ZnS:Mn nanoparticles could be enriched on silica substrates as a result of the presence of the Car9 insert, an excess of colloids was incubated with 35-70 μm silica particles for 5 min and the gel was washed twice. Illumination at 305 and 365 nm revealed co-localization of the expected goldenrod and green colors with the silica phase. By contrast, ZnS:Mn nanocrystals fabricated with sfGFP-CT43 were quantitatively removed by washing (**Figure 4.7**). Thus, sfGFP::Car9-CT43 retains the fluorescent properties of green fluorescent protein and supports both the biosynthesis of ZnS:Mn nanocrystals and their immobilization onto silica substrates, which should prove useful for sensor construction. From a protein engineering standpoint, our results indicate that the Car9 solid binding peptide is available for silica binding when inserted within loop 9 of sfGFP-CT43 and that bringing the two materials in apposition does not disrupt the interaction between the C-terminal CT43 extension and the surface of the QDs. To complete the design of an inexpensive optical sensor, we next turned our attention to the detection modality and the analyte recognition moiety.

1.18.3 Chloramphenicol detection

Like many marine toxins and small molecule pollutants[283, 284], chloramphenicol absorbs strongly in the 300 nm region of the spectrum (**Figure 4.8**) but is nearly transparent at wavelengths greater than 350 nm. Therefore, its addition should quench the 305 nm excitation of biofabricated ZnS:Mn nanocrystals while having little effect on the 365 nm excitation of the capping sfGFP. This hypothesis was confirmed by supplying an sfGFP::Car9-CT43@ZnS:Mn colloidal suspension with increasing concentrations of chloramphenicol (**Figure 4.9**A). Quantification of emission intensities at 590 nm and 510 nm further revealed that both ZnS:Mn and sfGFP peaks decreased linearly with the chloramphenicol concentration in the 0-60 μg/mL range when the solution was excited at 305 nm. By contrast, there was no change in the intensity of the sfGFP

emission peak in the presence of chloramphenicol when excitation was conducted at 365 nm (**Figure 4.9**B, open circles). This detection modality could form the basis of a ratiometric sensor if the UV-absorbing analyte could be selectively enriched in the vicinity of the nanocrystals.

1.18.4 Conjugating a chloramphenicol-specific aptamer to biofabricated nanocrystals

Antibodies and their fragments have been extensively used in biosensor construction because of their exquisite ability to detect a broad range of analytes with high affinity and selectivity. However, these molecules are generally bulky with respect to the size of QDs and they are often quite expensive to produce. An alternative detection moiety are aptamers, a class of folded DNA/RNA molecules that can be selected for binding to protein and small molecule targets by SELEX (Systematic Evolution of Ligands by Exponential enrichment)[285, 286]. One such aptamer, called chloramphenicol aptamer 7 (and hereby denoted as CA7), was identified by Mehta et al. for its ability to bind chloramphenicol with an equilibrium dissociation constant of 700 nM.

One method to conjugate small molecules such as DNA aptamers to proteins is to make use of NHS (N-hydroxysuccinimide) "click" chemistry. In this reaction scheme, the NHS group is utilized as a leaving group to covalently bond a variable side chain to a protein's primary amine. Here, we chose bicyclononine (BCN) and azide groups as variable side chains because of their irreversible bonding and availability (**Figure 4.10**). To couple CA7 to sfGFP::Car9-CT43@ZnS:Mn particles, we first reacted NHS-BCN with a synthetic CA7 containing a primary amine at its 5' end and separately conjugated NHS-N_3 to the solvent-accessible primary amines of sfGFP::Car9-CT43 capping ZnS:Mn nanocrystals. With this approach, the use of dimethyl fluoride (DMF) which is necessary to solubilize NHS-BCN but could affect protein/nanocrystal integrity is restricted to the DNA conjugation step, and the lysine residues present in the Car9

extension of sfGFP::Car9-CT43 should be unavailable for NHS-N_3 binding because they contact the nanocrystal surface.

As expected, biofabricated QDs were highly sensitive to the conjugation conditions, and many of the conditions tested caused the nanocrystals to precipitate. However, when a sfGFP:CA7 molar ratio of 10,000: 1 was used in the final conjugation step, colloidal stability and silica binding ability were retained and there was little difference between the emission spectra of aptamer-conjugated and unconjugated sfGFP::Car9-CT43@ZnS:Mn nanocrystals (**Figure 4.11**, **A**). However, addition of as little as 2 µg/mL chloramphenicol caused a readily detectable change in the emission intensity of aptamer-conjugated nanoparticles compared to their aptamer-free counterpart following excitation at 305 nm. On the other hand, the emission of both colloidal preparations was similar and unaffected by the presence of chloramphenicol when solutions were excited at 365 nm, providing a built-in control for the integrity of the sensor (**Figure 4.11**). This inexpensive approach should be useful for the qualitative detection of low chloramphenicol concentrations in field samples and could be extended to that of other analytes by making use of different aptamers.

1.18.5 Cysteine mutants of sfGFP for aptamer conjugation

The aptamer coupling method described in section 4.3.4 relies on the non-specific conjugation of NHS-N_3 to the primary amines of sfGFP::Car9-CT43. To enable a more site-specific conjugation process, we introduced cysteine substitutions at two locations of sfGFP::Car9-CT43 with the intent of using the available sulfhydryl groups and a heterobifunctional linker (e.g., succinimidyl 4-(N-maleimidomethyl)cyclohexane-1-carboxylate; SMCC) to couple aptamers to protein-coated nanocrystals. The sfGFP-R2C::Car9-CT43 and sfGFP-G51C::Car9-CT43 variants

were built by site-directed mutagenesis and expressed and purified on silica beads in the same manner as sfGFP::Car9-CT43 (**Figure 4.12**).

However, there are limitations for both constructs. The R2C mutation is located at the N-terminus of sfGFP which projects from the same face of the β-barrel as the CT43 extension. Conjugation of an aptamer to Cys-2 may thus interfere with nanocrystal mineralization or the sulfhydryl may be unaccessible for SMCC binding because Cys-2 faces the ZnS surface in particles that have already been mineralized (a likely scenario since Cys residues are known to coordinate Zn). Similarly, the G51C substitution is in loop 3 of sfGFP which lies on the same face of the β-barrel as the Car9 insertion. Thus, conjugation of an aptamer at this location could interfere with the ability of the nanocrystals to bind to silica.

While there remains a need to develop a protocol for conjugating the CA7 or other aptamers to the G51C and R2C mutants, we synthesized ZnS:Mn QDs to determine if the newly introduced cysteines would impact the functionality of the CT43 extension. The emission spectra of ZnS:Mn nanocrystals fabricated with these proteins are very similar to those obtained with the sfGFP::Car9-CT43 control protein except for a small decrease in the intensity of the GFP emission peak (**Figure 4.13**). The mean hydrodynamic diameters of the particles (21 ± 1 nm) were however 40% larger than those of the control (**Figure 4.13**) While the reason for this increase in hydrodynamic diameter remain unclear (and might be related to the formation of intermolecular disulfide bonds), these results establish that the G51C and R2C mutants of sfGFP::Car9-CT43 remain capable of driving the synthesis of luminescent ZnS:Mn nanocrystals.

1.19 Conclusions

Here, we created sfGFP::Car9-CT43, a protein that: (i) mediates the synthesis of ZnS:Mn QDs; (ii) functions as a heterobifunctional linker suitable for coupling luminescent nanocrystals to silica surfaces; and (iii) retains the fluorescent properties of sfGFP. ZnS:Mn QDs biofabricated with sfGFP::Car9-CT43 can be concentrated on silica beads and further derivatized with a chloramphenicol-binding aptamer to provide a color-shifting sensor for the antibiotic. The introduction of free cysteines in sfGFP::Car9-CT43 may prove useful for the site-specific conjugation of other aptamers.

1.20 Figures

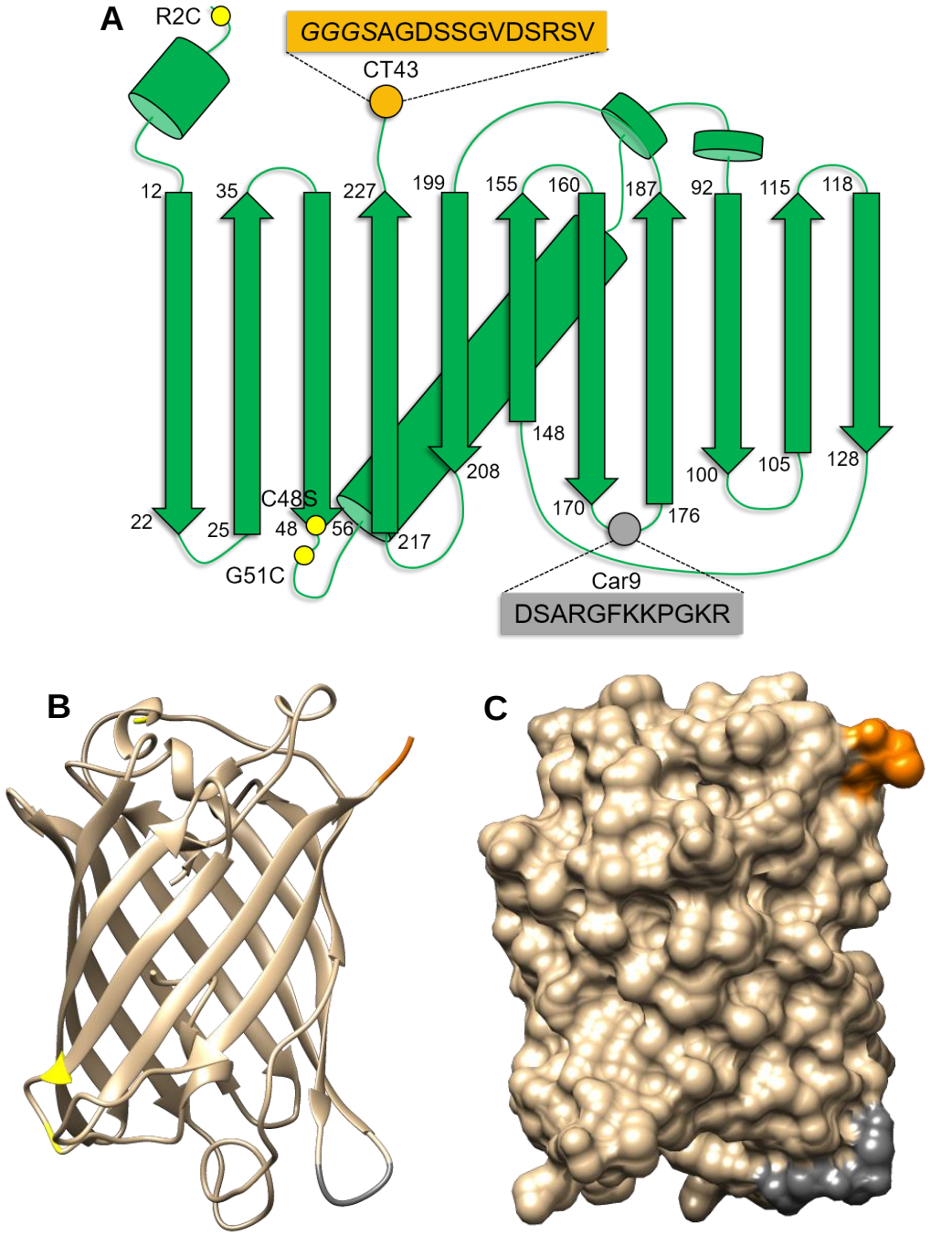

Figure 0.1 sfGFP mutants used in this study. A) Cartoon structure of sfGFP showing the location and amino acid compositions of the Car9 and CT43 extensions as well as the locations of cysteine mutations (yellow circles). B) Ribbon structure of sfGFP. The C-terminus is colored orange and permissive loop 9 highlighted in yellow. C) Molecular surface corresponding to the ribbon structure of panel B. The cysteine mutations are surface exposed but lie on the opposite face of the protein.

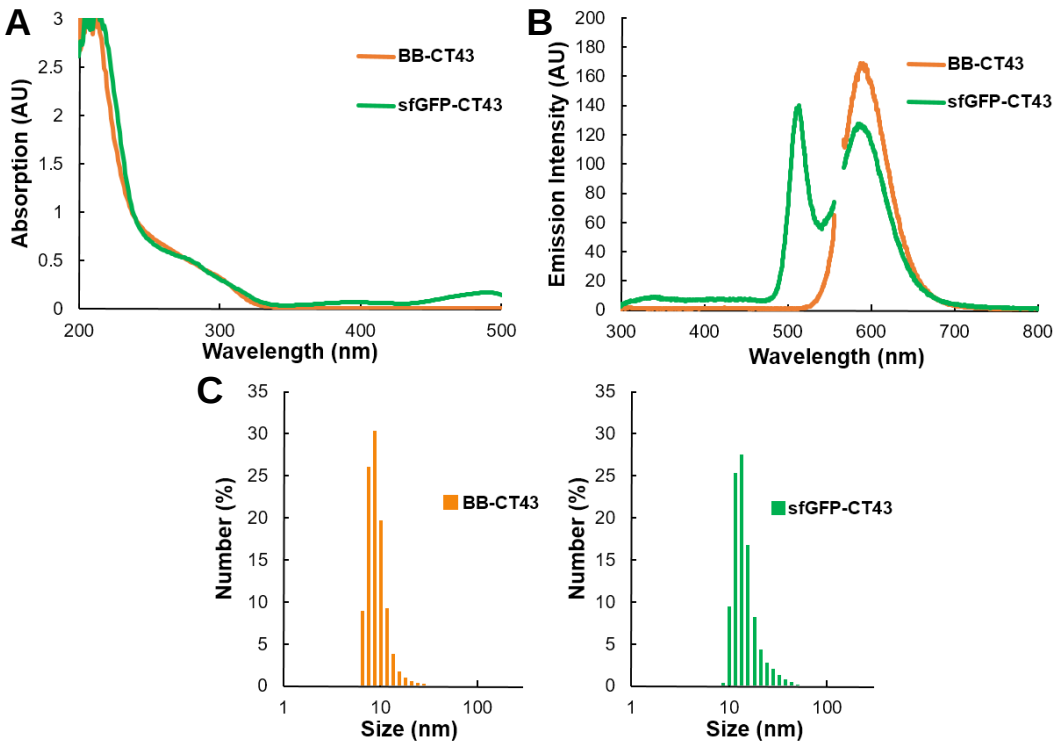

Figure 0.2 A) ZnS:Mn nanocrystals fabricated with sfGFP-CT43 (green) or BB-CT43 (orange) exhibit similar UV/visible absorption profiles. B) Emission spectra reveal that sfGFP-CT43@ZnS:Mn particles combine contributions from GFP (510 nm) and ZnS:Mn (590 nm) signals. By contrast, the BB-CT43@ZnS:Mn colloid contains a single emission peak corresponding to the inorganic fluorophore. C) DLS characterization of the particles. Mean hydrodynamic are 14.5 ± 1.5 nm for sfGFP-CT43@ZnS:Mn and 10 ± 2 nm for BB-CT43@ZnS:Mn nanocrystals.

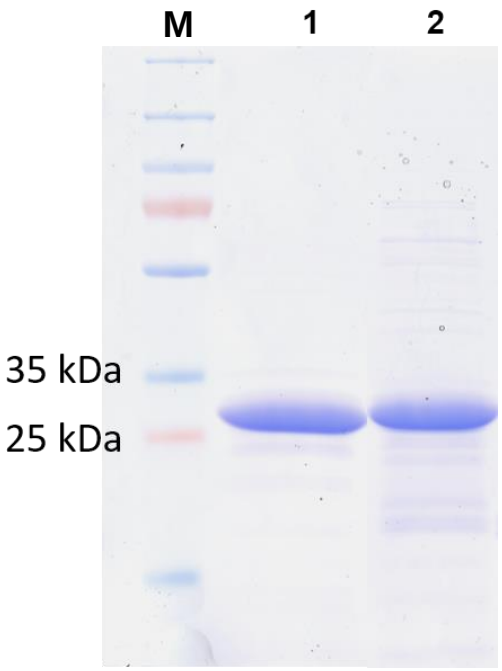

Figure 0.3 SDS-PAGE analysis of sfGFP-CT43 (lane 1) and sfGFP::Car9-CT43 (lane 2) following purification on silica gels. The protein purity is ~ 90% or higher. Lane M contains molecular mass markers. From top: 250, 130, 100, 70, 55, 35, 25, 15 kDa

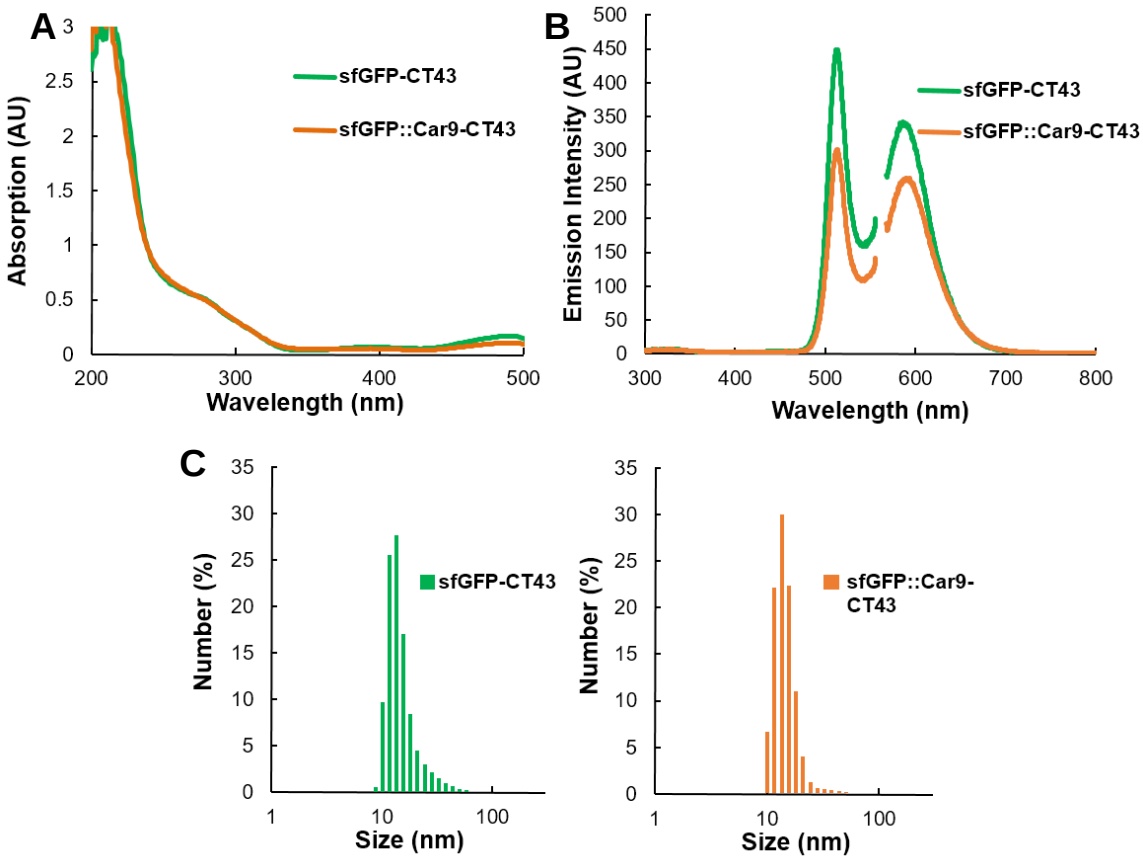

Figure 0.4 Absorption (A) and emission (B) spectra of ZnS:Mn nanocrystals fabricated in the presence of 5 µM sfGFP-CT43 or sfGFP::Car9-CT43 have very similar characteristics. The particles produced also have a comparable size distribution as judged by DLS measurements (C). Mean hydrodynamic diameters are 15 ± 1 nm for sfGFP::Car9-CT43@ZnS:Mn and 14.5 ± 1.5 nm for sfGFP-CT43@ZnS.

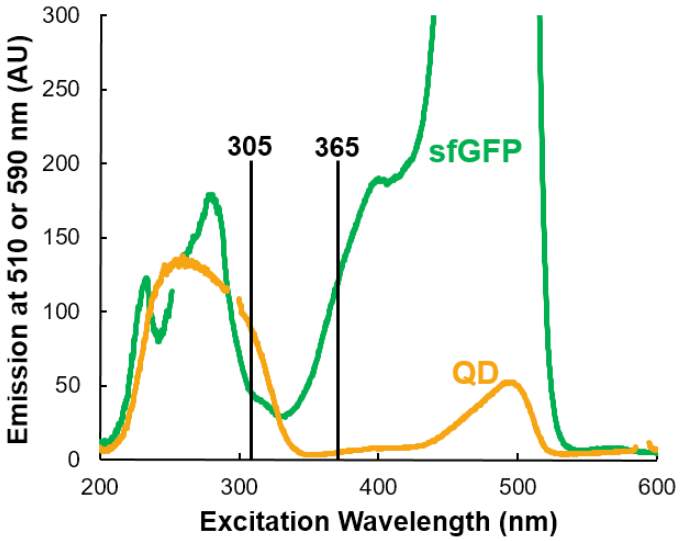

Figure 0.5 Excitation scans of sfGFP-CT43@ZnS nanocrystals. Emission intensities at 510 nm (sfGFP component; green) and 590 nm (ZnS:Mn component; orange) are shown as a function of the excitation wavelength.. The largest QD:sfGFP emission ratio occurs at an excitation wavelength of 305 nm while excitation at 365 nm results in sfGFP emission alone.

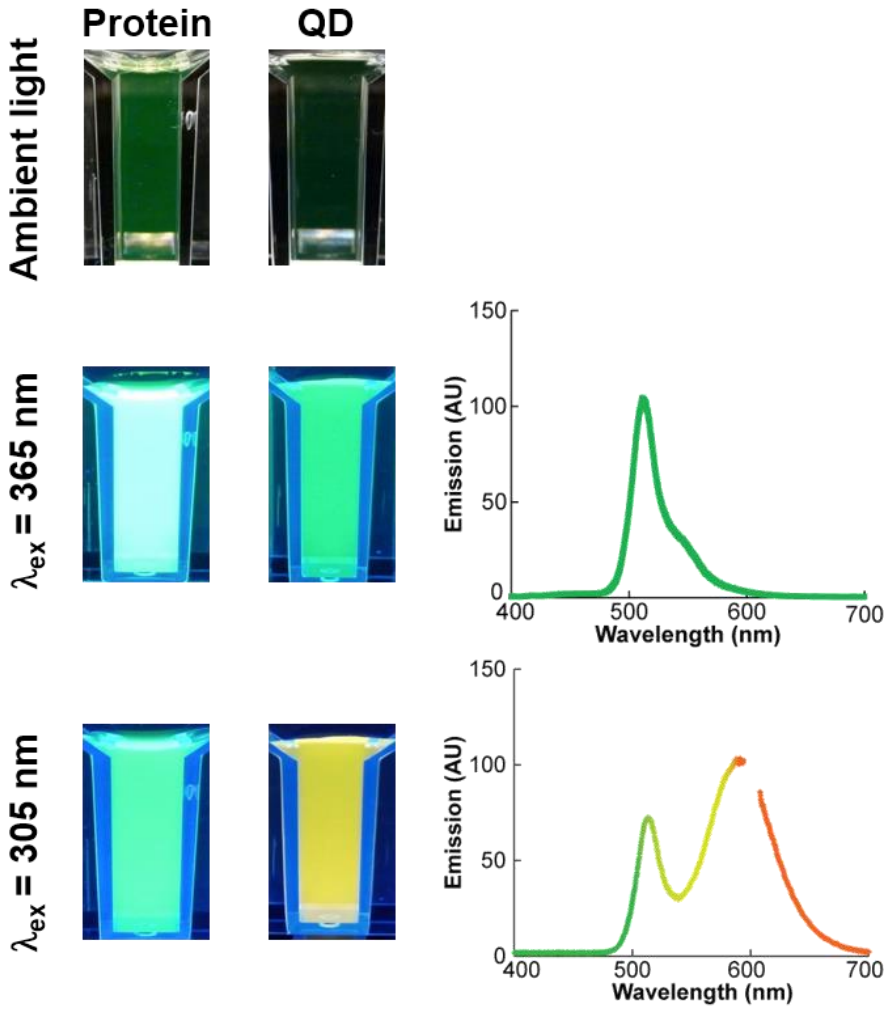

Figure 0.6 Appearance of purified sfGFP::Car9-CT43 and sfGFP::Car9-CT43 @ZnS:Mn nanocrystals under ambient light and upon illumination at 365 nm or 305 nm (left-hand side images). The corresponding emission spectra are shown on the right.

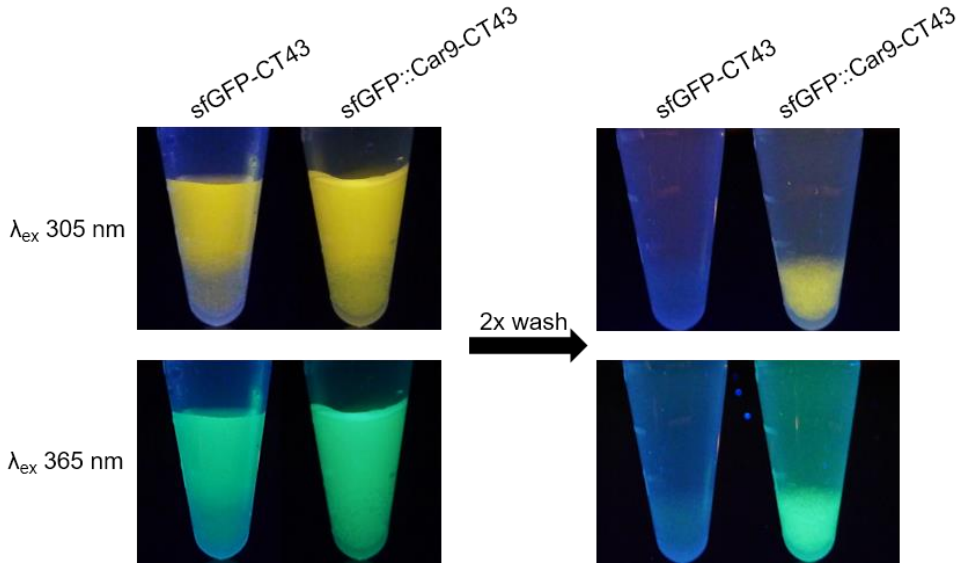

Figure 0.7 Car9 mediates the binding of sfGFP::Car9-CT43@ZnS:Mn nanocrystals to silica microparticles. ZnS:Mn QDs synthesized in the presence of sfGFP-CT43 or sfGFP::Car9-CT43 were mixed with silica beads (left panels) and subjected to two wash cycles (right panels). The appearance of the solutions is shown under illumination at 305 nm (top panels) or 365 nm (bottom panels).

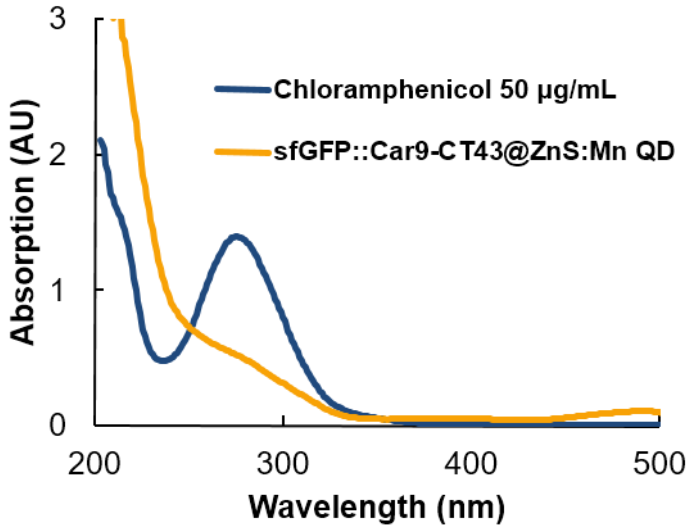

Figure 0.8 The UV/visible absorption spectra of chloramphenicol and sfGFP::Car-CT43@ZnS:Mn nanocrystals overlap. Chloramphenicol will interfere with QD emission when excitation is conducted at 305 nm, but should have no impact on sfGFP emission upon excitation at 365 nm.

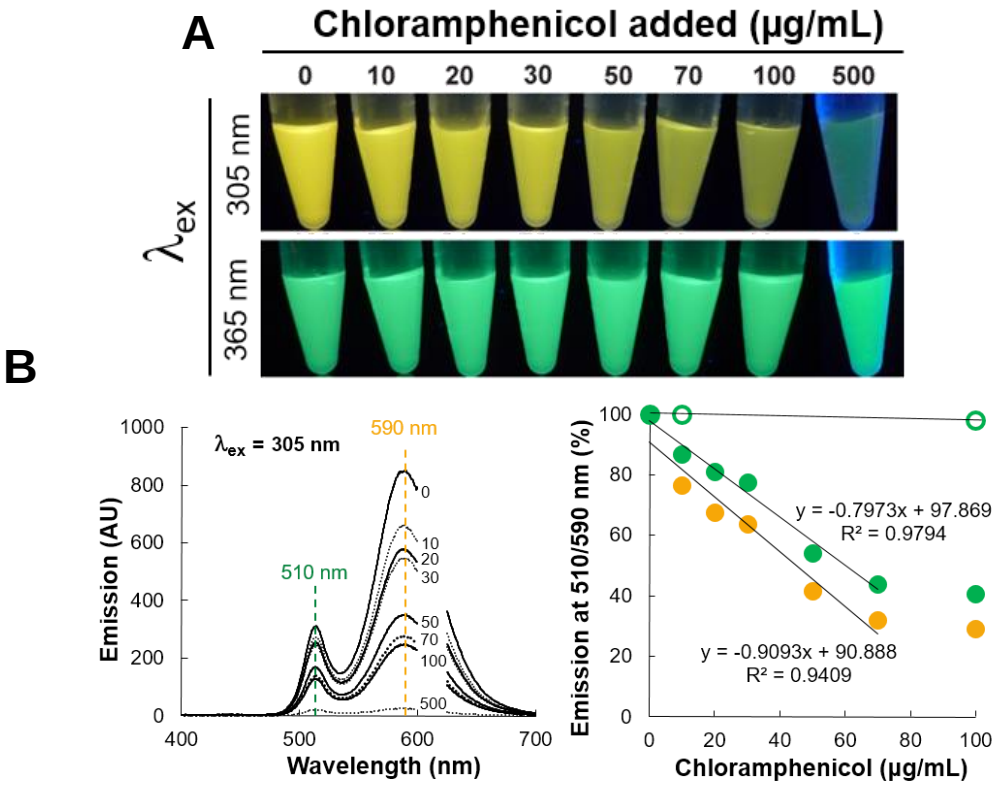

Figure 0.9 A) The emission intensity of sfGFP::Car9-CT43 capped QDs excited at 305 nm decreases in the presence of increasing chloramphenicol concentrations due to competitive absorption. However, sfGFP emission is unaffected when the solution is excited at 365 nm, which is outside the absorption spectrum of chloramphenicol. B) The left-hand panel shows the quenching effect increasing chloramphenicol concentrations have on both the QD and sfGFP signals when excitation is at 305 nm. The right-hand side panel illustrates that the quenching effect is linear in the 0-60 µg/mL range with excitation at 305 nm (closed circles). There is little to no decrease in the sfGFP signal with excitation at 365 nm (open circles).

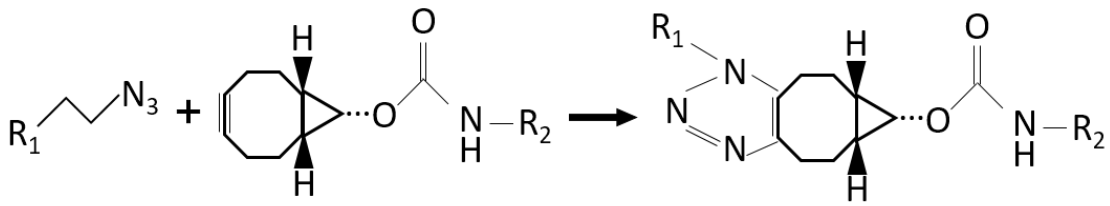

Figure 0.10 The generalized reaction scheme of azide and BCN after their conjugations to primary amine targets. In this case, R_1 is sfGFP::Car9-CT43 and azide labeling presumably occurs at all primary amines that remain solvent-accessible when the protein is tethered to ZnS:Mn nanocrystals., R_2 represents the CA7 aptamer.

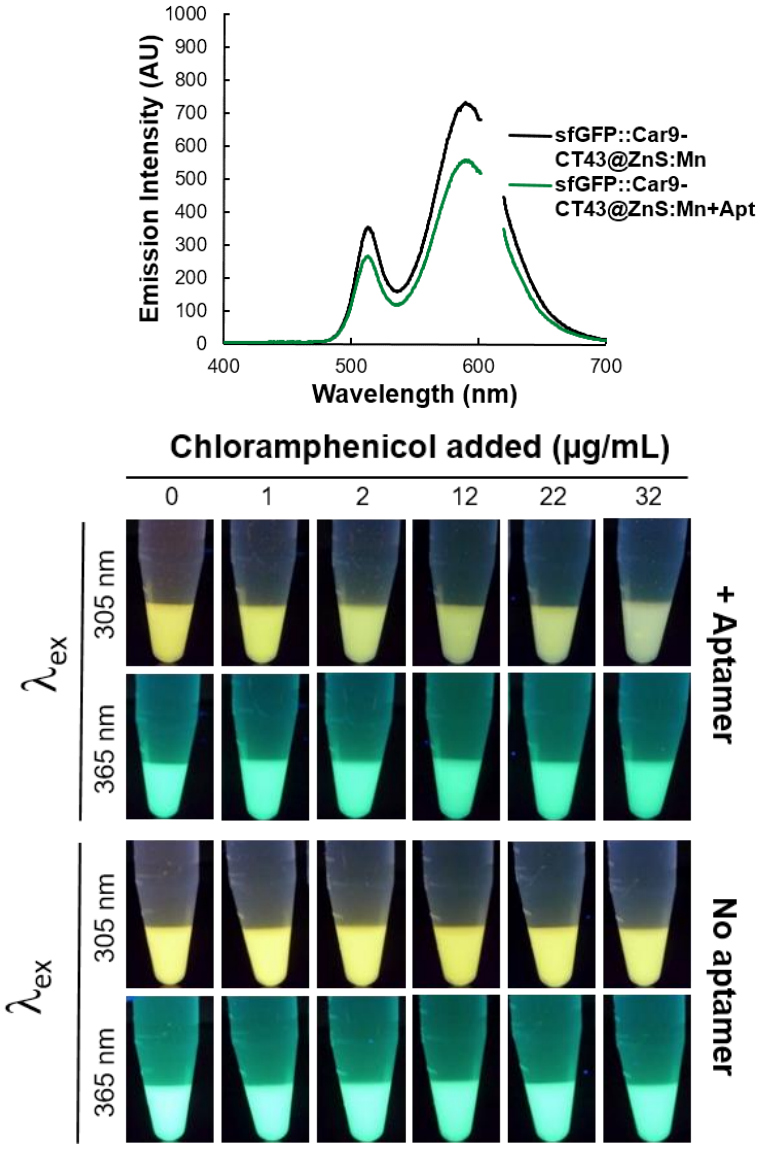

Figure 0.11 A) Emission spectra show that the conjugation of CA7 to sfGFP::Car9-CT43 QDs does not greatly impact their fluorescence upon excitation at 305 nm. B) QDs mineralized with sfGFP::Car9-CT43 were derivatized (+ Aptamer) or not with CA7, and 100 µL of colloidal solution was mixed with 50 mg of silica particles that were washed as in **Figure 0.7**. The particles were exposed to stepwise increases in chloramphenicol concentration and photographed under UV illumination at 305 nm and 365 nm.

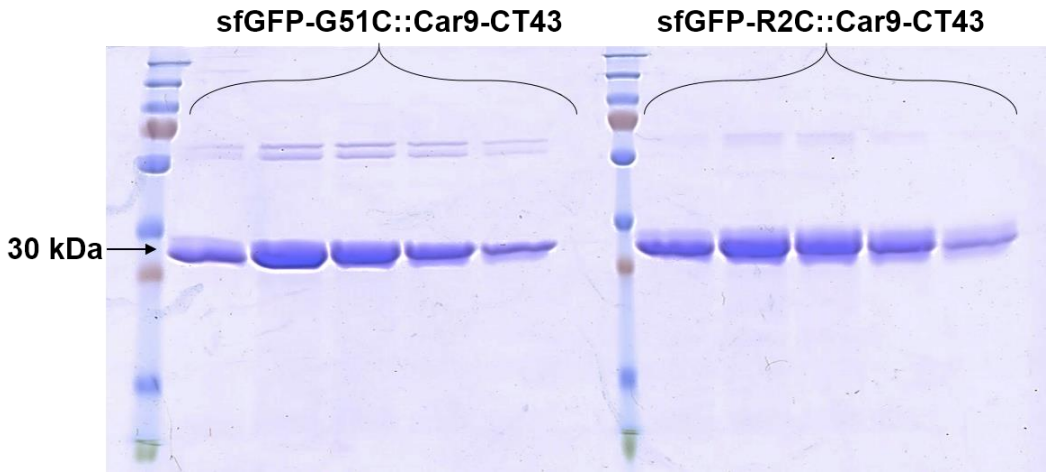

Figure 0.12 The G51C and R2C mutants of sfGFP::Car9-CT43 were purified by rapid silica chromatography. Successive fractions eluted with 1M lysine were fractionated by SDS-PAGE. Both samples contain an unidentified contaminant at ~60 kDa.

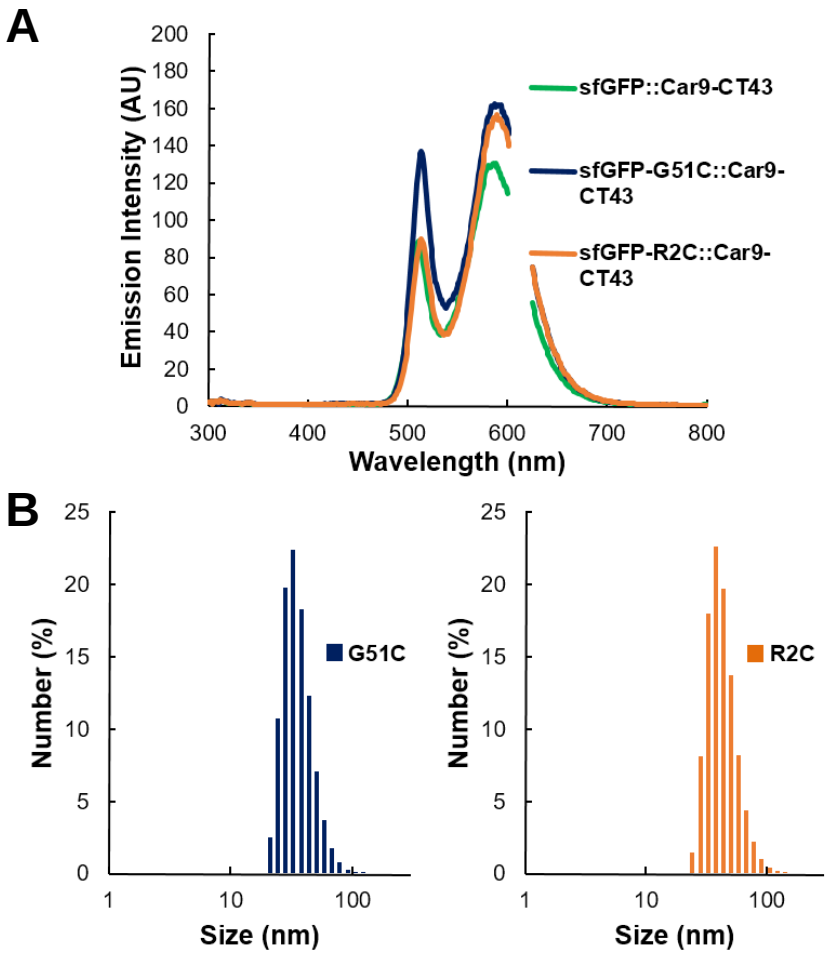

Figure 0.13 A) The G51C and R2C of sfGFP::Car9-CT43 mutants support the synthesis of luminescent ZnS:Mn nanocrystals whose emission properties following excitation at 305 nm are similar to those of the sfGFP::Car9-CT43@ZnS:Mn control. B) Particles produced with the R2C and G51C variants are slightly larger D_h (21 ± 1 nm) than those formed by the sfGFP::Car9-CT43 control (15 ± 1 nm).

Carbon nanotube dispersion

1.21 Introduction

Carbon nanotubes are a recently discovered material with highly favorable properties for use in the electronics industry. They have remarkably high conductivity[199], heat transfer[199], and tensile strength, but are hydrophobic and thus insoluble in aqueous solutions.[200, 201] Many methods that have been developed to improve the water solubility of CNTs require covalent modification of the CNT surface and thus disrupt the carbon lattice responsible for the CNT's desirable properties.[200] In this work we engineer a protein to maintain CNTs solubility in water through selective end-labeling, while also enabling their tracking by fluorescence and laying the groundwork for their controllable patterning on a surface.

1.22 Materials and Methods

1.22.1 sfGFP-Car9 construction and purification

sfGFP-Car9 was constructed previously in the lab and is amenable to rapid purification on a silica resin as previously described.[48]

1.22.2 Carbon nanotube dispersion

Single-walled carbon nanotubes purchased from NanoIntegris are dispersed in a proprietary detergent. The detergent was exchanged to sodium cholate and proteins by first diluting the CNTs 1:200 in 2% (wt/vol) sodium cholate in ddH2O, bath sonicating the resulting solution (1 mL) for 1 hour, and centrifuging it at 14,000 *g* for 30 minutes to sediment any aggregate. Next, 200 µL of 10 µM sfGFP-Car9 in 20 mM Tris-HCl, pH 7.5 (Buffer A) was mixed with 800 µL of the cholate diluted CNTs, and this solution was dialyzed against Buffer A with 3 buffer exchanges over a period of 48 hours.[287]

1.22.3 Carbon nanotube imaging

Following dialysis, the solution (500 µL) was mixed with 50 mg of silica beads (Davisil grade) that had been washed with Buffer A in order to remove free sfGFP-Car9 from solution. After 5 min incubation with gentle mixing with a pipette, 10 µL of supernatant was spotted on borosilicate microscope slides that had been previously washed with ethanol and UV-ozone cleaned for 20 min. The protein-dispersed CNTs were imaged under 90x magnification on a Nikon fluorescence microscope fitted with B-2A cube (450-490 excitation / 500 emission).

1.23 Results and Discussion

1.23.1 Protein mediated dispersion of SWCNTs in aqueous solvent

Dialysis of detergent-dispersed CNTs (proprietary detergent and sodium cholate) in the absence of sfGFP-Car9 leads to their nearly quantitative precipitation after about 4 buffer exchanges (**Figure 5.1**). On the other hand, samples supplemented with 10 µM of sfGFP-Car9 remain well dispersed under the same conditions and little aggregated material is seen at the bottom of the tube after centrifugation at 14,000*g* for 10 minutes. This result indicates that sfGFP-Car9 binds to the CNTs and prevent the aggregation that occurs when enough of the bound detergent has been removed by dialysis. Because the Car9 tag selectively binds to the hydroxyl-rich edges of carbon nanostructures[278] which are found at the ends of CNTs, the nanotube side-walls presumably remain bound by a small amount of detergent that prevents the hydrophobic side walls from contacting one another to drive aggregation. This hypothesis is supported by the fact that if the sfGFP-Car9-CNT solution is subjected to 7 buffer exchanges (which should deplete the detergent further) the CNT precipitate out of solution within 2 weeks. By contrast, samples subjected to 4 buffer exchanges are stable for 6 months.

1.23.2 Fluorescent imaging of end-labeled SWCNTs

Conjugates between sfGFP-Car9 and CNTs were imaged by fluorescence microscopy at λ_{ex} = 480 nm to excite the GFP fluorophore. However, at the protein concentration used in these experiments (2 μM) the background fluorescence of sfGFP-Car9 was found to dominate. To circumvent this issue, we incubated the protein-CNT solution with silica beads to remove the majority of free sfGFP-Car9 from solution. Imaging the supernatants revealed punctuated fluorescence with a distinct pairing of fluorescent spots that is obvious in magnified images of regions containing few fluorescent spots (**Figure 5.2**, inset). The distance between paired fluorescent spots varied between 0.5 and 3 μm with a 1 μm and 2 μm separations being the most frequent (20% each; **Figure 5.3**). These distances are consistent with the CNT length distribution provided by the manufacturer as our approach biases against spots whose separation distances is smaller than the diffraction limit of light. We conclude that sfGFP-CT43 can be used to selectively label the ends of SWCNTs and improve their solubility.

1.24 Conclusions

In this chapter we have demonstrated sfGFP-Car9's capability to serve as a selective end-labeler of SWCNTs that have been previously dispersed in detergents. The high stability of sfGFP allows it to remain folded during the detergent removal process and upon association with the CNT ends. These results lay the groundwork for patterning SWCNTs with heterobifunctional proteins similar to those described in *Chapter 4*.

1.25 Figures

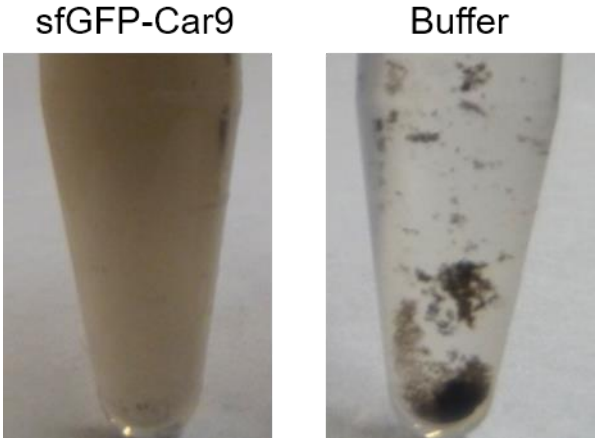

Figure 0.1 SWCNTs resuspended in sodium cholate buffer lacking sfGFP-Car9 precipitate out of solution after 4 cycles of dialysis buffer exchange (right). Samples supplied with 2 µM of sfGFP-Car9 remain well dispersed under the same conditions as there is little precipitate present at the bottom of the tube following centrifugation at 14,000*g* for 10 minutes (left).

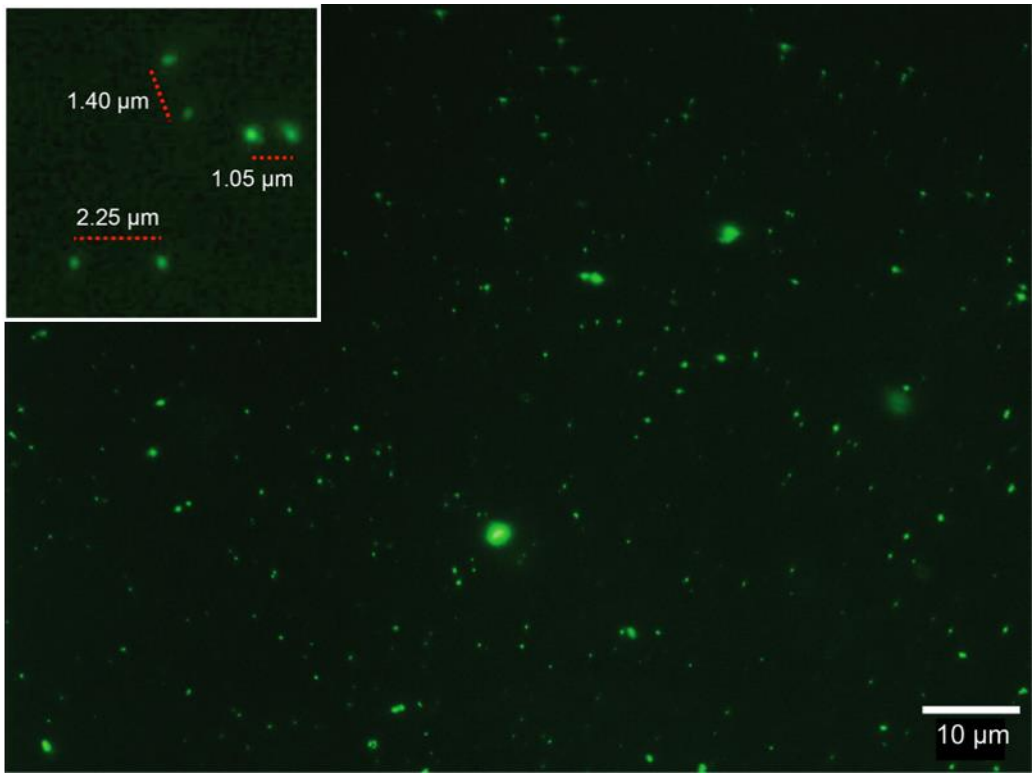

Figure 0.2 Fluorescence microscopy at 90x magnification shows the pairings of sfGFP-CT43 spots at length scales commensurate with those of single-walled carbon nanotubes. The inset is a magnified portion of a low density region that provides a better illustration of the length separating paired fluorophores.

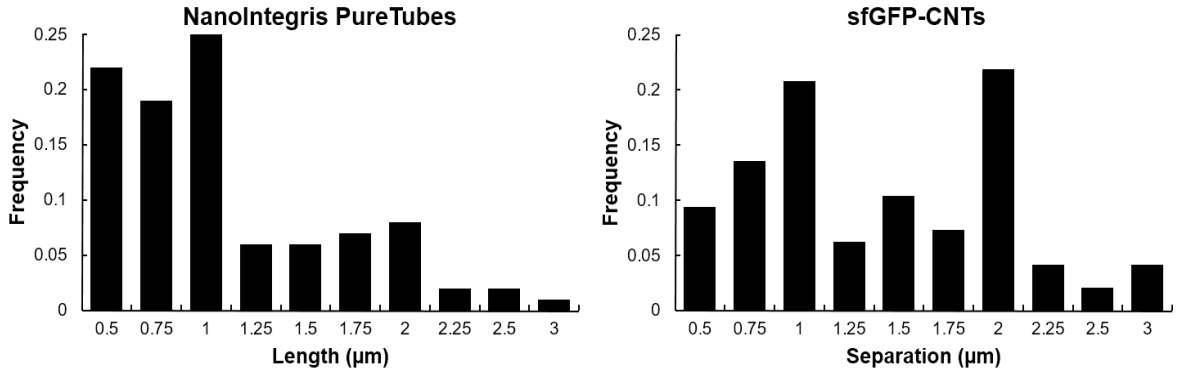

Figure 0.3 The reported values of CNT lengths from the manufacturer (evaluated by TEM, all samples < 0.5 μm pooled) compare favorably with the distribution of lengths between paired sfGFP-CT43 fluorescent spots. A total of 96 pairs were counted to produce the histogram.

Conclusions

Controlled biomineralization of high-value inorganic materials such as QDs will continue to be important as industry strives to improve nanoscale manufacturing. Understanding and utilizing Nature's methods for building complex and hierarchically ordered materials with proteins and peptides is key to this process. This work focused on combining the ability of combinatorially selected SBPs to bind inorganic and synthetic materials with our ability to modify proteins through genetic engineering to create useful, functional nanomaterials with nontoxic compositions via environmentally friendly schemes.

In Chapter 2 we built on previous work utilizing a ZnS binding peptide called CT43 to synthesize fluorescent Mn-doped ZnS QDs by constructing a minimized capping protein in which the BB IgG binding domain is fused to CT43. The resulting QDs exhibited 30% improved fluorescence and a reduction in hydrodynamic diameter while maintaining colloidal stability. They also retained immuno-functionality as evidenced by their ability to bind IgG antibodies through the BB domain.

Chapter 3 focused on how biofabricated nanocrystals such as BB-CT43@ZnS:Mn may impact the environment. We found that these QDs were unable to penetrate unmodified *E. coli.* However, protein-coated nanocrystals readily translocated to the cytoplasm of cells whose membrane had been destabilized by compounds such as $CaCl_2$, as evidenced by spheroplast fluorescence and FRET between QD and a fluorescent protein confined to the cytoplasm. We further found that internalized QDs did not induce a detectable stress response at low dosage, but caused oxidative stress when present at concentrations exceeding 2.5 μg/mL. Finally, we determined that the uptaken nanocrystals were not extruded by the *tolC* export system, but rather

diluted across cell populations during exponential growth, thus posing a minimal risk threat for bioaccumulation.

In Chapter 4 we once again redesigned the protein that caps the growth of ZnS:Mn nanocrystals by appending the CT43 extension to a fluorescent protein, sfGFP. In the resulting system, organic and inorganic fluorophores combine their emission characteristics. We further inserted the silica-binding Car9 sequence within a permissive loop of sfGFP-CT43 to create a fluorescent protein capable of both synthesizing QDs and mediating their binding to silica surfaces. We concurrently developed a method to conjugate a chloramphenicol-specific DNA aptamer to the biofabricated QDs and demonstrated that the resulting inorganic-protein-nucleic acid system was suitable for the qualitative detection of low concentrations of chloramphenicol in aqueous samples. We also laid out the groundwork for site-specific conjugation of aptamers by introducing cysteine residues at two solvent-exposed locations of sfGFP::Car9-CT43.

Finally, in Chapter 5, we demonstrated that sfGFP-Car9 could also be used to label the end of single-walled carbon nanotubes while increasing their solubility. Labeled CNTs were visualized by fluorescence microscopy and the calculated size distribution based on fluorophore separation was in good agreement with that provided by the manufacturer.

Collectively, this work demonstrates the usefulness of combining solid binding peptides and protein engineering to control the biomineralization of novel functional nanomaterials and structures. The fabrication methods described in this thesis are inexpensive when biomineralizing proteins are purified by silica chromatography, energy efficient since all reactions are performed under ambient conditions of pressure and temperature, and environmentally friendly since no toxic solvents or precursors are used. In addition to enabling the facile production of immuno-quantum dots and field-deployable sensors for small molecules, the strategies described herein may prove

useful for the development of nanotherapeutics and the protein-guided assembly of novel systems and devices.

References

1. Dickerson, M. B., Sandhage, K. H., and Naik, R. R., Protein- and Peptide-Directed Syntheses of Inorganic Materials. *Chemical Reviews*, 2008. **108**(11): p. 4935-4978.
2. Mann, S., *Biomineralization: Principles and Concepts in Bioinorganic Materials Chemistry*. 2001: Oxford University Press.
3. Weiner, S. and Addadi, L., Design strategies in mineralized biological materials. *Journal of Materials Chemistry*, 1997. **7**(5): p. 689-702.
4. Aizenberg, J., Crystallization in Patterns: A Bio-Inspired Approach. *Advanced Materials*, 2004. **16**(15): p. 1295-1302.
5. Aizenberg, J., Lambert, G., Weiner, S., and Addadi, L., *J. Am. Chem. Soc.*, 2002. **124**: p. 32.
6. Aizenberg, J., Tkachenko, A., Weiner, S., Addadi, L., and Hendler, G., *Nature*, 2001. **412**: p. 819.
7. Lee, J.-H., Lee, J. H., Lee, Y. J., and Nam, K. T., Protein/peptide based nanomaterials for energy application. *Current Opinion in Biotechnology*, 2013. **24**(4): p. 599-605.
8. Hay, S., Wallace, B. B., Smith, T. A., Ghiggino, K. P., and Wydrzynski, T., Protein engineering of cytochrome b562 for quinone binding and light-induced electron transfer. *Proceedings of the National Academy of Sciences of the United States of America*, 2004. **101**(51): p. 17675-17680.
9. Toporik, H., Carmeli, I., Volotsenko, I., Molotskii, M., Rosenwaks, Y., Carmeli, C., and Nelson, N., Large Photovoltages Generated by Plant Photosystem I Crystals. *Advanced Materials*, 2012. **24**(22): p. 2988-2991.
10. Zhou, W. and Baneyx, F., Aqueous, Protein-Driven Synthesis of Transition Metal-Doped ZnS Immuno-Quantum Dots. *ACS Nano*, 2011. **5**(10): p. 8013-8018.
11. Lowenstam, H. A., Minerals formed by organisms. *Science*, 1981. **211**(4487): p. 1126-1131.
12. Reddy, M. S., Biomineralization of calcium carbonates and their engineered applications: a review. *Frontiers in Microbiology*, 2013. **4**.
13. Fu, G., Valiyaveettil, S., Wopenka, B., and Morse, D. E., CaCO3 Biomineralization: Acidic 8-kDa Proteins Isolated from Aragonitic Abalone Shell Nacre Can Specifically Modify Calcite Crystal Morphology. *Biomacromolecules*, 2005. **6**(3): p. 1289-1298.
14. Evans, J. S., "Tuning in" to Mollusk Shell Nacre- and Prismatic-Associated Protein Terminal Sequences. Implications for Biomineralization and the Construction of High Performance Inorganic−Organic Composites. *Chemical Reviews*, 2008. **108**(11): p. 4455-4462.
15. Addadi, L., Joester, D., Nudelman, F., and Weiner, S., Mollusk Shell Formation: A Source of New Concepts for Understanding Biomineralization Processes. *Chemistry – A European Journal*, 2006. **12**(4): p. 980-987.
16. Currey, J. D., Mechanical Properties of Mother of Pearl in Tension. *Proceedings of the Royal Society of London B: Biological Sciences*, 1977. **196**(1125): p. 443-463.
17. Watabe, N., Studies on shell formation: XI. Crystal—matrix relationships in the inner layers of mollusk shells. *Journal of Ultrastructure Research*, 1965. **12**(3): p. 351-370.
18. Sun, J. and Bhushan, B., Hierarchical structure and mechanical properties of nacre: a review. *RSC Advances*, 2012. **2**(20): p. 7617-7632.

19. Behr, S., Vainio, U., Müller, M., Schreyer, A., and Schneider, G. A., Large-scale parallel alignment of platelet-shaped particles through gravitational sedimentation. *Scientific Reports*, 2015. **5**: p. 9984.
20. Weiner, S., Traub, W., and Parker, S. B., Macromolecules in Mollusc Shells and Their Functions in Biomineralization [and Discussion]. *Philosophical Transactions of the Royal Society of London B: Biological Sciences*, 1984. **304**(1121): p. 425-434.
21. Kröger, N., Deutzmann, R., and Sumper, M., Polycationic Peptides from Diatom Biosilica That Direct Silica Nanosphere Formation. *Science*, 1999. **286**(5442): p. 1129-1132.
22. Marner, W. D., Shaikh, A. S., Muller, S. J., and Keasling, J. D., Morphology of Artificial Silica Matrices Formed via Autosilification of a Silaffin/Protein Polymer Chimera. *Biomacromolecules*, 2008. **9**(1): p. 1-5.
23. Kröger, N., Lorenz, S., Brunner, E., and Sumper, M., Self-Assembly of Highly Phosphorylated Silaffins and Their Function in Biosilica Morphogenesis. *Science*, 2002. **298**(5593): p. 584-586.
24. Cha, J. N., Shimizu, K., Zhou, Y., Christiansen, S. C., Chmelka, B. F., Stucky, G. D., and Morse, D. E., Silicatein filaments and subunits from a marine sponge direct the polymerization of silica and silicones in vitro. *Proceedings of the National Academy of Sciences*, 1999. **96**(2): p. 361-365.
25. Shimizu, K., Cha, J., Stucky, G. D., and Morse, D. E., Silicatein α: Cathepsin L-like protein in sponge biosilica. *Proceedings of the National Academy of Sciences*, 1998. **95**(11): p. 6234-6238.
26. Tahir, M. N., Theato, P., Muller, W. E. G., Schroder, H. C., Janshoff, A., Zhang, J., Huth, J., and Tremel, W., Monitoring the formation of biosilica catalysed by histidine-tagged silicatein. *Chemical Communications*, 2004(24): p. 2848-2849.
27. Brutchey, R. L. and Morse, D. E., Silicatein and the Translation of its Molecular Mechanism of Biosilicification into Low Temperature Nanomaterial Synthesis. *Chemical Reviews*, 2008. **108**(11): p. 4915-4934.
28. Zhou, Y., Shimizu, K., Cha, J. N., Stucky, G. D., and Morse, D. E., Efficient Catalysis of Polysiloxane Synthesis by Silicatein α Requires Specific Hydroxy and Imidazole Functionalities. *Angewandte Chemie International Edition*, 1999. **38**(6): p. 779-782.
29. Collino, S. and Evans, J. S., Structural Features That Distinguish Kinetically Distinct Biomineralization Polypeptides. *Biomacromolecules*, 2007. **8**(5): p. 1686-1694.
30. Sano, K.-I., Sasaki, H., and Shiba, K., Specificity and Biomineralization Activities of Ti-Binding Peptide-1 (TBP-1). *Langmuir*, 2005. **21**(7): p. 3090-3095.
31. Thai, C. K., Dai, H., Sastry, M. S. R., Sarikaya, M., Schwartz, D. T., and Baneyx, F., Identification and characterization of Cu2O- and ZnO-binding polypeptides by Escherichia coli cell surface display: toward an understanding of metal oxide binding. *Biotechnology and Bioengineering*, 2004. **87**(2): p. 129-137.
32. Currie, H. A. and Perry, C. C., Silica in Plants: Biological, Biochemical and Chemical Studies. *Annals of Botany*, 2007. **100**(7): p. 1383-1389.
33. Voronkov, M. G., Zelchan, G. I., and Lukevits, E. J., *Silicon and Life*. 1971.
34. Iler, R. K., *The Chemistry of Silica*. 1979.
35. Patwardhan, S. V., Clarson, S. J., and Perry, C. C., On the role(s) of additives in bioinspired silicification. *Chemical Communications*, 2005(9): p. 1113-1121.
36. Perry, C. C. and Keeling-Tucker, T., Biosilicification: the role of the organic matrix in structure control. *JBIC Journal of Biological Inorganic Chemistry*. **5**(5): p. 537-550.

37. Shiomi, T., Tsunoda, T., Kawai, A., Mizukami, F., and Sakaguchi, K., Biomimetic Synthesis of Lysozyme−Silica Hybrid Hollow Particles Using Sonochemical Treatment: Influence of pH and Lysozyme Concentration on Morphology. *Chemistry of Materials*, 2007. **19**(18): p. 4486-4493.
38. Simpson, T. L. and Volcani, B. E., *Silicon and Siliceous Structures in Biological Systems*. 1981.
39. Harrison, C. C., Evidence for intramineral macromolecules containing protein from plant silicas. *Phytochemistry*, 1996. **41**(1): p. 37-42.
40. Hildebrand, M., Diatoms, Biomineralization Processes, and Genomics. *Chemical Reviews*, 2008. **108**(11): p. 4855-4874.
41. Addadi, L., Raz, S., and Weiner, S., Taking Advantage of Disorder: Amorphous Calcium Carbonate and Its Roles in Biomineralization. *Advanced Materials*, 2003. **15**(12): p. 959-970.
42. Sommerdijk, N. A. J. M. and With, G. d., Biomimetic CaCO3 Mineralization using Designer Molecules and Interfaces. *Chemical Reviews*, 2008. **108**(11): p. 4499-4550.
43. Sarikaya, M., Tamerler, C., Jen, A. K. Y., Schulten, K., and Baneyx, F., Molecular biomimetics: nanotechnology through biology. *Nat Mater*, 2003. **2**(9): p. 577-585.
44. Heinz, H., Farmer, B. L., Pandey, R. B., Slocik, J. M., Patnaik, S. S., Pachter, R., and Naik, R. R., Nature of Molecular Interactions of Peptides with Gold, Palladium, and Pd−Au Bimetal Surfaces in Aqueous Solution. *Journal of the American Chemical Society*, 2009. **131**(28): p. 9704-9714.
45. Hnilova, M., Oren, E. E., Seker, U. O. S., Wilson, B. R., Collino, S., Evans, J. S., Tamerler, C., and Sarikaya, M., Effect of Molecular Conformations on the Adsorption Behavior of Gold-Binding Peptides. *Langmuir*, 2008. **24**(21): p. 12440-12445.
46. Hall Sedlak, R., Hnilova, M., Grosh, C., Fong, H., Baneyx, F., Schwartz, D., Sarikaya, M., Tamerler, C., and Traxler, B., An engineered Escherichia coli silver-binding periplasmic protein promotes silver tolerance. *Applied and Environmental Microbiology*, 2012.
47. Sewell, S. L. and Wright, D. W., Biomimetic Synthesis of Titanium Dioxide Utilizing the R5 Peptide Derived from Cylindrotheca fusiformis. *Chemistry of Materials*, 2006. **18**(13): p. 3108-3113.
48. Coyle, B. L. and Baneyx, F., A cleavable silica-binding affinity tag for rapid and inexpensive protein purification. *Biotechnology and Bioengineering*, 2014. **111**(10): p. 2019-2026.
49. Cha, J. N., Stucky Gd Fau - Morse, D. E., Morse De Fau - Deming, T. J., and Deming, T. J., Biomimetic synthesis of ordered silica structures mediated by block copolypeptides. (0028-0836 (Print)).
50. Kitayaporn, S., Zhou, W., Schwartz, D. T., and Baneyx, F., Laying out ground rules for protein-aided nanofabrication: ZnO synthesis at 70°C as a case study. *Biotechnology and Bioengineering*, 2012. **109**(8): p. 1912-1918.
51. Zhou, W., Schwartz, D. T., and Baneyx, F., Single-Pot Biofabrication of Zinc Sulfide Immuno-Quantum Dots. *Journal of the American Chemical Society*, 2010. **132**(13): p. 4731-4738.
52. Coyle, B. L., Rolandi M Fau - Baneyx, F., and Baneyx, F., Carbon-binding designer proteins that discriminate between sp2- and sp3-hybridized carbon surfaces. (1520-5827 (Electronic)).

53. Chiu, D., Zhou, W., Kitayaporn, S., Schwartz, D. T., Murali-Krishna, K., Kavanagh, T. J., and Baneyx, F., Biomineralization and Size Control of Stable Calcium Phosphate Core–Protein Shell Nanoparticles: Potential for Vaccine Applications. *Bioconjugate Chemistry*, 2012. **23**(3): p. 610-617.
54. Peelle, B. R., Krauland, E. M., Wittrup, K. D., and Belcher, A. M., Probing the interface between biomolecules and inorganic materials using yeast surface display and genetic engineering. *Acta Biomaterialia*, 2005. **1**(2): p. 145-154.
55. Merzlyak, A. and Lee, S.-W., Phage as templates for hybrid materials and mediators for nanomaterial synthesis. *Current Opinion in Chemical Biology*, 2006. **10**(3): p. 246-252.
56. Parmley, S. F. and Smith, G. P., Antibody-selectable filamentous fd phage vectors: affinity purification of target genes. *Gene*, 1988. **73**(2): p. 305-318.
57. Lu, Z., Murray, K. S., Cleave, V. V., LaVallie, E. R., Stahl, M. L., and McCoy, J. M., Expression of Thioredoxin Random Peptide Libraries on the Escherichia coli Cell Surface as Functional Fusions to Flagellin: A System Designed for Exploring Protein-Protein Interactions. *Nat Biotech*, 1995. **13**(4): p. 366-372.
58. Moreau, J. W., Weber, P. K., Martin, M. C., Gilbert, B., Hutcheon, I. D., and Banfield, J. F., Extracellular Proteins Limit the Dispersal of Biogenic Nanoparticles. *Science*, 2007. **316**(5831): p. 1600-1603.
59. Klug, A. and Rhodes, D., Zinc Fingers: A Novel Protein Fold for Nucleic Acid Recognition. *Cold Spring Harbor Symposia on Quantitative Biology*, 1987. **52**: p. 473-482.
60. Pavletich, N. P. and Pabo, C. O., Zinc finger-DNA recognition: crystal structure of a Zif268-DNA complex at 2.1 A. *Science*, 1991. **252**(5007): p. 809-817.
61. Reddy, B. A., Etkin, L. D., and Freemont, P. S., A novel zinc finger coiled-coil domain in a family of nuclear proteins. *Trends in Biochemical Sciences*, 1992. **17**(9): p. 344-345.
62. Slocik, J. M., Moore, J. T., and Wright, D. W., Monoclonal Antibody Recognition of Histidine-Rich Peptide Encapsulated Nanoclusters. *Nano Letters*, 2002. **2**(3): p. 169-173.
63. Deonarine, A., Lau, B. L. T., Aiken, G. R., Ryan, J. N., and Hsu-Kim, H., Effects of Humic Substances on Precipitation and Aggregation of Zinc Sulfide Nanoparticles. *Environmental Science & Technology*, 2011. **45**(8): p. 3217-3223.
64. Lau, B. L. T. and Hsu-Kim, H., Precipitation and Growth of Zinc Sulfide Nanoparticles in the Presence of Thiol-Containing Natural Organic Ligands. *Environmental Science & Technology*, 2008. **42**(19): p. 7236-7241.
65. Bae, W., Abdullah, R., Henderson, D., and Mehra, R. K., Characteristics of Glutathione-Capped ZnS Nanocrystallites. *Biochemical and Biophysical Research Communications*, 1997. **237**(1): p. 16-23.
66. Kho, R., Nguyen, L., Torres-Martínez, C. L., and Mehra, R. K., Zinc–Histidine as Nucleation Centers for Growth of ZnS Nanocrystals. *Biochemical and Biophysical Research Communications*, 2000. **272**(1): p. 29-35.
67. Banerjee, I. A., Yu, L., and Matsui, H., Room-Temperature Wurtzite ZnS Nanocrystal Growth on Zn Finger-like Peptide Nanotubes by Controlling Their Unfolding Peptide Structures. *Journal of the American Chemical Society*, 2005. **127**(46): p. 16002-16003.
68. Flynn, C. E., Mao, C., Hayhurst, A., Williams, J. L., Georgiou, G., Iverson, B., and Belcher, A. M., Synthesis and organization of nanoscale II-VI semiconductor materials using evolved peptide specificity and viral capsid assembly. *Journal of Materials Chemistry*, 2003. **13**(10): p. 2414-2421.

69. Zhou, W. and Baneyx, F., Biofabrication of ZnS:Mn luminescent nanocrystals using histidine, hexahistidine, and His-tagged proteins: A comparison study. *Biochemical Engineering Journal*, 2014. **89**: p. 28-32.
70. Kuo, W.-H. K. and Chase, H. A., Exploiting the interactions between poly-histidine fusion tags and immobilized metal ions. *Biotechnology Letters*, 2011. **33**(6): p. 1075-1084.
71. Slocik, J. M. and Naik, R. R., Probing peptide-nanomaterial interactions. *Chemical Society Reviews*, 2010. **39**(9): p. 3454-3463.
72. Poulsen, N., Sumper, M., and Kröger, N., Biosilica formation in diatoms: Characterization of native silaffin-2 and its role in silica morphogenesis. *Proceedings of the National Academy of Sciences*, 2003. **100**(21): p. 12075-12080.
73. Rodríguez, F., Glawe, D. D., Naik, R. R., Hallinan, K. P., and Stone, M. O., Study of the Chemical and Physical Influences upon in Vitro Peptide-Mediated Silica Formation. *Biomacromolecules*, 2004. **5**(2): p. 261-265.
74. Brus, L., Quantum crystallites and nonlinear optics. *Applied Physics A*. **53**(6): p. 465-474.
75. Brus, L. E., A simple model for the ionization potential, electron affinity, and aqueous redox potentials of small semiconductor crystallites. *The Journal of Chemical Physics*, 1983. **79**(11): p. 5566-5571.
76. Hilinski, E. F., Lucas, P. A., and Wang, Y., A picosecond bleaching study of quantum-confined cadmium sulfide microcrystallites in a polymer film. *The Journal of Chemical Physics*, 1988. **89**(6): p. 3435-3441.
77. Bawendi, M. G., Steigerwald, M. L., and Brus, L. E., The Quantum Mechanics of Larger Semiconductor Clusters ("Quantum Dots"). *Annual Review of Physical Chemistry*, 1990. **41**(1): p. 477-496.
78. Efros, A. L., Rosen, M., Kuno, M., Nirmal, M., Norris, D. J., and Bawendi, M., Band-edge exciton in quantum dots of semiconductors with a degenerate valence band: Dark and bright exciton states. *Physical Review B*, 1996. **54**(7): p. 4843-4856.
79. Murray, C. B., Norris, D. J., and Bawendi, M. G., Synthesis and characterization of nearly monodisperse CdE (E = sulfur, selenium, tellurium) semiconductor nanocrystallites. *Journal of the American Chemical Society*, 1993. **115**(19): p. 8706-8715.
80. Hu, Y. Z., Koch, S. W., and Thoai, D. B. T., Quantum Confinement and Coulomb Effects in Semiconductor Quantum Dots. *Modern Physics Letters B*, 1990. **04**(16): p. 1009-1016.
81. Chen, Y. and Rosenzweig, Z., Luminescent CdS Quantum Dots as Selective Ion Probes. *Analytical Chemistry*, 2002. **74**(19): p. 5132-5138.
82. Sun, W.-T., Yu, Y., Pan, H.-Y., Gao, X.-F., Chen, Q., and Peng, L.-M., CdS Quantum Dots Sensitized TiO2 Nanotube-Array Photoelectrodes. *Journal of the American Chemical Society*, 2008. **130**(4): p. 1124-1125.
83. Baker, D. R. and Kamat, P. V., Photosensitization of TiO2 Nanostructures with CdS Quantum Dots: Particulate versus Tubular Support Architectures. *Advanced Functional Materials*, 2009. **19**(5): p. 805-811.
84. Talapin, D. V., Haubold, S., Rogach, A. L., Kornowski, A., Haase, M., and Weller, H., A Novel Organometallic Synthesis of Highly Luminescent CdTe Nanocrystals. *The Journal of Physical Chemistry B*, 2001. **105**(12): p. 2260-2263.
85. Gaponik, N., Talapin, D. V., Rogach, A. L., Hoppe, K., Shevchenko, E. V., Kornowski, A., Eychmüller, A., and Weller, H., Thiol-Capping of CdTe Nanocrystals: An Alternative to Organometallic Synthetic Routes. *The Journal of Physical Chemistry B*, 2002. **106**(29): p. 7177-7185.

86. Wuister, S. F., Swart, I., van Driel, F., Hickey, S. G., and de Mello Donegá, C., Highly Luminescent Water-Soluble CdTe Quantum Dots. *Nano Letters*, 2003. **3**(4): p. 503-507.
87. Zheng, Y., Gao, S., and Ying, J. Y., Synthesis and Cell-Imaging Applications of Glutathione-Capped CdTe Quantum Dots. *Advanced Materials*, 2007. **19**(3): p. 376-380.
88. Liao, M. C. H., Chang, Y. H., Chen, Y. F., Hsu, J. W., Lin, J. M., and Chou, W. C., Fabrication of ZnSe quantum dots under Volmer–Weber mode by metalorganic chemical vapor deposition. *Applied Physics Letters*, 1997. **70**(17): p. 2256-2258.
89. Smith, C. A., Lee, H. W. H., Leppert, V. J., and Risbud, S. H., Ultraviolet-blue emission and electron-hole states in ZnSe quantum dots. *Applied Physics Letters*, 1999. **75**(12): p. 1688-1690.
90. Chen, H. S., Wang, S. J. J., Lo, C. J., and Chi, J. Y., White-light emission from organics-capped ZnSe quantum dots and application in white-light-emitting diodes. *Applied Physics Letters*, 2005. **86**(13): p. 131905.
91. Micic, O. I., Curtis, C. J., Jones, K. M., Sprague, J. R., and Nozik, A. J., Synthesis and Characterization of InP Quantum Dots. *The Journal of Physical Chemistry*, 1994. **98**(19): p. 4966-4969.
92. Mićić, O. I., Sprague, J., Lu, Z., and Nozik, A. J., Highly efficient band-edge emission from InP quantum dots. *Applied Physics Letters*, 1996. **68**(22): p. 3150-3152.
93. Bharali, D. J., Lucey, D. W., Jayakumar, H., Pudavar, H. E., and Prasad, P. N., Folate-Receptor-Mediated Delivery of InP Quantum Dots for Bioimaging Using Confocal and Two-Photon Microscopy. *Journal of the American Chemical Society*, 2005. **127**(32): p. 11364-11371.
94. Marzin, J. Y., Gérard, J. M., Izraël, A., Barrier, D., and Bastard, G., Photoluminescence of Single InAs Quantum Dots Obtained by Self-Organized Growth on GaAs. *Physical Review Letters*, 1994. **73**(5): p. 716-719.
95. Lubyshev, D. I., González-Borrero, P. P., Marega, E., Petitprez, E., La Scala, N., and Basmaji, P., Exciton localization and temperature stability in self-organized InAs quantum dots. *Applied Physics Letters*, 1996. **68**(2): p. 205-207.
96. Lee, S.-W., Hirakawa, K., and Shimada, Y., Bound-to-continuum intersubband photoconductivity of self-assembled InAs quantum dots in modulation-doped heterostructures. *Applied Physics Letters*, 1999. **75**(10): p. 1428-1430.
97. Fukui, T., Ando, S., Tokura, Y., and Toriyama, T., GaAs tetrahedral quantum dot structures fabricated using selective area metalorganic chemical vapor deposition. *Applied Physics Letters*, 1991. **58**(18): p. 2018-2020.
98. Gammon, D., Snow, E. S., Shanabrook, B. V., Katzer, D. S., and Park, D., Fine Structure Splitting in the Optical Spectra of Single GaAs Quantum Dots. *Physical Review Letters*, 1996. **76**(16): p. 3005-3008.
99. Moreels, I., Lambert, K., Smeets, D., De Muynck, D., Nollet, T., Martins, J. C., Vanhaecke, F., Vantomme, A., Delerue, C., Allan, G., and Hens, Z., Size-Dependent Optical Properties of Colloidal PbS Quantum Dots. *ACS Nano*, 2009. **3**(10): p. 3023-3030.
100. Ellingson, R. J., Beard, M. C., Johnson, J. C., Yu, P., Micic, O. I., Nozik, A. J., Shabaev, A., and Efros, A. L., Highly Efficient Multiple Exciton Generation in Colloidal PbSe and PbS Quantum Dots. *Nano Letters*, 2005. **5**(5): p. 865-871.
101. Steckel, J. S., Coe-Sullivan, S., Bulović, V., and Bawendi, M. G., 1.3 μm to 1.55 μm Tunable Electroluminescence from PbSe Quantum Dots Embedded within an Organic Device. *Advanced Materials*, 2003. **15**(21): p. 1862-1866.

102. Pietryga, J. M., Schaller, R. D., Werder, D., Stewart, M. H., Klimov, V. I., and Hollingsworth, J. A., Pushing the Band Gap Envelope: Mid-Infrared Emitting Colloidal PbSe Quantum Dots. *Journal of the American Chemical Society*, 2004. **126**(38): p. 11752-11753.
103. Michalet, X., Pinaud, F. F., Bentolila, L. A., Tsay, J. M., Doose, S., Li, J. J., Sundaresan, G., Wu, A. M., Gambhir, S. S., and Weiss, S., Quantum Dots for Live Cells, in Vivo Imaging, and Diagnostics. *Science*, 2005. **307**(5709): p. 538-544.
104. Danek, M., Jensen, K. F., Murray, C. B., and Bawendi, M. G., Synthesis of Luminescent Thin-Film CdSe/ZnSe Quantum Dot Composites Using CdSe Quantum Dots Passivated with an Overlayer of ZnSe. *Chemistry of Materials*, 1996. **8**(1): p. 173-180.
105. Spanhel, L., Haase, M., Weller, H., and Henglein, A., Photochemistry of colloidal semiconductors. 20. Surface modification and stability of strong luminescing CdS particles. *Journal of the American Chemical Society*, 1987. **109**(19): p. 5649-5655.
106. Hines, M. A. and Guyot-Sionnest, P., Synthesis and Characterization of Strongly Luminescing ZnS-Capped CdSe Nanocrystals. *The Journal of Physical Chemistry*, 1996. **100**(2): p. 468-471.
107. Talapin, D. V., Rogach, A. L., Kornowski, A., Haase, M., and Weller, H., Highly Luminescent Monodisperse CdSe and CdSe/ZnS Nanocrystals Synthesized in a Hexadecylamine−Trioctylphosphine Oxide−Trioctylphospine Mixture. *Nano Letters*, 2001. **1**(4): p. 207-211.
108. Dabbousi, B. O., Rodriguez-Viejo, J., Mikulec, F. V., Heine, J. R., Mattoussi, H., Ober, R., Jensen, K. F., and Bawendi, M. G., (CdSe)ZnS Core−Shell Quantum Dots: Synthesis and Characterization of a Size Series of Highly Luminescent Nanocrystallites. *The Journal of Physical Chemistry B*, 1997. **101**(46): p. 9463-9475.
109. de Mello Donegá, C., Hickey, S. G., Wuister, S. F., Vanmaekelbergh, D., and Meijerink, A., Single-Step Synthesis to Control the Photoluminescence Quantum Yield and Size Dispersion of CdSe Nanocrystals. *The Journal of Physical Chemistry B*, 2002. **107**(2): p. 489-496.
110. Hao, J.-j., Zhou, J., and Zhang, C.-y., A tri-n-octylphosphine-assisted successive ionic layer adsorption and reaction method to synthesize multilayered core-shell CdSe-ZnS quantum dots with extremely high quantum yield. *Chemical Communications*, 2013. **49**(56): p. 6346-6348.
111. Roy, D., Routh, T., Asaithambi, A. V., Mandal, S., and Mandal, P. K., Spectral and Temporal Optical Behavior of Blue-, Green-, Orange-, and Red-Emitting CdSe-Based Core/Gradient Alloy Shell/Shell Quantum Dots: Ensemble and Single-Particle Investigation Results. *The Journal of Physical Chemistry C*, 2016.
112. Cho, J., Jung, Y. K., and Lee, J.-K., Kinetic studies on the formation of various II-VI semiconductor nanocrystals and synthesis of gradient alloy quantum dots emitting in the entire visible range. *Journal of Materials Chemistry*, 2012. **22**(21): p. 10827-10833.
113. Zrazhevskiy, P., Sena, M., and Gao, X., Designing multifunctional quantum dots for bioimaging, detection, and drug delivery. *Chemical Society Reviews*, 2010. **39**(11): p. 4326-4354.
114. Frigerio, C., Ribeiro, D. S. M., Rodrigues, S. S. M., Abreu, V. L. R. G., Barbosa, J. A. C., Prior, J. A. V., Marques, K. L., and Santos, J. L. M., Application of quantum dots as analytical tools in automated chemical analysis: A review. *Analytica Chimica Acta*, 2012. **735**(0): p. 9-22.

115. Sun, Q., Wang, Y. A., Li, L. S., Wang, D., Zhu, T., Xu, J., Yang, C., and Li, Y., Bright, multicoloured light-emitting diodes based on quantum dots. *Nat Photon*, 2007. **1**(12): p. 717-722.
116. Shirasaki, Y., Supran, G. J., Bawendi, M. G., and Bulovic, V., Emergence of colloidal quantum-dot light-emitting technologies. *Nat Photon*, 2013. **7**(1): p. 13-23.
117. Nozik, A. J., Beard, M. C., Luther, J. M., Law, M., Ellingson, R. J., and Johnson, J. C., Semiconductor Quantum Dots and Quantum Dot Arrays and Applications of Multiple Exciton Generation to Third-Generation Photovoltaic Solar Cells. *Chemical Reviews*, 2010. **110**(11): p. 6873-6890.
118. Oliver, J. *Quantum Dots: Global Market Growth and Future Commercial Prospects*. 2014; Available from: http://www.bccresearch.com/market-research/nanotechnology/quantum-dots-nanomaterials-nan027d.html.
119. Perry, T. *Placing Bets on the New TV Technologies*. 2015; Available from: http://spectrum.ieee.org/tech-talk/consumer-electronics/audiovideo/ces-2015-placing-bets-on-the-new-tv-technologies.
120. Park, J., Joo, J., Kwon, S. G., Jang, Y., and Hyeon, T., Synthesis of monodisperse spherical nanocrystals. *Angew Chem. Int. Ed.*, 2007. **46**: p. 4630-4660.
121. Dubertret, B., Skourides, P., Norris, D. J., Noireaux, V., Brivanlou, A. H., and Libchaber, A., In Vivo Imaging of Quantum Dots Encapsulated in Phospholipid Micelles. *Science*, 2002. **298**(5599): p. 1759-1762.
122. Wu, X., Liu, H., Liu, J., Haley, K. N., Treadway, J. A., Larson, J. P., Ge, N., Peale, F., and Bruchez, M. P., Immunofluorescent labeling of cancer marker Her2 and other cellular targets with semiconductor quantum dots. *Nat Biotech*, 2003. **21**(1): p. 41-46.
123. Ballou, B., Lagerholm, B. C., Ernst, L. A., Bruchez, M. P., and Waggoner, A. S., Noninvasive Imaging of Quantum Dots in Mice. *Bioconjugate Chemistry*, 2004. **15**(1): p. 79-86.
124. Gao, X., Cui, Y., Levenson, R. M., Chung, L. W. K., and Nie, S., In vivo cancer targeting and imaging with semiconductor quantum dots. *Nat Biotech*, 2004. **22**(8): p. 969-976.
125. Bruchez, M., Moronne, M., Gin, P., Weiss, S., and Alivisatos, A. P., Semiconductor Nanocrystals as Fluorescent Biological Labels. *Science*, 1998. **281**(5385): p. 2013-2016.
126. Mulvaney, P., Liz-Marzan, L. M., Giersig, M., and Ung, T., Silica encapsulation of quantum dots and metal clusters. *Journal of Materials Chemistry*, 2000. **10**(6): p. 1259-1270.
127. Gerion, D., Pinaud, F., Williams, S. C., Parak, W. J., Zanchet, D., Weiss, S., and Alivisatos, A. P., Synthesis and Properties of Biocompatible Water-Soluble Silica-Coated CdSe/ZnS Semiconductor Quantum Dots†. *The Journal of Physical Chemistry B*, 2001. **105**(37): p. 8861-8871.
128. Yi, D. K., Selvan, S. T., Lee, S. S., Papaefthymiou, G. C., Kundaliya, D., and Ying, J. Y., Silica-Coated Nanocomposites of Magnetic Nanoparticles and Quantum Dots. *Journal of the American Chemical Society*, 2005. **127**(14): p. 4990-4991.
129. Chan, W. C. W. and Nie, S., Quantum Dot Bioconjugates for Ultrasensitive Nonisotopic Detection. *Science*, 1998. **281**(5385): p. 2016-2018.
130. Chunyang, Z., Hui, M., Shuming, N., Yao, D., Lei, J., and Dieyan, C., Quantum dot-labeled trichosanthin. *Analyst*, 2000. **125**(6): p. 1029-1031.

131. Mitchell, G. P., Mirkin, C. A., and Letsinger, R. L., Programmed Assembly of DNA Functionalized Quantum Dots. *Journal of the American Chemical Society*, 1999. **121**(35): p. 8122-8123.
132. Wang, S., Mamedova, N., Kotov, N. A., Chen, W., and Studer, J., Antigen/Antibody Immunocomplex from CdTe Nanoparticle Bioconjugates. *Nano Letters*, 2002. **2**(8): p. 817-822.
133. Selvan, S. T., Patra, P. K., Ang, C. Y., and Ying, J. Y., Synthesis of Silica-Coated Semiconductor and Magnetic Quantum Dots and Their Use in the Imaging of Live Cells. *Angewandte Chemie*, 2007. **119**(14): p. 2500-2504.
134. Shukoor, M. I., Natalio, F., Therese, H. A., Tahir, M. N., Ksenofontov, V., Panthöfer, M., Eberhardt, M., Theato, P., Schröder, H. C., Müller, W. E. G., and Tremel, W., Fabrication of a Silica Coating on Magnetic γ-Fe2O3 Nanoparticles by an Immobilized Enzyme. *Chemistry of Materials*, 2008. **20**(11): p. 3567-3573.
135. Pathak, S., Choi, S.-K., Arnheim, N., and Thompson, M. E., Hydroxylated Quantum Dots as Luminescent Probes for in Situ Hybridization. *Journal of the American Chemical Society*, 2001. **123**(17): p. 4103-4104.
136. Biju, V., Itoh, T., Anas, A., Sujith, A., and Ishikawa, M., Semiconductor quantum dots and metal nanoparticles: syntheses, optical properties, and biological applications. *Analytical and Bioanalytical Chemistry*, 2008. **391**(7): p. 2469-2495.
137. Jamieson, T., Bakhshi, R., Petrova, D., Pocock, R., Imani, M., and Seifalian, A. M., Biological applications of quantum dots. *Biomaterials*, 2007. **28**(31): p. 4717-4732.
138. Medintz, I. L., Uyeda, H. T., Goldman, E. R., and Mattoussi, H., Quantum dot bioconjugates for imaging, labelling and sensing. *Nature Materials*, 2005. **4**(6): p. 435-446.
139. Winnik, F. M. and Maysinger, D., Quantum Dot Cytotoxicity and Ways To Reduce It. *Accounts of Chemical Research*, 2012. **46**(3): p. 672-680.
140. Nel, A. E., Madler, L., Velegol, D., Xia, T., Hoek, E. M. V., Somasundaran, P., Klaessig, F., Castranova, V., and Thompson, M., Understanding biophysicochemical interactions at the nano-bio interface. *Nat Mater*, 2009. **8**(7): p. 543-557.
141. Yaghini, E., Pirker, K. F., Kay, C. W. M., Seifalian, A. M., and MacRobert, A. J., Quantification of Reactive Oxygen Species Generation by Photoexcitation of PEGylated Quantum Dots. *Small*, 2014. **10**(24): p. 5106-5115.
142. Anas, A., Akita, H., Harashima, H., Itoh, T., Ishikawa, M., and Biju, V., Photosensitized Breakage and Damage of DNA by CdSe−ZnS Quantum Dots. *The Journal of Physical Chemistry B*, 2008. **112**(32): p. 10005-10011.
143. Bottrill, M. and Green, M., Some aspects of quantum dot toxicity. *Chemical Communications*, 2011. **47**(25): p. 7039-7050.
144. Derfus, A. M., Chan, W. C. W., and Bhatia, S. N., Probing the Cytotoxicity of Semiconductor Quantum Dots. *Nano Letters*, 2003. **4**(1): p. 11-18.
145. Gomes, S. A., Vieira, C. S., Almeida, D. B., Santos-Mallet, J. R., Menna-Barreto, R. F., Cesar, C. L., and Feder, D., CdTe and CdSe quantum dots cytotoxicity: a comparative study on microorganisms. *Sensors*, 2011. **11**: p. 11664-11678.
146. Green, M. and Howman, E., Semiconductor quantum dots and free radical induced DNA nicking. *Chemical Communications*, 2005(1): p. 121-123.
147. Smith, W. E., Brownell, J., White, C. C., Afsharinejad, Z., Tsai, J., Hu, X., Polyak, S. J., Gao, X., Kavanagh, T. J., and Eaton, D. L., In Vitro Toxicity Assessment of Amphiphillic

Polymer-Coated CdSe/ZnS Quantum Dots in Two Human Liver Cell Models. *ACS Nano*, 2012. **6**(11): p. 9475-9484.
148. Choi, H. S., Liu, W., Misra, P., Tanaka, E., Zimmer, J. P., Ipe, B. I., Bawendi, M. G., and Frangioni, J. V., Renal clearance of quantum dots. *Nat. Biotechnol.*, 2007. **25**: p. 1165-1170.
149. Hoshino, A., Hanada, S., and Yamamoto, K., Toxicity of nanocrystal quantum dots: the relevance of surface modifications. *Archives of Toxicology*, 2011. **85**(7): p. 707-720.
150. Yong, K.-T., Law, W.-C., Hu, R., Ye, L., Liu, L., Swihart, M. T., and Prasad, P. N., Nanotoxicity assessment of quantum dots: from cellular to primate studies. *Chemical Society Reviews*, 2013. **42**(3): p. 1236-1250.
151. Pietroiusti, A., Magrini, A., and Campagnolo, L., New frontiers in nanotoxicology: Gut microbiota/microbiome-mediated effects of engineered nanomaterials. *Toxicology and Applied Pharmacology*.
152. Kloepfer, J. A., Mielke, R. E., and Nadeau, J. L., Uptake of CdSe and CdSe/ZnS Quantum Dots into Bacteria via Purine-Dependent Mechanisms. *Applied and Environmental Microbiology*, 2005. **71**(5): p. 2548-2557.
153. Mahendra, S., Zhu, H., Colvin, V. L., and Alvarez, P. J., Quantum Dot Weathering Results in Microbial Toxicity. *Environmental Science & Technology*, 2008. **42**(24): p. 9424-9430.
154. Raphaël, S., Cécile, W., Hélène, G., Lavinia, B., Jacques, L., and Christophe, M., The exposure of bacteria to CdTe-core quantum dots: the importance of surface chemistry on cytotoxicity. *Nanotechnology*, 2009. **20**(22): p. 225101.
155. Prasher, D. C., Eckenrode Vk Fau - Ward, W. W., Ward Ww Fau - Prendergast, F. G., Prendergast Fg Fau - Cormier, M. J., and Cormier, M. J., Primary structure of the Aequorea victoria green-fluorescent protein. (0378-1119 (Print)).
156. Chalfie, M., Tu Y Fau - Euskirchen, G., Euskirchen G Fau - Ward, W. W., Ward Ww Fau - Prasher, D. C., and Prasher, D. C., Green fluorescent protein as a marker for gene expression. (0036-8075 (Print)).
157. Yang, F., Moss, L. G., and Phillips, G. N., The molecular structure of green fluorescent protein. *Nat Biotech*, 1996. **14**(10): p. 1246-1251.
158. Zhuo, L., Sun, B., Zhang, C.-L., Fine, A., Chiu, S.-Y., and Messing, A., Live Astrocytes Visualized by Green Fluorescent Protein in Transgenic Mice. *Developmental Biology*, 1997. **187**(1): p. 36-42.
159. Persons, D. A., Allay, J. A., Riberdy, J. M., Wersto, R. P., Donahue, R. E., Sorrentino, B. P., and Nienhuis, A. W., Use of the green fluorescent protein as a marker to identify and track genetically modified hematopoietic cells. *Nat Med*, 1998. **4**(10): p. 1201-1205.
160. Adams, C. L., Chen, Y.-T., Smith, S. J., and James Nelson, W., Mechanisms of Epithelial Cell–Cell Adhesion and Cell Compaction Revealed by High-resolution Tracking of E-Cadherin– Green Fluorescent Protein. *The Journal of Cell Biology*, 1998. **142**(4): p. 1105-1119.
161. Jung, S., Aliberti, J., Graemmel, P., Sunshine, M. J., Kreutzberg, G. W., Sher, A., and Littman, D. R., Analysis of Fractalkine Receptor CX3CR1 Function by Targeted Deletion and Green Fluorescent Protein Reporter Gene Insertion. *Molecular and Cellular Biology*, 2000. **20**(11): p. 4106-4114.
162. Andersen, J. B., Sternberg, C., Poulsen, L. K., Bjørn, S. P., Givskov, M., and Molin, S., New Unstable Variants of Green Fluorescent Protein for Studies of Transient Gene

Expression in Bacteria. *Applied and Environmental Microbiology*, 1998. **64**(6): p. 2240-2246.
163. Chalfie, M., Tu, Y., Euskirchen, G., Ward, W. W., and Prasher, D. C., Green fluorescent protein as a marker for gene expression. *Science*, 1994. **263**(5148): p. 802-805.
164. Chudakov, D. M., Verkhusha, V. V., Staroverov, D. B., Souslova, E. A., Lukyanov, S., and Lukyanov, K. A., Photoswitchable cyan fluorescent protein for protein tracking. *Nat Biotech*, 2004. **22**(11): p. 1435-1439.
165. Lukyanov, K. A. and Belousov, V. V., Genetically encoded fluorescent redox sensors. *Biochimica et Biophysica Acta (BBA) - General Subjects*, 2014. **1840**(2): p. 745-756.
166. Cody, C. W., Prasher, D. C., Westler, W. M., Prendergast, F. G., and Ward, W. W., Chemical structure of the hexapeptide chromophore of the Aequorea green-fluorescent protein. *Biochemistry*, 1993. **32**(5): p. 1212-1218.
167. Yang, T.-T., Cheng, L., and Kain, S. R., Optimized Codon Usage and Chromophore Mutations Provide Enhanced Sensitivity with the Green Fluorescent Protein. *Nucleic Acids Research*, 1996. **24**(22): p. 4592-4593.
168. Cormack, B. P., Valdivia, R. H., and Falkow, S., FACS-optimized mutants of the green fluorescent protein (GFP). *Gene*, 1996. **173**(1): p. 33-38.
169. Crameri, A., Whitehorn, E. A., Tate, E., and Stemmer, W. P. C., Improved Green Fluorescent Protein by Molecular Evolution Using DNA Shuffling. *Nat Biotech*, 1996. **14**(3): p. 315-319.
170. Patterson, G. H., Knobel, S. M., Sharif, W. D., Kain, S. R., and Piston, D. W., Use of the green fluorescent protein and its mutants in quantitative fluorescence microscopy. *Biophysical Journal*, 1997. **73**(5): p. 2782-2790.
171. Heim, R., Prasher, D. C., and Tsien, R. Y., Wavelength mutations and posttranslational autoxidation of green fluorescent protein. *Proceedings of the National Academy of Sciences of the United States of America*, 1994. **91**(26): p. 12501-12504.
172. Delagrave, S., Hawtin, R. E., Silva, C. M., Yang, M. M., and Youvan, D. C., Red-Shifted Excitation Mutants of the Green Fluorescent Protein. *Nat Biotech*, 1995. **13**(2): p. 151-154.
173. Pedelacq, J.-D., Cabantous, S., Tran, T., Terwilliger, T. C., and Waldo, G. S., Engineering and characterization of a superfolder green fluorescent protein. *Nat Biotech*, 2006. **24**(1): p. 79-88.
174. Rizzuto, R., Brini, M., Giorgi, F. D., Rossi, R., Heim, R., Tsien, R. Y., and Pozzan, T., Double labelling of subcellular structures with organelle-targeted GFP mutants in vivo. *Current Biology*, 1996. **6**(2): p. 183-188.
175. Karpova, T. S., Baumann, C. T., He, L., Wu, X., Grammer, A., Lipsky, P., Hager, G. L., and McNally, J. G., Fluorescence resonance energy transfer from cyan to yellow fluorescent protein detected by acceptor photobleaching using confocal microscopy and a single laser. *Journal of Microscopy*, 2003. **209**(1): p. 56-70.
176. Griesbeck, O., Baird, G. S., Campbell, R. E., Zacharias, D. A., and Tsien, R. Y., Reducing the Environmental Sensitivity of Yellow Fluorescent Protein: Mechanism and Applications. *Journal of Biological Chemistry*, 2001. **276**(31): p. 29188-29194.
177. Rekas, A., Alattia, J.-R., Nagai, T., Miyawaki, A., and Ikura, M., Crystal Structure of Venus, a Yellow Fluorescent Protein with Improved Maturation and Reduced Environmental Sensitivity. *Journal of Biological Chemistry*, 2002. **277**(52): p. 50573-50578.

178. Nguyen, H. B., Hung, L.-W., Yeates, T. O., Terwilliger, T. C., and Waldo, G. S., Split green fluorescent protein as a modular binding partner for protein crystallization. *Acta Crystallographica Section D: Biological Crystallography*, 2013. **69**(Pt 12): p. 2513-2523.
179. Cabantous, S., Nguyen, H. B., Pedelacq, J.-D., Koraïchi, F., Chaudhary, A., Ganguly, K., Lockard, M. A., Favre, G., Terwilliger, T. C., and Waldo, G. S., A New Protein-Protein Interaction Sensor Based on Tripartite Split-GFP Association. *Scientific Reports*, 2013. **3**: p. 2854.
180. Li, Y., Sierra, A. M., Ai, H.-w., and Campbell, R. E., Identification of Sites Within a Monomeric Red Fluorescent Protein that Tolerate Peptide Insertion and Testing of Corresponding Circular Permutations. *Photochemistry and Photobiology*, 2008. **84**(1): p. 111-119.
181. Manoil, C. and Bailey, J., A simple screen for permissive sites in proteins: analysis of Escherichia coli lac permease1. *Journal of Molecular Biology*, 1997. **267**(2): p. 250-263.
182. Martineau, P., Guillet Jg Fau - Leclerc, C., Leclerc C Fau - Hofnung, M., and Hofnung, M., Expression of heterologous peptides at two permissive sites of the MalE protein: antigenicity and immunogenicity of foreign B-cell and T-cell epitopes. (0378-1119 (Print)).
183. Betton, J. M. and Hofnung, M., In vivo assembly of active maltose binding protein from independently exported protein fragments. *The EMBO Journal*, 1994. **13**(5): p. 1226-1234.
184. Guntas, G. and Ostermeier, M., Creation of an Allosteric Enzyme by Domain Insertion. *Journal of Molecular Biology*, 2004. **336**(1): p. 263-273.
185. Aguilar-Sánchez, C., Hernández-Díaz, I., Lorenzo-Díaz, F., Navarro, J. F., Hughes, T. E., Giraldez, T., and Alvarez de la Rosa, D., Identification of Permissive Insertion Sites for Generating Functional Fluorescent Mineralocorticoid Receptors. *Endocrinology*, 2012. **153**(7): p. 3517-3525.
186. Ruth, N., Quinting, B., Mainil, J., Hallet, B., Frère, J.-M., Huygen, K., and Galleni, M., Creating hybrid proteins by insertion of exogenous peptides into permissive sites of a class A β-lactamase. *FEBS Journal*, 2008. **275**(20): p. 5150-5160.
187. Abedi, M. R., Caponigro, G., and Kamb, A., Green fluorescent protein as a scaffold for intracellular presentation of peptides. *Nucleic Acids Research*, 1998. **26**(2): p. 623-630.
188. Iijima, S., Helical microtubules of graphitic carbon. *Nature*, 1991. **354**(6348): p. 56-58.
189. Galano, A., Carbon nanotubes: promising agents against free radicals. *Nanoscale*, 2010. **2**(3): p. 373-380.
190. Odom, T. W., Huang, J.-L., Kim, P., and Lieber, C. M., Structure and Electronic Properties of Carbon Nanotubes. *The Journal of Physical Chemistry B*, 2000. **104**(13): p. 2794-2809.
191. Terrones, M., Science and Technology of the Twenty-First Century: Synthesis, Properties, and Applications of Carbon Nanotubes. *Annual Review of Materials Research*, 2003. **33**(1): p. 419-501.
192. Dai, H., Carbon Nanotubes: Synthesis, Integration, and Properties. *Accounts of Chemical Research*, 2002. **35**(12): p. 1035-1044.
193. Tans, S. J., Verschueren, A. R. M., and Dekker, C., Room-temperature transistor based on a single carbon nanotube. *Nature*, 1998. **393**(6680): p. 49-52.
194. Park, H., Afzali, A., Han, S.-J., Tulevski, G. S., Franklin, A. D., Tersoff, J., Hannon, J. B., and Haensch, W., High-density integration of carbon nanotubes via chemical self-assembly. *Nat Nano*, 2012. **7**(12): p. 787-791.

195. Futaba, D. N., Hata, K., Yamada, T., Hiraoka, T., Hayamizu, Y., Kakudate, Y., Tanaike, O., Hatori, H., Yumura, M., and Iijima, S., Shape-engineerable and highly densely packed single-walled carbon nanotubes and their application as super-capacitor electrodes. *Nat Mater*, 2006. **5**(12): p. 987-994.
196. De Volder, M. F. L., Tawfick, S. H., Baughman, R. H., and Hart, A. J., Carbon Nanotubes: Present and Future Commercial Applications. *Science*, 2013. **339**(6119): p. 535-539.
197. Baughman, R. H., Zakhidov, A. A., and de Heer, W. A., Carbon Nanotubes--the Route Toward Applications. *Science*, 2002. **297**(5582): p. 787-792.
198. Hong, S. and Myung, S., Nanotube Electronics: A flexible approach to mobility. *Nat Nano*, 2007. **2**(4): p. 207-208.
199. Pop, E., Mann, D., Wang, Q., Goodson, K., and Dai, H., Thermal Conductance of an Individual Single-Wall Carbon Nanotube above Room Temperature. *Nano Letters*, 2006. **6**(1): p. 96-100.
200. Hirsch, A., Functionalization of Single-Walled Carbon Nanotubes. *Angewandte Chemie International Edition*, 2002. **41**(11): p. 1853-1859.
201. Moore, V. C., Strano, M. S., Haroz, E. H., Hauge, R. H., Smalley, R. E., Schmidt, J., and Talmon, Y., Individually Suspended Single-Walled Carbon Nanotubes in Various Surfactants. *Nano Letters*, 2003. **3**(10): p. 1379-1382.
202. O'Connell, M. J., Bachilo, S. M., Huffman, C. B., Moore, V. C., Strano, M. S., Haroz, E. H., Rialon, K. L., Boul, P. J., Noon, W. H., Kittrell, C., Ma, J., Hauge, R. H., Weisman, R. B., and Smalley, R. E., Band Gap Fluorescence from Individual Single-Walled Carbon Nanotubes. *Science*, 2002. **297**(5581): p. 593-596.
203. Franklin, A. D., Electronics: The road to carbon nanotube transistors. *Nature*, 2013. **498**(7455): p. 443-444.
204. Cao, Q. and Han, S.-j., Single-walled carbon nanotubes for high-performance electronics. *Nanoscale*, 2013. **5**(19): p. 8852-8863.
205. Kong, J., Soh, H. T., Cassell, A. M., Quate, C. F., and Dai, H., Synthesis of individual single-walled carbon nanotubes on patterned silicon wafers. *Nature*, 1998. **395**(6705): p. 878-881.
206. Wang, C., Cao, Q., Ozel, T., Gaur, A., Rogers, J. A., and Shim, M., Electronically Selective Chemical Functionalization of Carbon Nanotubes: Correlation between Raman Spectral and Electrical Responses. *Journal of the American Chemical Society*, 2005. **127**(32): p. 11460-11468.
207. Jin, S. H., Dunham, S. N., Song, J., Xie, X., Kim, J.-h., Lu, C., Islam, A., Du, F., Kim, J., Felts, J., Li, Y., Xiong, F., Wahab, M. A., Menon, M., Cho, E., Grosse, K. L., Lee, D. J., Chung, H. U., Pop, E., Alam, M. A., King, W. P., Huang, Y., and Rogers, J. A., Using nanoscale thermocapillary flows to create arrays of purely semiconducting single-walled carbon nanotubes. *Nat Nano*, 2013. **8**(5): p. 347-355.
208. Justino, C. I. L., Rocha-Santos, T. A. P., Duarte, A. C., and Rocha-Santos, T. A. P., Advances in point-of-care technologies with biosensors based on carbon nanotubes. *TrAC Trends in Analytical Chemistry*, 2013. **45**: p. 24-36.
209. Minot, E. D., Janssens, A. M., Heller, I., Heering, H. A., Dekker, C., and Lemay, S. G., Carbon nanotube biosensors: The critical role of the reference electrode. *Applied Physics Letters*, 2007. **91**(9): p. 093507.
210. Lin, Y., Lu, F., Tu, Y., and Ren, Z., Glucose Biosensors Based on Carbon Nanotube Nanoelectrode Ensembles. *Nano Letters*, 2004. **4**(2): p. 191-195.

211. Tang, X., Bansaruntip, S., Nakayama, N., Yenilmez, E., Chang, Y.-l., and Wang, Q., Carbon Nanotube DNA Sensor and Sensing Mechanism. *Nano Letters*, 2006. **6**(8): p. 1632-1636.
212. Chen, Z., Tabakman, S. M., Goodwin, A. P., Kattah, M. G., Daranciang, D., Wang, X., Zhang, G., Li, X., Liu, Z., Utz, P. J., Jiang, K., Fan, S., and Dai, H., Protein microarrays with carbon nanotubes as multicolor Raman labels. *Nat Biotech*, 2008. **26**(11): p. 1285-1292.
213. Kam, N. W. S. and Dai, H., Carbon Nanotubes as Intracellular Protein Transporters: Generality and Biological Functionality. *Journal of the American Chemical Society*, 2005. **127**(16): p. 6021-6026.
214. Gao, L., Nie, L., Wang, T., Qin, Y., Guo, Z., Yang, D., and Yan, X., Carbon Nanotube Delivery of the GFP Gene into Mammalian Cells. *ChemBioChem*, 2006. **7**(2): p. 239-242.
215. Biju, V., Itoh, T., Anas, A., Sujith, A., and Ishikawa, M., Semiconductor quantum dots and metal nanoparticles: syntheses, optical properties and biological applications. *Anal. Bioanal. Chem.*, 2008. **391**: p. 2469-2495.
216. Jamieson, T., Bakhshi, R., Petrova, D., Pocock, R., Imani, M., and Seifalian, A. M., Biological applications of quantum dots. *Biomaterials*, 2007. **28**: p. 4717-4732.
217. Medintz, I. L., Uyeda, H. T., Goldman, E. R., and Mattoussi, H., Quantum dot bioconjugates for imaging, labeling and sensing. *Nat. Mater.*, 2005. **4**: p. 435-446.
218. Winnik, F. M. and Maysinger, D., Quantum dot cytotoxicity and ways to reduce it. *Acc Chem Res*, 2013. **46**(3): p. 672-80.
219. Shiohara, A., Hanada, S., Prabakar, S., Fujioka, K., Lim, T. H., Yamamoto, K., Northcote, P. T., and Tilley, R. D., Chemical reactions on surface molecules attached to silicon quantum dots. *J Am Chem Soc*, 2010. **132**(1): p. 248-53.
220. Zhou, W. and Baneyx, F., Aqueous, protein-driven synthesis of transition metal-doped ZnS immuno-quantum dots. *ACS Nano*, 2011. **5**: p. 8013-8018.
221. Zhou, W., Schwartz, D. T., and Baneyx, F., Single pot biofabrication of zinc sulfide immuno-quantum dots. *J. Am. Chem. Soc.*, 2010. **132**: p. 4731-4738.
222. Oh, E., Delehanty, J. B., Sapsford, K. E., Susumu, K., Goswami, R., Blanco-Canosa, J. B., Dawson, P. E., Granek, J., Shoff, M., Zhang, Q., Goering, P. L., Huston, A., and Medintz, I. L., Cellular uptake and fate of PEGylated gold nanoparticles is dependent on both cell-penetration peptides and particle size. *ACS Nano*, 2011. **5**(8): p. 6434-48.
223. Lu, Z., Murray, K. S., Van Cleave, V., LaVallie, E. R., Stahl, M. L., and McCoy, J. M., Expression of thioredoxin random peptide libraries on the *Escherichia coli* cell surface as functional fusions to flagellin: a system designed for exploring protein-protein interactions. *Biotechnology*, 1995. **13**: p. 366-372.
224. Choe, W. S., Sastry, M. S. R., Thai, C. K., Dai, H., Schwartz, D. T., and Baneyx, F., Conformational control of inorganic adhesion in a designer protein engineered for cuprous oxide binding. *Langmuir*, 2007. **23**: p. 11347-11350.
225. Hnilova, M., Oren, E. E., Seker, U. O. S., Wilson, B. R., Collino, S., Evans, J. S., Tamerler, C., and Sarikaya, M., Effect of molecular conformations on the adsorption behavior of gold-binding peptides. *Langmuir*, 2008. **24**: p. 12440-12445.
226. Seker, U. O. S., Wilson, B., Dincer, S., Kim, I. W., Oren, E. E., Evans, J. S., Tamerler, C., and Sarikaya, M., Adsorption behavior of linear and cyclic genetically engineered platinum binding peptides. *Langmuir*, 2007. **23**: p. 7895-7900.

227. Chiu, D., Zhou, W., Kitayaporn, S., Schwartz, D. T., Murali-Krishna, K., Kavanagh, T. J., and Baneyx, F., Biomineralization and size control of calcium phosphate core-protein shell nanoparticles: potential for vaccine applications. *Bioconjug. Chem.*, 2012. **23**: p. 610-617.
228. Zhou, W. and Baneyx, F., Biofabrication of ZnS:Mn luminescent nanocrystals using histidine, hexahistidine, and His-tagged proteins: a comparison study. *Biochem. Eng. J.*, 2014. **89**: p. 28-32.
229. Chen, H. B., Su, X. D., Neoh, K.-G., and Choe, W. S., Context-dependent adsorption behavior of cyclic and linear peptides on metal oxide. *Langmuir*, 2009. **25**: p. 1588-1593.
230. Zrazhevskiy, P., Sena, M., and Gao, X., Designing multifunctional quantum dots for bioimaging, detection, and drug delivery. *Chem Soc Rev*, 2010. **39**: p. 4326-4354.
231. Frigerio, C., Ribeiro, D. S., Rodrigues, S. S., Abreu, V. L., Barbosa, J. A., Prior, J. A., Marques, K. L., and Santos, J. L., Application of quantum dots as analytical tools in automated chemical analysis: a review. *Anal Chim Acta*, 2012. **735**: p. 9-22.
232. Sun, Q., Wang, A., Li, L. S., Wang, D., Zhu, T., Xu, J., Yang, C. S., and Li, Y., Bright, multicoloured light-emitting diodes based on quantum dots. *Nature Photon*, 2007. **1**: p. 717-722.
233. Shirasaki, Y., Supran, G. J., Bawendi, M. G., and Bulovic, V., Emergence of colloidal quantum-dot light-emitting technologies. *Nature Photon*, 2013. **7**: p. 13-23.
234. Nozik, A. J., Beard, M. C., Luther, J. M., Law, M., Ellingson, R. J., and Johnson, J. C., Semiconductor quantum dots and quantum dot arrays and applications of multiple exciton generation to third-generation photovoltaic solar cells. *Chem Rev*, 2010. **110**: p. 6873-6890.
235. Winnik, F. M. and Maysinger, D., Quantum dot cytotoxicity and ways to reduce it. *Acc Chem Res*, 2013. **46**: p. 672-680.
236. Bottrill, M. and Green, M., Some aspects of quantum dot toxicity. *Chem Commun (Camb)*, 2011. **47**(25): p. 7039-50.
237. Derfus, A. M., Chan, W. C. W., and Bhatia, S. N., Probing the cytotoxicity of semiconductor quantum dots. *Nano Lett*, 2004. **4**: p. 11-18.
238. Gomes, S. A., Vieira, C. S., Almeida, D. B., Santos-Mallet, J. R., Menna-Barreto, R. F., Cesar, C. L., and Feder, D., CdTe and CdSe quantum dots cytotoxicity: a comparative study on microorganisms. *Sensors (Basel)*, 2011. **11**(12): p. 11664-78.
239. Ostermeier, M., Engineering allosteric protein switches by domain insertion. *Protein Eng Des Sel*, 2005. **18**(8): p. 359-64.
240. Smith, W. E., Brownell, J., White, C. C., Afsharinejad, Z., Tsai, J., Hu, X., Polyak, S. J., Gao, X., Kavanagh, T. J., and Eaton, D. L., In vitro toxicity assessment of amphiphillic polymer-coated CdSe/ZnS quantum dots in two human liver cell models. *ACS Nano*, 2012. **6**(11): p. 9475-84.
241. Anas, A., Akita, H., Harashima, H., Itoh, T., Ishikawa, M., and Biju, V., Photosensitized breakage and damage of DNA by CdSe-ZnS quantum dots. *J Phys Chem B*, 2008. **112**(32): p. 10005-11.
242. Hoshino, A., Hanada, S., and Yamamoto, K., Toxicity of nanocrystal quantum dots: the relevance of surface modifications. *Arch Toxicol*, 2011. **85**(7): p. 707-20.
243. Yong, K. T., Law, W. C., Hu, R., Ye, L., Liu, L., Swihart, M. T., and Prasad, P. N., Nanotoxicity assessment of quantum dots: from cellular to primate studies. *Chem Soc Rev*, 2013. **42**(3): p. 1236-50.

244. Kloepfer, J. A., Mielke, R. E., and Nadeau, J. L., Uptake of CdSe and CdSe/ZnS quantum dots into bacteria via purine-dependent mechanisms. *Appl Env Microbiol*, 2005. **71**: p. 2548-2557.
245. Mahendra, S., Zhu, H., Colvin, V. L., and Alvarez, P. J., Quantum dot weathering results in microbial toxicity. *Environ Sci Technol*, 2008. **42**: p. 9424-9430.
246. Schneider, R., Wolpert, C., Guilloteau, H., Balan, L., Lambert, J., and Merlin, C., The exposure of bacteria to CdTe-core quantum dots: the importance of surface chemistry on cytotoxicity. *Nanotechnology*, 2009. **20**: p. 225101.
247. Zhou, W., Swift, B. J. F., and Baneyx, F., A minimized designer protein for facile biofabrication of ZnS:Mn immuno-quantum dots *Chem Commun*, 2015. **Submitted**.
248. Nies, D. H., Microbial heavy metal resistance. *Appl Microbiol Biotechnol*, 1999. **51**: p. 730-750.
249. Minsky, A., Summers, R. G., and Knowles, J. R., Secretion of beta-lactamase into the periplasm of Escherichia coli: evidence for a distinct release step associated with a conformational change. *Proceedings of the National Academy of Sciences of the United States of America*, 1986. **83**(12): p. 4180-4184.
250. Bianchi, A. A. and Baneyx, F., Stress Responses as a Tool To Detect and Characterize the Mode of Action of Antibacterial Agents. *Applied and Environmental Microbiology*, 1999. **65**(11): p. 5023-5027.
251. Shapiro, E. and Baneyx, F., Stress-Based Identification and Classification of Antibacterial Agents: Second-Generation Escherichia coli Reporter Strains and Optimization of Detection. *Antimicrobial Agents and Chemotherapy*, 2002. **46**(8): p. 2490-2497.
252. Silhavy, T. J. B., M. L.; Enquist, L. W., *Experiments with Gene Fusions*. 1984, Cold Spring Harbor, NY: Cold Spring Harbor Laboratory Press.
253. Silhavy, T. J., Kahne, D., and Walker, S., The Bacterial Cell Envelope. *Cold Spring Harbor Perspectives in Biology*, 2010. **2**(5).
254. Li, W., Xie, H., Xie, Z., Lu, Z., Ou, J., Chen, X., and Shen, P., Exploring the mechanism of competence development in Escherichia coli using quantum dots as fluorescent probes. *Journal of Biochemical and Biophysical Methods*, 2004. **58**(1): p. 59-66.
255. Nikaido, H., Molecular Basis of Bacterial Outer Membrane Permeability Revisited. *Microbiology and Molecular Biology Reviews*, 2003. **67**(4): p. 593-656.
256. Shaner, N. C., Campbell, R. E., Steinbach, P. A., Giepmans, B. N. G., Palmer, A. E., and Tsien, R. Y., Improved monomeric red, orange and yellow fluorescent proteins derived from Discosoma sp. red fluorescent protein. *Nat Biotech*, 2004. **22**(12): p. 1567-1572.
257. Bayer, M. E., Areas of Adhesion between Wall and Membrane of Escherichia coli. *Journal of General Microbiology*, 1968. **53**(3): p. 395-404.
258. Ruiz, N., Kahne, D., and Silhavy, T. J., Advances in understanding bacterial outer-membrane biogenesis. *Nat Rev Micro*, 2006. **4**(1): p. 57-66.
259. Dumas, E. M., Ozenne, V., Mielke, R. E., and Nadeau, J. L., Toxicity of CdTe Quantum Dots in Bacterial Strains. *NanoBioscience, IEEE Transactions on*, 2009. **8**(1): p. 58-64.
260. Dwarakanatha, S., Bruno Jg Fau - Athmaram, T. N., Athmaram Tn Fau - Bali, G., Bali G Fau - Vattem, D., Vattem D Fau - Rao, P., and Rao, P., Antibody-quantum dot conjugates exhibit enhanced antibacterial effect vs. unconjugated quantum dots. (0015-5632 (Print)).
261. Kloepfer, J. A., Mielke, R. E., Wong, M. S., Nealson, K. H., Stucky, G., and Nadeau, J. L., Quantum Dots as Strain- and Metabolism-Specific Microbiological Labels. *Applied and Environmental Microbiology*, 2003. **69**(7): p. 4205-4213.

262. Lu, Z., Li Cm Fau - Bao, H., Bao H Fau - Qiao, Y., Qiao Y Fau - Toh, Y., Toh Y Fau - Yang, X., and Yang, X., Mechanism of antimicrobial activity of CdTe quantum dots. (0743-7463).
263. Imlay, J. A., Cellular defenses against superoxide and hydrogen peroxide. (0066-4154).
264. Zhang, C. and Suslick, K. S., A Colorimetric Sensor Array for Organics in Water. *Journal of the American Chemical Society*, 2005. **127**(33): p. 11548-11549.
265. Medintz, I. L., Clapp, A. R., Mattoussi, H., Goldman, E. R., Fisher, B., and Mauro, J. M., Self-assembled nanoscale biosensors based on quantum dot FRET donors. *Nat Mater*, 2003. **2**(9): p. 630-638.
266. Xu, C., Xing, B., and Rao, J., A self-assembled quantum dot probe for detecting β-lactamase activity. *Biochemical and Biophysical Research Communications*, 2006. **344**(3): p. 931-935.
267. Algar, W. R. and Krull, U. J., Towards multi-colour strategies for the detection of oligonucleotide hybridization using quantum dots as energy donors in fluorescence resonance energy transfer (FRET). *Analytica Chimica Acta*, 2007. **581**(2): p. 193-201.
268. Medintz, I. L. and Mattoussi, H., Quantum dot-based resonance energy transfer and its growing application in biology. *Physical Chemistry Chemical Physics*, 2009. **11**(1): p. 17-45.
269. Duan, N., Zhang, H., Nie, Y., Wu, S., Miao, T., Chen, J., and Wang, Z., Fluorescence resonance energy transfer-based aptamer biosensors for bisphenol A using lanthanide-doped KGdF4 nanoparticles. *Analytical Methods*, 2015. **7**(12): p. 5186-5192.
270. Zhang, C.-y. and Johnson, L. W., Quantum-Dot-Based Nanosensor for RRE IIB RNA−Rev Peptide Interaction Assay. *Journal of the American Chemical Society*, 2006. **128**(16): p. 5324-5325.
271. Dennis, A. M., Rhee, W. J., Sotto, D., Dublin, S. N., and Bao, G., Quantum Dot-Fluorescent Protein FRET Probes for Sensing Intracellular pH. *ACS Nano*, 2012. **6**(4): p. 2917-2924.
272. Boeneman, K., Mei, B. C., Dennis, A. M., Bao, G., Deschamps, J. R., Mattoussi, H., and Medintz, I. L., Sensing Caspase 3 Activity with Quantum Dot-Fluorescent Protein Assemblies. *Journal of the American Chemical Society*, 2009. **131**(11): p. 3828-3829.
273. Dennis, A. M. and Bao, G., Quantum Dot−Fluorescent Protein Pairs as Novel Fluorescence Resonance Energy Transfer Probes. *Nano Letters*, 2008. **8**(5): p. 1439-1445.
274. Chang, E., Protease-activated quantum dot probes. *Biochem. Biophys. Res. Commun.*, 2005. **334**: p. 1317-1321.
275. *Introduction to Fluorescence*, in *Principles of Fluorescence Spectroscopy*, J.R. Lakowicz, Editor. 2006, Springer US: Boston, MA. p. 1-26.
276. Swift, B. J. F. and Baneyx, F., Microbial Uptake, Toxicity, and Fate of Biofabricated ZnS:Mn Nanocrystals. *PLoS ONE*, 2015. **10**(4): p. e0124916.
277. Coyle, B. L., *Solid-binding proteins for modification of inorganic substrates.* 2014.
278. Coyle, B. L., Rolandi, M., and Baneyx, F., Carbon-binding designer proteins that discriminate between sp2- and sp3-hybridized carbon surfaces. *Langmuir*, 2013. **29**(15): p. 4839-46.
279. Nannenga, B. L. and Baneyx, F., Reprogramming chaperone pathways to improve membrane protein expression in Escherichia coli. *Protein Science : A Publication of the Protein Society*, 2011. **20**(8): p. 1411-1420.

280. Zhou, W., Swift, B. J. F., and Baneyx, F., A minimized designer protein for facile biofabrication of ZnS:Mn immuno-quantum dots. *Chemical Communications*, 2015. **51**(17): p. 3515-3517.
281. Mehta, J., Van Dorst, B., Rouah-Martin, E., Herrebout, W., Scippo, M.-L., Blust, R., and Robbens, J., In vitro selection and characterization of DNA aptamers recognizing chloramphenicol. *Journal of Biotechnology*, 2011. **155**(4): p. 361-369.
282. DeForest, C. A. and Tirrell, D. A., A photoreversible protein-patterning approach for guiding stem cell fate in three-dimensional gels. *Nat Mater*, 2015. **14**(5): p. 523-531.
283. Gawley, R. E., Mao, H., Haque, M. M., Thorne, J. B., and Pharr, J. S., Visible Fluorescence Chemosensor for Saxitoxin. *The Journal of Organic Chemistry*, 2007. **72**(6): p. 2187-2191.
284. Quilliam, M. A., Sim, P. G., McCulloch, A. W., and McInnes, A. G., High-Performance Liquid Chromatography of Domoic Acid, a Marine Neurotoxin, with Application to Shellfish and Plankton. *International Journal of Environmental Analytical Chemistry*, 1989. **36**(3): p. 139-154.
285. Ellington, A. D. and Szostak, J. W., In vitro selection of RNA molecules that bind specific ligands. *Nature*, 1990. **346**(6287): p. 818-822.
286. Tuerk, C. and Gold, L., Systematic evolution of ligands by exponential enrichment: RNA ligands to bacteriophage T4 DNA polymerase. *Science*, 1990. **249**(4968): p. 505-510.
287. Graff, R. A., Swanson, J. P., Barone, P. W., Baik, S., Heller, D. A., and Strano, M. S., Achieving Individual-Nanotube Dispersion at High Loading in Single-Walled Carbon Nanotube Composites. *Advanced Materials*, 2005. **17**(8): p. 980-984.
288. Elghanian, R., Storhoff, J. J., Mucic, R. C., Letsinger, R. L., and Mirkin, C. A., Selective colorimetric detection of polynucleotides based on the distance-dependent optical properties of gold nanoparticles. *Science*, 1997. **277**: p. 1078-1081.
289. Dubertret, B., Calame, M., and Libchaber, A. J., Single-mismatch detection using gold-quenched fluorescent oligonucleotides. *Nature Biotechnol.*, 2001. **19**: p. 365-370.
290. Pons, T., Medintz, I. L., Sapsford, K. E., Higashiya, S., Grimes, A. F., English, D. S., and Mattoussi, H., On the Quenching of Semiconductor Quantum Dot Photoluminescence by Proximal Gold Nanoparticles. *Nano Letters*, 2007. **7**(10): p. 3157-3164.
291. Kulakovich, O., Strekal, N., Yaroshevich, A., Maskevich, S., Gaponenko, S., Nabiev, I., Woggon, U., and Artemyev, M., Enhanced Luminescence of CdSe Quantum Dots on Gold Colloids. *Nano Letters*, 2002. **2**(12): p. 1449-1452.
292. Deng, W., Xie, F., Baltar, H. T. M. C. M., and Goldys, E. M., Metal-enhanced fluorescence in the life sciences: here, now and beyond. *Physical Chemistry Chemical Physics*, 2013. **15**(38): p. 15695-15708.
293. Ji, B., Giovanelli, E., Habert, B., Spinicelli, P., Nasilowski, M., Xu, X., Lequeux, N., Hugonin, J.-P., Marquier, F., Greffet, J.-J., and Dubertret, B., Non-blinking quantum dot with a plasmonic nanoshell resonator. *Nat Nano*, 2015. **10**(2): p. 170-175.
294. Kim, Y.-P., Oh, Y.-H., Oh, E., Ko, S., Han, M.-K., and Kim, H.-S., Energy Transfer-Based Multiplexed Assay of Proteases by Using Gold Nanoparticle and Quantum Dot Conjugates on a Surface. *Analytical Chemistry*, 2008. **80**(12): p. 4634-4641.
295. Gueroui, Z. and Libchaber, A., Single-Molecule Measurements of Gold-Quenched Quantum Dots. *Physical Review Letters*, 2004. **93**(16): p. 166108.
296. Oh, E., Hong, M.-Y., Lee, D., Nam, S.-H., Yoon, H. C., and Kim, H.-S., Inhibition Assay of Biomolecules based on Fluorescence Resonance Energy Transfer (FRET) between

Quantum Dots and Gold Nanoparticles. *Journal of the American Chemical Society*, 2005. **127**(10): p. 3270-3271.

297. Ratchford, D., Shafiei, F., Kim, S., Gray, S. K., and Li, X., Manipulating Coupling between a Single Semiconductor Quantum Dot and Single Gold Nanoparticle. *Nano Letters*, 2011. **11**(3): p. 1049-1054.
298. Dubertret, B., Calame, M., and Libchaber, A. J., Single-mismatch detection using gold-quenched fluorescent oligonucleotides. *Nat Biotech*, 2001. **19**(4): p. 365-370.
299. Naik, R. R., Stringer, S. J., Agarwal, G., Jones, S. E., and Stone, M. O., Biomimetic synthesis and patterning of silver nanoparticles. *Nat Mater*, 2002. **1**(3): p. 169-172.
300. Nies, D. H., Microbial heavy-metal resistance. *Applied Microbiology and Biotechnology*, 1999. **51**(6): p. 730-750.
301. Yilmaz, E. I., Metal tolerance and biosorption capacity of Bacillus circulans strain EB1. *Research in Microbiology*, 2003. **154**(6): p. 409-415.
302. Xu, F. F. and Imlay, J. A., Silver(I), Mercury(II), Cadmium(II), and Zinc(II) Target Exposed Enzymic Iron-Sulfur Clusters when They Toxify Escherichia coli. *Applied and Environmental Microbiology*, 2012. **78**(10): p. 3614-3621.
303. Shaw, J. R., Dempsey, T. D., Chen, C. Y., Hamilton, J. W., and Folt, C. L., Comparative toxicity of cadmium, zinc, and mixtures of cadmium and zinc to daphnids. *Environmental Toxicology and Chemistry*, 2006. **25**(1): p. 182-189.

Appendix A

Effects of metal nanoparticles on QD emission

There has been considerably effort to improve QD overall fluorescence by the addition of close proximity noble metals because of their plasmonic properties.[288-290] While there have been some reports of success[291-293], it is far more common for these plasmonic metals to quench the fluorescence of any QDs they are associated with.[290, 294-298] In order to ascertain if complexation of gold nanoparticles could provide enhancement of QD emission, sfGFP::Ag4-CT43 was constructed. This protein enables mineralization of ZnS:Mn QDs, while also imparting the potential to complex silver or gold via the Ag4 tag.[299]

Materials and Methods

Oligonucleotides (10 μM) of seuqunce 5'-GCTATAGTTGGATCCAACCCGAGCAGCCTGTTTTCGCTATCTGCCGAGCGATACTAGTTCATAGCG-3' and 5'-CGCATATGAACTAGTATCGCTCGGCAGATAGCGAAACAGGCTGCTCGGGTTGGATCCAACTATAGC-3' were annealed in boiling water for 10 minutes and digested by restriction enzymes *BamHI* and *SpeI* for 3 hours at 37 °C. Concurrently, the previously constructed sfGFP::Car9-CT43 with the *BamHI* mutation in pet24a+ was also digested with *BamHI* and *SpeI* for 3 hours at 37 °C. The backbone of sfGFP::-CT43 in pet24a+ was then ligated with the CT43 oligonucleotides at a ratio of 3:1, insert:backbone for 16 hours at 16 °C. The protein was then expressed and purified as detailed in *Chapter 3*.

Gold nanoparticle dosing in solution

Gold nanoparticles of three sizes: 5 nm (Sigma Aldrich), 50 nm (Nanocomposix), and 90 nm (Cytodisgnostics) in 50 nM citrate buffers were added to sfGFP::Car9-CT43 or sfGFP::Ag4-CT43 capped QDs at a final concentration of 30 µM or ~ 4 x10^{11} particles/mL.

Analytical Techniques

Fluorescence and phosphorescence emission spectra were recorded using 1 mL of sample on a Hitachi F4500 fluorescence spectrophotometer with excitation and emission slit widths set at 2.5 nm (fluorescence). The wavelength region corresponding to the second order diffraction peak of the excitation light was omitted.

Results and Discussion

Impact of gold nanopartlces on ZnS:Mn QD emission

The addition of gold nanoparticles to QD solutions uniformly quenches emission upon excitation at 305 nm, with the 5 nm particles having the most significant (>50%) impact.

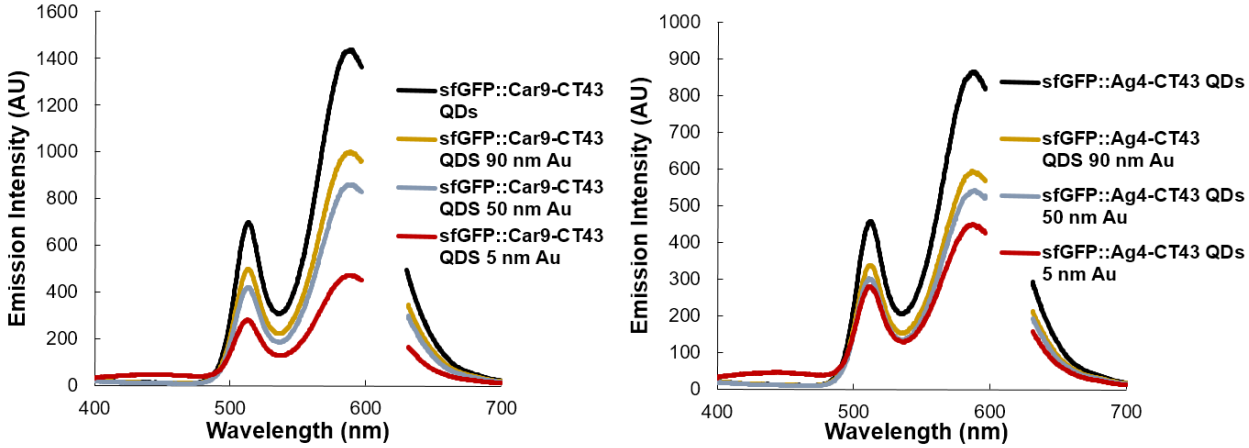

Figure A.1 Gold nanoparticles of various sizes cause a decrease in the emission intensity of both sfGFP::Car9-CT43 and sfGFP::Ag4-CT43 capped ZnS:Mn QDs

Appendix B

Comparative toxicities of metals

Evaluating the absolute toxicity of QD base materials is difficult because the actual dose delivered can be significantly different from the dose added to cell media. Despite the complicating factors, minimal inhibitory concentrations (MIC) for cadmium and zinc have been reported at 0.5 mM and 1 mM respectively for *E. coli*[300], and as high as 2 mM and 22 mM for a heavy metal resistant strain of the bacterium *Bacillus circulans.*[301] Relative toxicities for the two metals in their ionic forms fluctuates between 2-10 fold with cadmium consistently appearing to be more toxic than zinc.[302, 303] For this appendix we evaluate the MIC of ionic zinc, manganese, and copper on *E. coli*.

Materials and Methods

Determining minimal inhibitory concentrations

E. coli AB734 (F^-*lac-6*(del)) was grown overnight at 30°C in 5 mL of LB medium. Cells were pelleted by centrifugation for 5 min at 6,000 rpm, resuspended in 5 mL of 10 mM $MgSO_4$, diluted 1:4 so the optical density at 600nm (OD_{600}) was 0.265, diluted 1:100, and 20 µL aliquots ($\approx 5x10^4$ cells, as determined by colony counting) were mixed with 1 mL of LB. One mL serial dilutions of Zn^{2+} (9.12mM), Mn^{2+} (91.2mM), and Cu^{2+} (15.2mM) stock solutions were made so 500µL was added to every sample. Final concentrations varied from 3-1 mM for Zn^{2+}, 30-15 mM Mn^{2+}, and 5-1 mM Cu^{2+}. This controlled the final volume to 1.52 mL. Cultures were grown for 24 h at 30°C with shaking. Any culture with an OD_{600} less than 0.01 was considered dead.

Results and Discussion

Comparing the toxicity of zinc, manganese, and copper

The determined MIC values for all three metals agrees well with previously reported literature values and are displayed in Table 1.

Table 1

Metal Ion	Experimental Value		Literature Value		Reference
	mM	μg/mL	mM	μg/mL	
Zn^{2+}	2.4	528	2.2	484	Brocklehurst, K.; Morby, A. *Microbiology* **146**, 2277-2282 (2000)
Cu^{2+}	3.7	729	1.0	170	Nies, D.H. *Applied Microbiology and Biotechnology* **51**, 730-750 (1999)
Mn^{2+}	20.0	4000	20.0	4000	Nies, D.H. *Applied Microbiology and Biotechnology* **51**, 730-750 (1999)